

박사학위논문  
Ph.D. Dissertation

리드버그 원자 양자전산모사를 위한 단원자열  
생성

Reconfigurable single-atom array for Rydberg atom quantum  
simulation

2018

김효섭 (金孝燮 Kim, Hyosub)

한국과학기술원

Korea Advanced Institute of Science and Technology

박사학위논문

리드버그 원자 양자전산모사를 위한 단원자열  
생성

2018

김효섭

한국과학기술원

물리학과

# 리드버그 원자 양자전산모사를 위한 단원자열 생성

김 호 섭

위 논문은 한국과학기술원 박사학위논문으로  
학위논문 심사위원회의 심사를 통과하였음

2017년 11월 13일

심사위원장 안 재 욱 (인)

심 사 위 원 이 순 칠 (인)

심 사 위 원 강 명 수 (인)

심 사 위 원 이 성 빈 (인)

심 사 위 원 이 재 훈 (인)

# Reconfigurable single-atom array for Rydberg atom quantum simulation

Hyosub Kim

Advisor: Jaewook Ahn

A dissertation submitted to the faculty of  
Korea Advanced Institute of Science and Technology in  
partial fulfillment of the requirements for the degree of  
Doctor of Philosophy in Physics

Daejeon, Korea  
November 13, 2017

Approved by

---

Jaewook Ahn  
Professor of Physics Department

The study was conducted in accordance with Code of Research Ethics<sup>1</sup>.

---

<sup>1</sup> Declaration of Ethical Conduct in Research: I, as a graduate student of Korea Advanced Institute of Science and Technology, hereby declare that I have not committed any act that may damage the credibility of my research. This includes, but is not limited to, falsification, thesis written by someone else, distortion of research findings, and plagiarism. I confirm that my thesis contains honest conclusions based on my own careful research under the guidance of my advisor.

DPH  
20118036

김효섭. 리드버그 원자 양자전산모사를 위한 단원자열 생성. 물리학과 . 2018년. 107+iv 쪽. 지도교수: 안재욱 (영문 논문)

Hyosub Kim. Reconfigurable single-atom array for Rydberg atom quantum simulation. Department of Physics . 2018. 107+iv pages. Advisor: Jaewook Ahn (Text in English)

### 초 록

이 학위논문에서는 단원자열을 홀로그래프를 통해 생성하고 움직이는 일을 수행하였다. 이를 위해 액정 광변조기를 사용하였고, 홀로그래프 알고리즘을 개발하였으며, 이를 저온 원자에 적용하여 광포획된 단원자들을 2차원 평면에서 동시다발적으로 움직이는 일을 성공하였다. 이와 더불어 실시간 되먹임 조절을 통하여 20개 이상의 완벽히 채워진 단원자열을 생성할 수 있었다. 여기에 리드버그 원자 상호작용을 더하여 스핀-1/2 입자 모형이 열평형점으로 수렴하는 과정을 실험적으로 양자전산모사 하였다. 이처럼 크기를 확장 가능하고 모양을 자유롭게 바꿀 수 있는 단원자열 생성은 양자 전산 및 양자 다체계 모사 연구 수행에 필요한 선결 과제 중 하나이다. 이를 해결함으로써 향후 이 분야에 기여를 할 수 있을 것으로 기대된다.

핵심 낱말 양자 전산 모사, 저온 원자, 단원자, 리드버그 원자

### Abstract

In this thesis, real-time transport of single-atom array using holographic tweezers is demonstrated. For this, a liquid-crystal spatial light modulator is used, a computer-generated hologram algorithm (CGHA) is devised based on Gerchberg-Saxton algorithm, and cold rubidium ( $^{87}\text{Rb}$ ) single atoms trapped in the tweezers are simultaneously rearranged without atom losses. In-situ feedback control for defect-free single-atom array formation is also demonstrated. By adding Rydberg atom interaction to this system, thermalization dynamics of spin-1/2 lattice model is simulated as well. Establishing such reliable method to form a scalable neutral-atom platform has been an important task to be achieved for quantum information science and quantum simulation of many-body systems. The methodology presented in this thesis resolves the issue and is expected to contribute the progression in the field of neutral atoms quantum simulation and quantum information.

Keywords Quantum simulation, Cold atom, Single atom, Rydberg atom,



# Contents

Contents . . . . .	i
List of Tables . . . . .	iii
List of Figures . . . . .	iv
<b>Chapter 1. Introduction</b>	<b>1</b>
1.1 Personal viewpoint . . . . .	1
1.2 In this thesis . . . . .	2
<b>Chapter 2. Experimental background and setup</b>	<b>3</b>
2.1 Vacuum chamber . . . . .	3
2.2 Cooling and Trapping of Rb atoms . . . . .	6
2.2.1 MOT characterization . . . . .	6
2.3 Optical Dipole Trap . . . . .	9
2.3.1 The single-atom optical dipole trap . . . . .	11
2.3.2 Characterization of the single-atom trap . . . . .	11
<b>Chapter 3. Dynamic phase holograms for single atom optical traps</b>	<b>14</b>
3.1 Spirit of the approach . . . . .	14
3.2 The proof-of-principle: random mask algorithm . . . . .	14
3.2.1 Experimental concept and flicker-free beam steering algorithm . . . . .	14
3.2.2 Simultaneous transport of $N$ single atoms . . . . .	16
3.2.3 Single-atom array synthesis demonstration . . . . .	16
3.2.4 Discussion . . . . .	17
3.2.5 Methods . . . . .	21
3.3 Scale Improvement; superposition algorithm . . . . .	24
3.4 Versatility Improvement: a modified Gerchberg-Saxton algorithm . . . . .	26
3.4.1 Upgrade of spatial light modulatr . . . . .	26
3.4.2 Experimental setup and procedure . . . . .	26
3.5 Weighted, induction, and zero-pedding Gerchberg-Saxton algorithm . . . . .	31
3.5.1 Review . . . . .	31
3.5.2 Issues to be addressed . . . . .	32
3.5.3 Weighted-GS . . . . .	33

3.5.4	Induction-GS . . . . .	33
3.5.5	Zero-padding-GS . . . . .	33
3.5.6	Phase reduction . . . . .	33
3.5.7	Algorithm performance . . . . .	34
3.5.8	Results . . . . .	36
3.5.9	Discussion . . . . .	36
3.6	Source code . . . . .	38
3.6.1	Matlab . . . . .	38
3.6.2	C++ . . . . .	45
<b>Chapter 4.</b>	<b>A Rydberg atom quantum simulator</b>	<b>56</b>
4.1	Brief Introduction . . . . .	56
4.2	Rydberg atom excitation . . . . .	56
4.2.1	Level scheme and Rydberg lasers . . . . .	57
4.2.2	Rydberg resonance finding . . . . .	58
4.2.3	The experimental protocol . . . . .	60
4.2.4	Stray electric field . . . . .	62
4.3	Toward many-body experiments . . . . .	65
4.3.1	Detailed balance of thermalization dynamics in Ising-like quantum magnets . . . . .	66
4.3.2	Supplements . . . . .	71
<b>Chapter 5.</b>	<b>Conclusion</b>	<b>83</b>
<b>Chapter 6.</b>	<b>Appendix</b>	<b>84</b>
6.1	Trap depth calculation code in Matlab . . . . .	84
6.2	Hungarian algorithm code in Matlab . . . . .	85
6.3	Miscellaneous experimental apparatus . . . . .	90
	<b>Bibliography</b>	<b>92</b>
	<b>Acknowledgments in Korean</b>	<b>102</b>
	<b>Curriculum Vitae</b>	<b>103</b>

## List of Tables

3.1	Future perspectives for larger scale arrays. . . . .	38
4.1	Quantum defect for $^{87}\text{Rb}$ Rydberg states [136]. . . . .	59
4.2	Individual dephasing sources. . . . .	75
4.3	Collective dephasing sources. . . . .	76
4.4	Projection measurement error sources. . . . .	77

## List of Figures

2.1 Vacuum glass cell. It is made of Pyrex. The clear window dimension is 100 mm × 40 mm × 40 mm located at the center, and the thickness is 3.5 mm. Both ends are mounted with rotatable 2.75 inch flanges and sealed with lead-like material, limiting bake-out temperature to 250 °C. The angled-arm on the right side has two Rb getters (SAES getters) for atoms supply. The getter should be initially baked out for 10 minutes with 4 A current during the entire chamber bake-out stage. The windows are one-side anti-reflection (AR) coated to 400-800nm range. It is a customized product from "Precisionglassblowing," USA. . . . .	3
2.2 Objective lens for single atom experiments. High NA and outside vacuum chamber accessibility is simultaneously achieved by just adopting this commercial objective lens. One defect is color mismatch that diminishes the transmittance, yet it is affordable at around 800 nm wavelength. The lens is purchased from "Mitutoyo," Japan. . . . .	4
2.3 Customized 5-Way metal adaptor. Each way corresponds to the glass cell, ion gauge, ion pump, gate valve, and laser beam window, respectively. . . . .	4
2.4 The completely assembled vacuum chamber. The periphery of optics are also shown as well. . . . .	5
2.5 The measured pressure inside the chamber, with bake-out temperature. . . . .	5
2.6 The principle of Magneto-optical trap (MOT). . . . .	6
2.7 MOT and characterization setup overall. (a) optical alignment parts. (b) Chamber top view. The microscope imaging parts are for micro optical dipole trap which will be discussed in the next section. (c) Chamber side view. The relevant parameter for Anti-Helmholtz (AH) coils are presented. . . . .	7
2.8 (a) MOT pulse and MOT characterization sequence time table. (b) Time of Flight measurement scheme from Ref. [51]. . . . .	8
2.9 MOT characterization results. (a) Time of Flight image from the camera. The falling time is 63 ms. (b) The white dotted square box in (a) is summed over and plotted as a function of time. The label 2 is for background compensation to estimate the atom number. . . . .	8
2.10 The AC Stark shift of two level system. Its representation has adopted from Ref. [52]. . . . .	9
2.11 (a) Dipole trap laser optical parts. These parts are additional to Figure 2.7(a). The microscope imaging parts in Figure 2.7(b) are replaced to these. (b) The pulses and trigger timing sequence for ODT absorption imaging experiments. (c) An absorption profile of ODT in radial direction. (d) An absorption image of ODT. . . . .	10
2.12 My single atom loading results. (a) its histogram. (b) Single atom loss curve. . . . .	11
2.13 Measured single atom temperature by release and recapture method presented in Ref. [57]. My measurement pulse sequences are shown. . . . .	12
2.14 Measured single atom trap frequency in radial direction. The method was presented in Ref. [58]. My measurement pulse sequences are shown. . . . .	13

3.1	<b>Set-up for single-atom holographic transport.</b> <b>a</b> , The optical system for hologram transfer and trap imaging. <b>b</b> , Schematic 2D phase planes of the liquid crystal spatial light modulator (LC-SLM) in gray scale. One of them intuitively illustrates the working principle (arc division), and the other shows real hologram (random division), respectively. <b>c</b> , An example of loaded single atoms in a tweezer array, represented with $22 \times 22 \mu\text{m}^2$ size 500 cumulative images. The parenthesis denotes the loading probability and life time. <b>d</b> , The intensity standard deviation as a function of $N_t$ for the random division. The data points were calculated for various beam waists $W$ at the SLM window (circles for $W = 1$ mm, squares for 2 mm, crosses for 3 mm, and diamonds for 4 mm) and the solid lines are the linear fits to the data. The inset presents the intensity histogram of $W = 2$ mm for $N_t = 9$ of the red mark. <b>e</b> , An in situ single-atom array expansion movie.	15
3.2	<b>Single-atom transport example.</b> <b>a</b> , Transient cumulative images of 500 snapshots showing that nine atoms move the predefined path (red arrows) sequentially. <b>b</b> , Three selected single events having four atoms or more. Every snapshot represents the same $26 \times 26 \mu\text{m}^2$ area. The images are Gaussian-filtered for clarity.	17
3.3	<b>In situ single-atom array synthesis.</b> <b>a</b> , The feedback-control loop sequence: (i) signal gathering and processing with a charge-coupled device (CCD), (ii) state resolving and solution finding, (iii) solution execution with a spatial light modulator (SLM). <b>b</b> , The cumulative image of initially loaded $N = 9$ atoms (left), accompanied by the corresponding number histogram (right), where the scale bar size is $5 \mu\text{m}$ . <b>c</b> , From the initial 9 sites, one, two, three, and four atoms are rearranged through single feedback loop. <b>d</b> , Success probabilities of the atom rearrangement: $p = 0.5$ (black dotted line), experiments (red line and data points), and theoretical limit (blue dashed line). The error bar depicts the standard deviation of time-binned 100 events.	18
3.4	<b>Intensity flicker of IFTA transport.</b> <b>a</b> , Stroboscopic measurement of optical images of the trap array. Two different images are generated using an IFTA and the LC-SLM. The two upper lows in the second and third frames (right) are slightly shifted up, by the gaps indicated by the arrows, from the first frame (left). <b>b</b> , The transient potential for the trap loss simulation. The trap waist is $w_o = 1.14 \mu\text{m}$ , the transient time $\tau = 1/f$ where $f$ is frame rate, and the displacement $w_o/18$ . The color scale is normalized by the peak potential, $-U$ . <b>c</b> , Trap loss landscape by the flickering potential ( <b>b</b> ). The color scale normalized by $P_l$ represents the loss probability at time $\tau$ which varies by $0.005 - 0.04$ according to the initial trap condition ( $T/U = 1/18 \sim 1/12$ ).	19

3.5	<b>Transport loss mechanism.</b> <b>a</b> , Schematic modulated two linear phases. The $x$ -axis is normalized to 1. The sum of the shaded regions is $R$ which is proportional to field strength. <b>b</b> , Transient vectorial representation of the flicker effect. <b>c</b> , The experimentally measured loss probabilities are shown for three different tweezer displacements $\Delta x = 180 \mu\text{m}$ , $360 \mu\text{m}$ , and $520 \mu\text{m}$ , respectively. Each data point (gray) is the average of 1,000 experimental runs, the red solid line is the average value of the data points, and the black dashed line is the loss without the displacement. The $x$ -axis is the time-lapse after the array loading, and the $y$ -axis is the single-atom survival probability measured using 1,000 cumulative events and normalized to 1. <b>d</b> , Single-frame losses measured for various $R$ s. The red circles are extracted single-frame data from <b>c</b> and the error bars represent the standard deviations of the different sites. The solid lines are from the adiabatic intensity flicker model (see Methods for more details). . . . .	20
3.6	The experimental sequence table. . . . .	22
3.7	Random mask algorithm scheme. . . . .	24
3.8	<b>(a)</b> Time sequence of the generic experiments. At first, 3D MOT was loaded and soon after detuning of the MOT beam was decreased for PGC stage. The 1 kHz sinusoidal modulation of the detuning was for optimization of single-atom loading rate on the various traps having different depths. Then the MOT coil (anti-Helmholtz) was turned off and the PGC detune was fixed for single-atom fluorescence imaging. After capturing the image, the detune was further decreased and PGC beam was turned off for time $T=0.5$ s that is feed-back operation period. The imaging and feed-back sequence periodically repeated for pre-defined number $N_f$ . Then the entire sequence runs for $N_{exp}$ . $\Gamma$ denotes spontaneous decay rate of $5P_{3/2}$ ( $2\pi \times 6$ MHz). <b>(b)</b> $N=10$ circular array deterministic generation. <b>(c)</b> $N=15$ circular array deterministic generation. . . . .	25
3.9	Two SLM performance comparison. Old one had used before this session of my thesis. New one have used after this session of my thesis. (OLD) the diffracted beam was measured by using photo-diode for both static and dynamic traps. The diffraction efficiency is about 50 % (not shown). The intensity spectrum was shown in linear scale as well. The old device has low (240 Hz) refresh rate, thus the phase fluctuation directly coupled to the intensity noise showing strong spectrum noise peak even in the linear scale. For the dynamic traps, the situation becomes worse showing stronger intensity fluctuation. (NEW) Both the diffracted beam and zero order beam was measured as well as background noise. In the frequency domain, any significant noise peaks have observed. Note that the spectrum is log scale. For the dynamic traps, the saw-tooth intensity traces have observed as expected from the ideal theory of liquid crystal hydro-dynamics. In the spectrum (log scale), harmonics of frame rate have observed. . . . .	27

3.10	(a) Time sequence of the generic experiments described in Figure 3.8 is used again. (b) Lifetime of static (without feed-back operation) single-atom traps. Grey dots are results from individual traps. Red dots are average of the traps. Black line is exponential fit resulting in initial loading rate of 0.51 and lifetime of 40 s. During continuous feed-back operation, lifetime reduced to 20 s. (c) An example of feed-back operation. The 96 total traps including targets were initially loaded. The bipartite graphs connect between single-atom and target site. The blue circles and red dots are single-atom and target sites, respectively. The single-atom transport paths are straight lines corresponding to the links of graphs. The single-shot fluorescence images before and after the feed-back operation represent the result of the graphs. The "Butterfly" is composed of 37 single-atom, having 35 % peak filling rate at $N_f=3$ for $N_{exp}=500$ . . . . .	28
3.11	Average of hundreds of single-atom fluorescence images before and after the aberration compensation (see text). Each images are resulting from the different hologram. Both have the same color scale and dimension. . . . .	29
3.12	Lifetime improvement by applying on/off cycle of PGC beam. The duty cycle 20 % is applied. (Inset) the residue of the exponential fit. . . . .	29
3.13	An example of feedback operation. They are measured optical images from the intermediate plane when a computer-simulated atom loading information is given. The purpose is to gather the atoms in the square lattice to its center for defect-free array formation. . . . .	30
3.14	Monte-Carlo simulation of trap intensity transient minima vs. step size (in unit of trap waist) for various algorithm modifications. Dotted-lines are $C \times \exp(-x^2/2w_0^2)$ where $C$ is 0.3, 0.8, and 1 (theoretical limit) for black, blue, and red, respectively. Shaded areas represent extended accessibility of smaller step size when zero-padding multiplier $N_z$ is applied (see text). The errorbars represent standard deviation. . . . .	34
3.15	(a) Examples of compaction for various 2D arrays of initial 81 sites. (b) Black lines are loading probability of individual (left) and accumulated (right) sites from the center of array for the honeycomb lattice. (c) Examples of deterministic loading from initial 96 square lattice, representing capital letters. All the results were acquired by the same algorithm parameters, i.e. wiz-GS where $i = 5$ , $N_z = 4$ , $n_i = -1$ , and $f_{\#} = 15$ (see Algorithm section). The nearest distance is $3.7 \mu\text{m}$ for all the arrays. . . . .	35
3.16	Monte-Carlo simulation of trap intensity transient minima vs. step size (in unit of trap waist) for various induction $n_i$ , where $\Phi_0^{(k)} = \Phi^{(k-n_i)}$ and wiz-GS+phase reduction. Black lines are $\exp(-x^2/2w_0^2)$ . Gray dots are individual results and red dots are average of them. . . . .	37
3.17	The data flowchart for the single-atom array synthesis. . . . .	39
4.1	(a) Counter-propagating two-photon excitation to a Rydberg state. The B field defines quantization axis. (b) Graphical representation of our Rydberg excitation scheme with Rabi frequency and detuning ( $1/2\pi$ scaled). The Rydberg hyper-fine splitting is an order of 10 kHz thus it is treated in $J$ basis. Zeeman splittings of individual states are shown as well, where the two-level scheme ( $ 5S_{1/2}, F = 2, m_F = 2\rangle$ and $ 67S_{1/2}, J = 1/2, m_J = 1/2\rangle$ ) is robust against magnetic field fluctuation. . . . .	57

4.2	Two Rydberg lasers are frequency locked to external cavity setup. 480 nm and 780 nm lasers are 20 MHz phase modulated by free-space electro-optic modulator (EOM) and coupled to the cavity and then the Pound-Drever-Hall (PDH) signal is generated. An additional fiber phase EOM is used for 780 nm laser. The PDH signals are fed into the fast analogue lock servo (TOPTICA, FALC110). The lock servo generates the error signal to stabilize the laser frequencies to one of the cavity comb. The commercial 480 nm laser (TOPTICA, DLpro) enables to easily feed the error signal into the back-plane BNC connector. The home-built 780 nm laser needs to be modified for stable cavity lock; high frequency bias tee (Thorlab, TG100) is added for fast current modulation. . . . .	58
4.3	Rydberg EIT signal for 61D states. 780 nm laser is locked to $F = 2 \rightarrow F' = 3$ . 480 nm laser frequency is slowly scanned by piezo transducer. 480 nm laser is switched 50 kHz by AOM. 780 nm laser is detected by PD and lock-in amplifier (SRS, SR830). The resulting Rydberg EIT signal shows 61D states. . . . .	59
4.4	(a) The release & recapture protocol and the projection measurement. (b) Time trace of (yellow) switched 820 nm trap laser, and (blue) Rydberg 480 nm laser. The trap laser has rise/fall time of 100 ns. . . . .	60
4.5	Rydberg pulse time analysis. (a) Analysis scheme. (b) Green (Ry 480 nm) and Red (Ry 780 nm) traces are optical pulses measured by fast PD (ET-2030, eotech). Both laser pulses are TTL gated by identical trigger generated from the function generator (DG4162, RIGOL). (c) 480 nm laser gating is generated from DAQ (6353, National Instrument) whereas 780 nm laser gating is generated from the DG535 (Stanford Research Systems). The DG535 is triggered by the same gating pulse of 480 nm laser. (d) 480 nm laser gating is generated from DAQ (6353, National Instrument) whereas 780 nm laser gating is generated from the DG4162. The DG4162 is triggered by the same gating pulse of 480 nm laser. The laser pulses arrive at the chamber or the fast PD after 250ns from the gating pulses. . . . .	61
4.6	Rydberg 480 nm laser alignment scheme. The 480 nm laser beam has only 10 $\mu\text{m}$ diameter ( $1/e^2$ ). Tune the 480 nm wavelength to the near resonance of any Rydberg levels ( $nD_{5/2}$ is preferred) by using wave-meter. By turning on and off the laser, the penetration pattern on the atom array can be observed. . . . .	62
4.7	$^{87}\text{Rb}$ Rydberg Rabi oscillation between $ 5S_{1/2}, F = 2, m_F = 2\rangle \rightarrow  6S_{1/2}, J = 1/2, m_J = 1/2\rangle$ . The protocol and excitation scheme were the same as in Fig. 4.1. The bias B-field was 2 G. (Up) Before ground connection of the nearby metals. (Down) After ground connection of the nearby metals. The oscillation was fitted by exponential decaying cosine function. The time-zero errors are 0.004 and 0.012, respectively. . . . .	63
4.8	3 dimensional electric field scan for $^{87}\text{Rb}$ 65D Stark map measurement. The experiment was done by using single-atom array and release & recapture protocol. There was no bias B-field and optical pumping on this experiment. The laser excitation scheme was the same for the other experiment; counter-propagating $\sigma^\pm$ polarization. The quadrant metal plates [128] were placed outside the glass cell. The electric field was controlled by function generator to exert radio-frequency pulse. DC-field from the outside did not penetrate the glass cell. It is intriguing fact that the glass cell had only pressure of $10^{-10}$ Torr, but still shows the feature of Faraday cage. . . . .	64

4.9	<b>Setup.</b> (a) The wave-front of trap laser is modulated by a liquid-crystal spatial light modulator (SLM) and imaged by a telescope (L1, L2) and an objective lens (L3). The fluorescence image of the trapped atoms is captured by a camera, and analyzed to feedback the SLM for array compactification by atom shuttling. Then, 480 nm and 780 nm lasers excite the array to $67S$ Rydberg state, forming a tunable Ising-like spin-1/2 chain. (b) Zig-zag chain fluorescence images (Gaussian filtered for clarity). . . . .	67
4.10	<b>Thermalization dynamics.</b> Time dependence of Rydberg fraction after the quench for (a) the linear chain of $N = 10$ and $\theta = 180^\circ$ and (b) the zigzag chain of $N = 20$ and $\theta = 60^\circ$ . The experimental data (circles) are compared with the computation (solid lines) and the result (dashed) of the master equation constructed based on the experimental data. The errorbars are standard error of the mean. Right panels: Chain configurations with blockade radius of $r_B = ( C_6 /2\pi\Omega)^{1/6} = 6.5 \mu\text{m}$ and lattice spacing of $d = 4.0(2) \mu\text{m}$ .	68
4.11	<b>Detailed balance in the linear chain of <math>N = 10</math>.</b> (a) The measured $P_n(t)$ (color bars) and its standard deviation ( $\pm\sigma$ , overlaid black lines). At $t > 2 \mu\text{s}$ , the measured data (red dots) and the theoretical predictions (black line) of the steady-state values $P_n^{\text{eq}}$ are shown. The red dashed line evolves along the tallest bar, showing the coherent oscillation of $P_n$ . (b) The ratio $\Gamma_{n \rightarrow n-1}/\Gamma_{n-1 \rightarrow n}$ (red dots) of transition rates are obtained (with errorbar $\pm\sigma$ ) from $P_n^{\text{eq}}$ , and compared with the theoretical prediction (black dots). (c) Graph for the thermalization dynamics. Its nodes (circles) represent low-energy eigenstates of the prequench Hamiltonian $H_0$ , classified by the number $n$ of spin-up atoms in the states. $\nu_n$ is the number of the eigenstates having $n$ spin-up atoms. Each red link connecting two nodes indicates transitions between the corresponding states by $H_I$ . . . . .	69
4.12	<b>Diffusion over prequench states.</b> Time average ( $t \geq t_{\text{relax}}$ ) of the measured probability $ C_m ^2$ of occupying the $m$ -th eigenstates of the prequench Hamiltonian $H_0$ for the linear chain of $N = 10$ . The position of the $D$ -th eigenstate is indicated by the dashed line. Inset: The same for the $\theta = 60^\circ$ zigzag chain of $N = 10$ . . . . .	70
4.13	<b>Thermalization value.</b> Time average $\bar{f}_R$ of measured Rydberg fraction as a function of system size $N$ for the linear chain (red circles) and the zigzag chain of $\theta = 60^\circ$ (blue diamonds). The errorbars of $\pm\sigma$ are shown. For comparison, the MPS result (solid lines) and the ETH prediction (at $N = 19$ for the linear chain and at $N = 21$ for the zigzag chain; color stars) are shown. . . . .	71
4.14	(a) Defect-free atom loading spectra, resulting from two-time of feed-back of total 35 sites, for $\theta = 180^\circ$ (red) and $60^\circ$ (blue), respectively. (b) Graphical representation of our Rydberg excitation scheme with Rabi frequency and detuning ( $1/2\pi$ scaled). The Rydberg hyper-fine splitting is sub-kHz order thus treated in a reduced form. Zeeman splittings of individual states are shown as well, where the two-level scheme ( $ 5S_{1/2}, F = 2, m_F = 2\rangle$ and $ 67S_{1/2}, J = 1/2, m_J = 1/2\rangle$ ) is robust against magnetic field fluctuation. . . . .	72
4.15	Every microstate probability for $N = 11$ , $\theta = \pi$ , and $N = 16$ , $\theta = 78^\circ$ . The $x$ -axis is decreasing order of $n$ . The false-positive detection errors (horizontal shaded areas) are sufficiently low. (Inset) Typical images before and after Rydberg excitation for $N = 11$ , and 16 chains. The bright (empty) sites correspond to the $ \downarrow\rangle$ ( $ \uparrow\rangle$ ) (see text), clearly show Rydberg crystals. The images are re-scaled and Gaussian filtered for clarity. . . . .	74

4.16	<b>Rydberg fraction dynamics</b> (a-c) N=1-3 atoms dynamics of collective Rydberg Rabi oscillation. The points are experimental data of W-states and the solid lines are best fits of $\{1 - \cos(\Omega t) \exp(-t/\tau)\}/2N$ . (a) The color points are data from different positions, 4.4 $\mu\text{m}$ apart. . . . .	75
4.17	N=10, $\theta = 180^\circ$ Rydberg fraction dynamics. Gray lines are Time-domain Schrödinger equation (TDSE) results of 200 Monte-Carlo events. $\delta V(t)$ was estimated by considering 3D atomic thermal motion. Black dashed line is the result of long-time average of Rydberg fraction in TDSE result. Red line is the result of Lindblad equation of 100 Monte-Carlo events. . . . .	77
4.18	Time dependence of $\sum_{i,j} \langle \hat{n}_i \hat{n}_j \rangle(t)/N^2$ measured for the linear chain of $N = 10$ . The experimental data (circles) are compared with the computation (solid lines) based on the Lindblad equation and also with the result (dashed) of the master equation constructed based on the experimental data. The errorbars are standard error of the mean. . . . .	78
4.19	Time average of $\sum_{i,j} \langle \hat{n}_i \hat{n}_j \rangle(t)/N^2$ at $t \geq t_{\text{relax}}$ as a function of system size $N$ for the linear chain (red circles) and the zigzag chain of $\theta = 60^\circ$ (blue diamonds). The errorbars of $\pm\sigma$ are shown. The theoretical results (solid lines) based on MPS are also shown. . . . .	79
4.20	Critical behavior of Rydberg fraction, $\bar{f}_R \sim \alpha^\nu$ , after reaching to the equilibrium as a function of $\alpha \equiv \hbar\Omega/ C_6 n_{\text{eff}}^6$ , where $n_{\text{eff}}$ is effective density of zigzag chain (see text). The experimentally measured critical exponent $\nu_{\text{exp}}$ is estimated with 95 % confidence interval of least-square fit. The y-axis, and x-axis errorbars are standard deviation of $\bar{f}_R$ , and fixed 200 nm distance error, respectively. N=15 for all data. . . . .	80
4.21	$n_{\alpha\alpha}(E)$ and $\rho(E)$ for the linear chain with $N = 19$ . Upper panel: The diagonal element $n(E)$ is supposed to be a smooth function of $E$ and constant over energy windows with width $\Delta$ , according to ETH. However, we see that $n(E)$ is not smooth. $\rho(E)$ is plotted after summing delta functions over small energy windows. If the system is quantum chaotic, $\rho(E)$ is expected to have a Gaussian centered at 0 with standard deviation $\Delta = 0.57$ . . . . .	82
4.22	$n_{\alpha\alpha}(E)$ and $\rho(E)$ for the zigzag chain with $N = 21$ and $\theta = 60^\circ$ . The diagonal element $n(E)$ is supposed to be a smooth function of $E$ and constant over energy windows with width $\Delta$ , according to ETH. However, we see that $n(E)$ is not smooth. $\rho(E)$ is plotted after summing delta functions over small energy windows. If the system is quantum chaotic, $\rho(E)$ is expected to have a Gaussian centered at 0 with standard deviation $\Delta = 0.6$ . . . . .	82
6.1	Current feed-back operational amplifier (OP-amp) for driving 50 Ohm load by using NI-6733 analogue pulse driver card. OP amp is TH-3001 current feed-back type from Texas Instrument. . . . .	90
6.2	Home-built circuit for AH coil switch. . . . .	90
6.3	Current control transient of bias coil. The blue line corresponds to the current switch given by analog pulse from NI PCIe-6353 device. The current per switching voltage is 2 A/V. The yellow line corresponds to the current of the coil, 2 V/A. The current driver model is Sorenson DLM60-10 with M51A option. . . . .	91

# Chapter 1. Introduction

Quantum physics has successfully explained the microscopic world. At the same time, its counter-intuitive nature has been at the center of controversy. For example, the seemingly unphysical statements such as Schrödinger's cat and Einstein Podolsky Rosen (EPR) paradoxes have brought up tremendous debates. It was natural that there have been elaborate efforts to clarify the nature of quantum mechanics. As results, the remarkable success of precision measurement [1] has confirmed the performance of quantum mechanics. Furthermore, the heart of quantum mechanics (superposition and entanglement) and the associated paradoxes have directly observed by many experiments [2, 3, 4, 5, 6], therefore its implications are barely arguable.

## 1.1 Personal viewpoint

The successful story of quantum mechanics owed to the capacities of controlling quantum systems precisely up to single quanta resolution [7]. Some of the representative quantum systems are briefly mentioned below.

Atoms are natural-born pure quantum systems. Especially their internal degree of freedom, such as quantized level structure of hydrogen atom, has long been under research subjects. Thank to the development of coherent sources of electromagnetic wave, the experimentalists could accurately control those atomic internal states [See. Ramsey, 1989 Nobel prize]. In other words, the coherent state of quantum systems could be prepared, and dynamics of those systems became a subject of a control theory, so-called coherent control [8, 9]. Its external degree of freedoms such as position and momentum also have been a research target. One of the key idea was an exchange of photons' and atoms' momentum; the laser cooling techniques have been well established [See. Nobel prize in Physics 1997]. Nowadays, one can achieve sub mili-Kelvin temperature of millions of atoms confined in a mili-meter size without much efforts. The confining potential for those atoms is the key ingredient for the quantization of position and momentum (quadrature fields). Its pedagogical example is a quantum harmonic oscillator. Further cooling techniques such as evaporative cooling [10] or Raman cooling [11] could cool down the atoms' motional states to the ground state; presumably the most famous example is Bose-Einstein condensation [See. Nobel prize in Physics 2001]. Many researches have extended the field to the observation of quantum phase in an optical lattice [12], or entanglement between atomic levels and external motions [13].

Photons are also a good quantum system as a quantum information carrier and processor. Its quantum nature was well organized by second quantization [14], and directly observed by the experiments [2, 15]. For example, discrete photon number states were observed by a cavity coupled atomic system, and superposition of coherent state (cat state) was generated [16].

At last but not least, there are still many different kinds of quantum systems such as superconducting qubits [17], quantum dot electron spins [18], and solid-state spins [19].

All the referred subjects are seemingly cooperative and converging together; for examples, tools of coherent control were suggested for achieving higher qubit fidelity [20, 21], single atoms and single photons were coupled thorough a cavity (cQED) [22], superconducting circuits and the other quantum systems were hybridized [23, 24], nano-photonic devices were coupled to atoms [25], and modular entanglement

of ions were performed by mediating photons [26], to list a few. Those various approaches are heading for common big goals such as developing quantum simulators, quantum computers, and new quantum technologies.

Quantum simulation is a concept that Feynman (universal quantum computer as the original term) proposed in early 1980's [27]. At that time, he already mentioned the universal quantum computer that designs a Hamiltonian and simulates real world physics. Since the world has quantum nature, the computer's simulating capacity should catch up the exponentially growing computational tasks with linearly increasing system size, otherwise the simulation would be impossible. Thus the computer also has to implement quantum nature as the world does. The idea have been implemented in various systems such as neutral atoms, ion trap, NV center, and superconducting qubits; there are many examples demonstrated in the last decade such as relativistic QED [28], magnetism [29, 30, 31, 32], thermalization and nonequilibrium dynamics [33, 34] especially addressing the issue; the gap between quantum statistics and classical statistical mechanics [35, 36].

For quantum computation, I barely refer the materials other than the famous algorithms that overwhelm the classical counterparts which are Shor's factoring [37] and Grover's searching [38] algorithms. Due to its predicted outperforming ability compared to that of classical computers, its physical implementation is vigorously ongoing project for many different platforms as well. Especially the error correction which is one of the key ingredients has demonstrated in ion traps [39] and superconducting qubits [40] recently. Those two platforms are seemingly promising candidates for realizing a quantum computer.

Quantum technologies have been an essential part for current industries and our lives; semiconductors, bio-imaging techniques (NMR, CT, PET, etc), and laser technologies are of the examples. New types of technologies such as quantum cryptography, computer, sensor, and biology are expected to come into play in the future [41].

## 1.2 In this thesis

In this thesis, a technique that may be useful in the future quantum technologies is developed and demonstrated. The technique is single-atom optical tweezers that was generated by dynamic phase holograms to transport single atoms ( $^{87}\text{Rb}$ ) in arbitrary ways [42, 43]. The technique demonstrated here can implement a bottom-up construction of atomic quantum systems. As a result, a Rydberg atom quantum simulation would be possible with larger scale [44]. Moreover, it has possible application for coupling single atoms with cavity and nano-photonic devices as well, yet those are out of my scope.

In Chapter 2, the relevant background knowledge such as laser cooling, single atom trapping, and experimental setup used in this thesis are introduced.

In Chapter 3, the single-atom transport by dynamic phase holograms and its application to deterministic loading of single-atom array are explained.

In chapter 4, Rydberg atom excitation and entanglement between trapped atoms through induced dipole-dipole interaction are explained. With the aid of the technique in Chapter 3, Rydberg atom quantum simulation is also performed.

## Chapter 2. Experimental background and setup

To build neutral atom quantum systems, several pre-requisites are required. One is ultra-high vacuum (UHV) system to maintain coherence of atoms because uncontrollable collisions with background gases or atoms themselves would destroy quantumness. The other condition is cooling and trapping of target atoms and resolving them to single quanta resolution. Cooling and trapping are essential for reducing inhomogeneous broadening and conducting reliable experiments. Resolving single quanta is also important in that a quantum system can be investigated one by one and its microscopic behavior is directly observable. In this chapter, achieving those pre-requisites as well as characterization of atomic samples is explained.

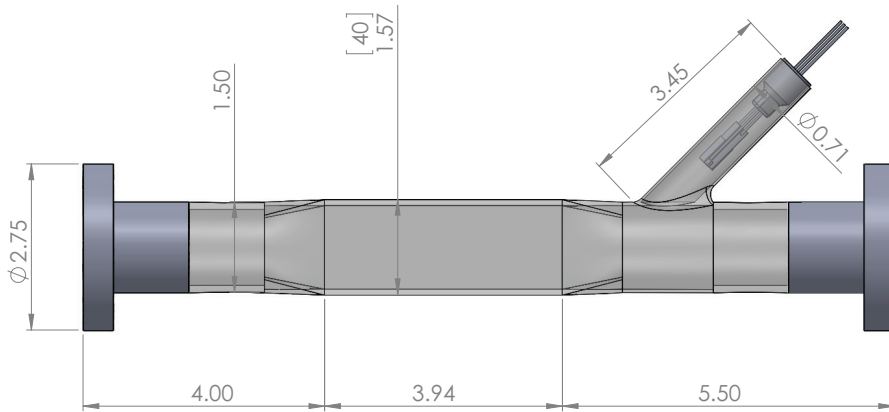


Figure 2.1: Vacuum glass cell. It is made of Pyrex. The clear window dimension is 100 mm  $\times$  40 mm  $\times$  40 mm located at the center, and the thickness is 3.5 mm. Both ends are mounted with rotatable 2.75 inch flanges and sealed with lead-like material, limiting bake-out temperature to 250 °C. The angled-arm on the right side has two Rb getters (SAES getters) for atoms supply. The getter should be initially baked out for 10 minutes with 4 A current during the entire chamber bake-out stage. The windows are one-side anti-reflection (AR) coated to 400-800nm range. It is a customized product from "Precisionglassblowing," USA.

### 2.1 Vacuum chamber

Nowadays, ultra-high vacuum (UHV) systems are commercially available. Thus achieving UHV regime for cold atoms experiments is easy and simple without knowing about the UHV material fabrication. For the minimal technical notes on the UHV, please read the articles [45, 46].

The purpose of the chamber shape in Figure 2.1 is to achieve high numerical aperture (NA) access from the outside toward the inside. It is essential for single atoms trapping. The key ingredient I had to consider was that the inside should be as clean as possible so that at least cold atoms can be reliably loaded and trapped for long enough time (at least several seconds). In addition to that, a high NA accessible port outside the vacuum was required for single atom manipulation. The possible approach was to choose a small size vacuum chamber as high NA access is usually limited to the distance from the inside objects and the outside lens. The conclusion was shown in Figure 2.1 which is a glass vacuum

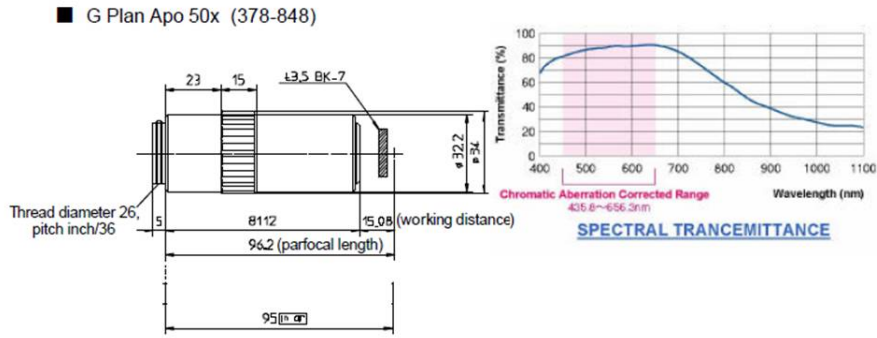


Figure 2.2: Objective lens for single atom experiments. High NA and outside vacuum chamber accessibility is simultaneously achieved by just adopting this commercial objective lens. One defect is color mismatch that diminishes the transmittance, yet it is affordable at around 800 nm wavelength. The lens is purchased from "Mitutoyo," Japan.

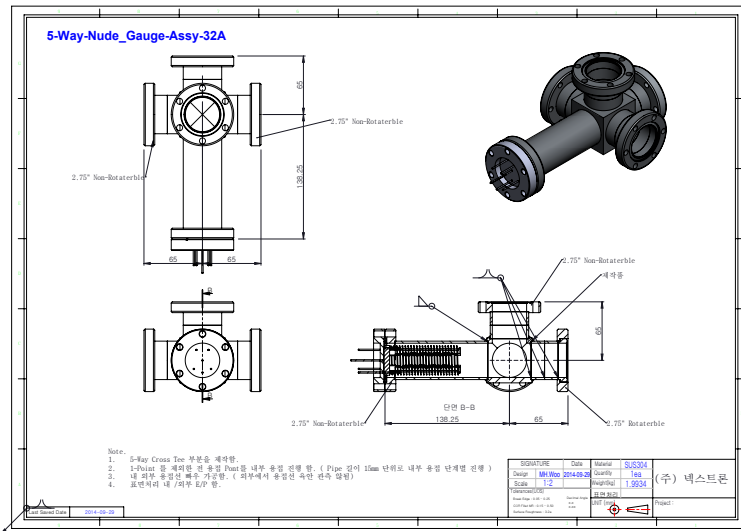


Figure 2.3: Customized 5-Way metal adaptor. Each way corresponds to the glass cell, ion gauge, ion pump, gate valve, and laser beam window, respectively.

chamber made of Pyrex.

Also, its simple structure (single component) makes it easy to assemble, and to combine additional components inside the chamber. The devices such as nano-fabricated chips inside the vacuum chamber are possibly advantageous for single atom trap due to its easy accessibility to high NA and accurate micro-nano sized fabrication technique [47, 48].

Higher the NA, shorter the working distance of the lens. The best option was the commercially available objective lens from Mitutoyo, G plan Apo 50X. The lens has 0.5 NA, 16 mm long working distance including 3.5 mm thick glass plate compensation, infinite conjugated, planar image area above  $200 \mu\text{m}^2$ . My target wavelength ranged from 780 nm to near-infra red (NIR) due to choice of atomic species,  $^{87}\text{Rb}$ . Thus a defect for choosing the lens was a mismatched color aberration correction. More on that, the anti-reflection (AR) coating of the lens was limited to visible range thus transmission decreases from 90 % at 600 nm to 60 % at 780 nm and 50 % at 820 nm. Note that the glass cell in Figure 2.1 had a dimension of 40 mm thus only one-sided access for objective lens was possible. Thus spatial aberration



Figure 2.4: The completely assembled vacuum chamber. The periphery of optics are also shown as well.

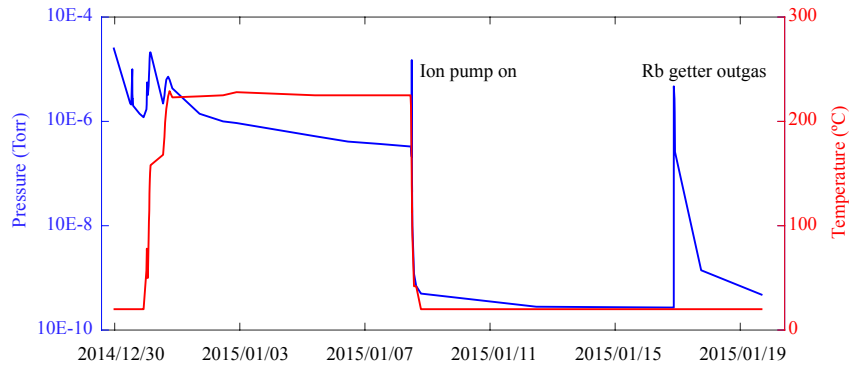


Figure 2.5: The measured pressure inside the chamber, with bake-out temperature.

correction of dipole trap inside the vacuum was limited due to lack of observation port.

Definitely, only glass cell was not enough for the entire vacuum systems. The cell's 2.75 inch flange of the right hand side in Figure 2.1 was sealed with a zero length viewport, anti-reflection V-coat at 780 nm, purchased from "Huntington Mechanical Lab". The other side of the cell was connected to the metal adaptor in Figure 2.3. The metal adaptor had 5-way 2.75 inch flange which are a view-port for 780 nm beam window, gate valve, ion gauge, ion pump, and the glass cell, respectively. The fully assembled vacuum system is shown in Figure 2.4.

The pressure inside the cell was measured during the whole preparation process as shown in Figure 2.5. At first, only turbo molecular pump (Varian, V-70) was used. The pump has a built-in rotary pump for pre-pumping stage. Below  $10^{-5}$  Torr was achieved within a day. Then the bake-out stage had started. The heating tapes was used for it. After packaging the entire chamber with the tapes, about two layers of aluminium foils covered the chamber again for thermal insulation and distribution. The baking temperature was carefully maintained below the chamber limit of 250 °C. After a few days, the baking ended and ion pump was turned on. The pressure rapidly decreased within a day to a few  $10^{-10}$  Torr. Unfortunately, the Rb getter inside the chamber wasn't baked out properly. The UHV level had to be

broken in order to bake out the getter. After then, the UHV regime could be rapidly recovered again. The history graph of the vacuum level and bake-out temperature is shown in Figure 2.5. The required amount of Rb can be maintained without driving the getter for several months if the adsorbed Rb atoms are enough. The experiments in this thesis have done by the setup in Figure 2.4.

## 2.2 Cooling and Trapping of Rb atoms

The operation procedure of the magneto-optical trap (MOT) is briefly summarised below. Note that the experiments were performed in the sub-Doppler cooling regime [49].

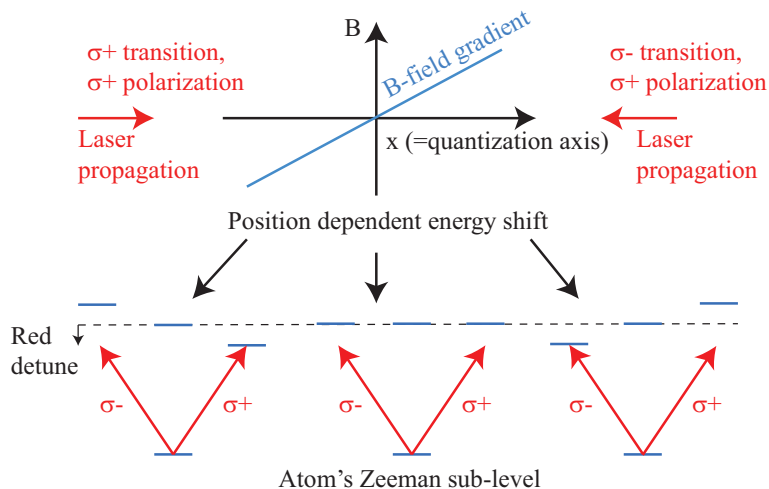


Figure 2.6: The principle of Magneto-optical trap (MOT).

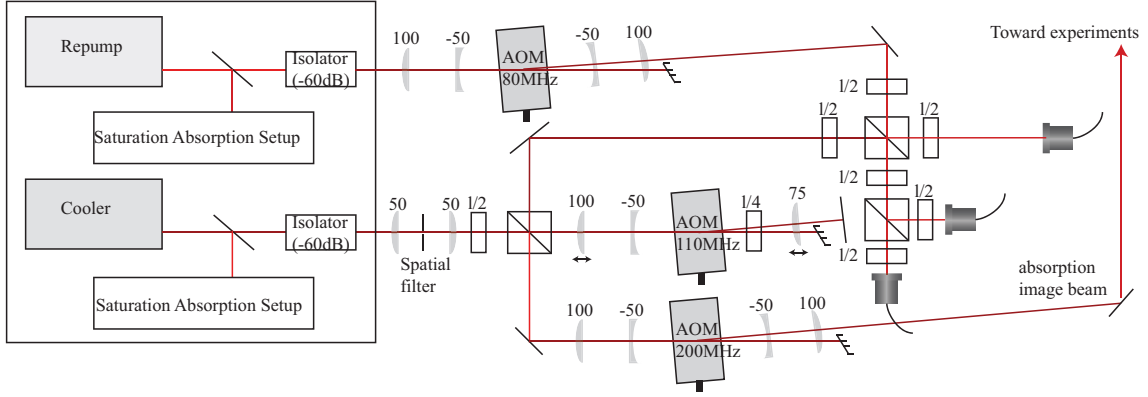
The atoms cooling mechanisms rely on the momentum exchange between atoms and photons. One can imagine the situation that atoms absorb photons resonantly from one direction, and then spontaneously decay to every direction. The expected result is that atoms lose their momentum to the direction where the photons are coming. To this happens in all directions, magneto-optical trap (MOT) is utilized; In Fig. 2.6, a magnetic field gradient is introduced. For the 3D field gradient, an anti-Helmholtz coil configuration is utilized. According to the gradient, atoms feel different Zeeman splitting at the position. The slightly ( $\sim -2\Gamma$  where  $\Gamma$  is spontaneous decay rate of a given level) red-detuned lasers with the given polarization counter-propagate. Due to the Zeeman splitting and the corresponding resonance condition, atoms are cooled down by the momentum exchange and at the same time, they are collected at the zero-field region.

### 2.2.1 MOT characterization

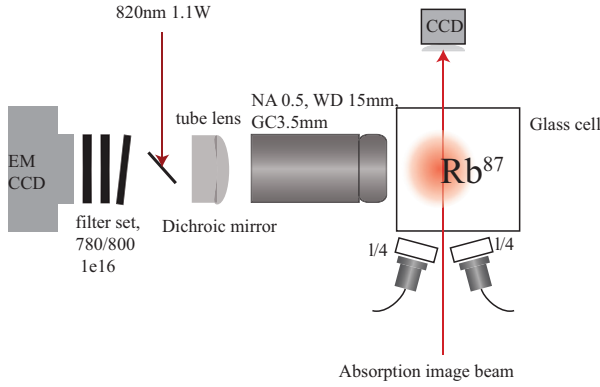
Fig. 2.7(a) shows the optical setup for the MOT. For  $^{87}\text{Rb}$  MOT, two 780 nm lasers are used; one is for cooling and the other is for repumping. The cooling laser is a commercial (Moglab, CEL002) diode laser and the repump laser is a home-built external-cavity diode laser (ECDL). Each laser is frequency swept by acousto-optic modulators (AOM). Fig. 2.7(b,c) show the single-atom trap setup. A high NA objective lens is placed for single-atom dipole trap.

Figure 2.8(a) shows the control parameters and their time sequence for the MOT. The cooler intensity 1 corresponds to each arm of the six-beam having an intensity of  $8 \text{ mW/cm}^2$ . As the cooler detuning increases, its intensity

(a) Optics setup



(b) Chamber top view



(c) Chamber side view

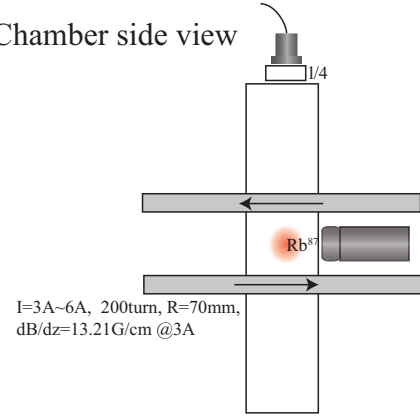


Figure 2.7: MOT and characterization setup overall. (a) optical alignment parts. (b) Chamber top view. The microscope imaging parts are for micro optical dipole trap which will be discussed in the next section. (c) Chamber side view. The relevant parameter for Anti-Helmholtz (AH) coils are presented.

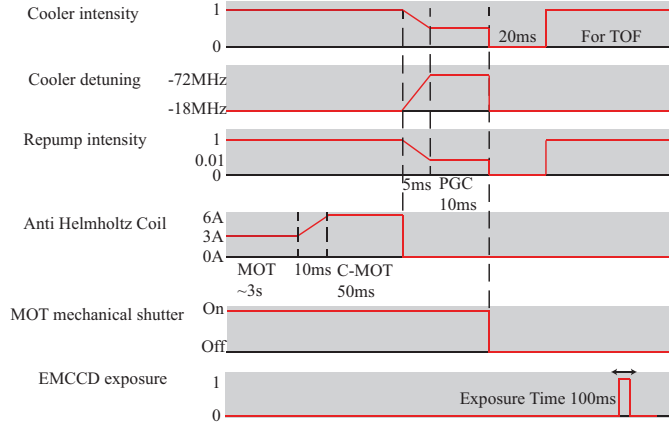
decreases because the detuning is controlled by double pass AOM configuration [50]. The decreased intensity is  $2.5 \text{ mW/cm}^2$  at the highest detuning. The magnetic field gradient  $dB/dz$  is  $12 \text{ G/cm}$  at  $3 \text{ A}$  coil current.

After shutting down the MOT, the atomic cloud freely expands and falls; the method was utilized to measure the temperature of MOT [51]. The expanded cloud size is given by

$$\sigma(t) = \sqrt{\sigma(0)^2 + \frac{k_B T}{m} t^2} \quad (2.1)$$

as a function of time. Meanwhile, the center of the cloud has the speed,  $v_c = gt$ . If falling time,  $t_0$ , is known and it is assumed that the  $t_0$  is long enough compared to the cloud transit time, the cloud size  $\sigma_z$  is given by  $\sigma(t_0) = v_c \sigma_z$ . The temperature can be measured from Equation. 2.1. The initial cloud size is usually negligible with the long enough time of flight (TOF) time. The TOF beam which comes from the same cooler laser has  $100 \mu\text{W}$ , and  $1 \text{ mm}$  beam diameter.  $30 \mu\text{W}$  repumper is used as well. It is focused by  $f=100 \text{ mm}$  cylindrical lens and counter-propagated below  $2 \text{ cm}$  of the MOT, The focused beam waist is measured as  $200 \mu\text{m}$ . The EMCCD captures the fluorescence image of the TOF beam as a function of free fall time of the cloud. The exposure time is  $100 \mu\text{s}$  fixed. The image and its fluorescence vs. fall time are shown in Figure 2.9(a). Figure 2.9(a) is a measured TOF image

(a) Experiments sequence



(b) Time of Flight

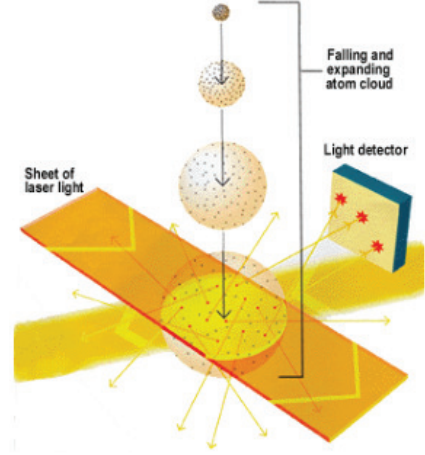


Figure 2.8: (a) MOT pulse and MOT characterization sequence time table. (b) Time of Flight measurement scheme from Ref. [51].

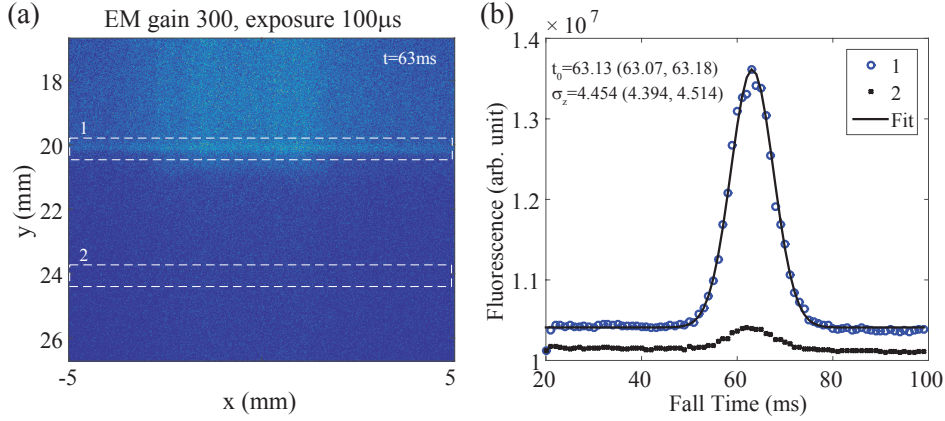


Figure 2.9: MOT characterization results. (a) Time of Flight image from the camera. The falling time is 63 ms. (b) The white dotted square box in (a) is summed over and plotted as a function of time. The label 2 is for background compensation to estimate the atom number.

after a falling time 63ms. The white dotted box with numbers 1, and 2 are regions of interest (ROI) for TOF signal and background, respectively. In Figure 2.9(b), each data points are the summation of the ROI as a function of time. The blue empty circles with fitting curve are TOF signal and its gaussian fitting,  $a \exp\{-\frac{(t - t_0)^2}{2\sigma_z^2}\} + b$ . The black dots are background signal. The resulting temperature is 20.1 (19.5 20.6)  $\mu\text{K}$ . The error is  $1\sigma$  fitting uncertainty. Note that polarization gradient cooling (PGC) [49] is done for this setup.

From the background signal of Figure 2.9(b), the absolute zero floor is acquired. Thus the ratio between the cold atom fluorescence and that of background thermal atom could be estimated as 9. The thermal atom pressure is  $1.3 \times 10^{-9}$  Torr (2.8 A getter current) and the volume of the ROI is  $2 \text{ mm}^3$ . From the ideal gas equation of state,  $PV = Nk_B T$ , the expanded cloud atom number involved with fluorescence emission is estimated as  $7.7e5$  from Figure 2.9(b). The gaussian width is measured as 2.8mm. The width estimated from Figure 2.9(a) is also similar with it. Under the assumption that the expanded cloud is sphere shaped,  $\exp\{-\frac{(x^2 + y^2 + z^2)}{2\sigma(t_0)^2}\}$ , and the TOF beam penetrates

exactly the center of the sphere, The portion of fluorescent cold atoms among the whole cold atoms is calculated from

$$\frac{\int_{-\infty}^{\infty} e^{-x^2/2\sigma^2} dx \int_{-0.5 \text{ mm}}^{0.5 \text{ mm}} e^{-y^2/2\sigma^2} dy \int_{-0.1 \text{ mm}}^{0.1 \text{ mm}} e^{-z^2/2\sigma^2} dz}{\int \int \int_{-\infty}^{\infty} e^{-(x^2+y^2+z^2)/2\sigma^2} dx dy dz} = 0.00404 \quad (2.2)$$

where  $\sigma = 2.8 \text{ mm}$ . Thus the whole cold atoms number is estimated as  $1.91 \times 10^8$ , and its density is  $3.6 \times 10^{11} / \text{cm}^3$  for the initial MOT diameter, 1 mm. The estimated density is seemingly too high for conventional MOT. For more rigorous density measurement, absorption imaging technique would be required.

## 2.3 Optical Dipole Trap

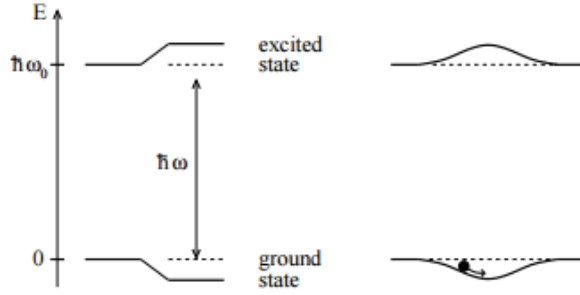


Figure 2.10: The AC Stark shift of two level system. Its representation has adopted from Ref. [52].

The optical dipole trapping (ODT) technique has widely used for atomic physics [52]. The basic physical principle is that AC Stark shift generates optical potential. First of all, a two-level pedagogical example is described here. A two-level Hamiltonian  $\hat{H}_0$  with energy separation  $\hbar\omega_0$  and interaction Hamiltonian  $\hat{H}_I$  by dipole field is given by

$$\hat{H} = \hat{H}_0 + \hat{H}_I = \begin{pmatrix} 0 & -\mu E \cos \omega t \\ -\mu E^* \cos \omega t & \hbar\omega_0 \end{pmatrix} \quad (2.3)$$

Note that optical phase offset can be omitted without loss of generality. If we deliver the Hamiltonian  $\hat{H}$  to the interaction picture [53] or rotating frame of  $\omega$ , the new Hamiltonian is given by

$$\begin{aligned} \hat{H}' &= \hbar \begin{pmatrix} 1 & 0 \\ 0 & e^{i\omega t} \end{pmatrix} \begin{pmatrix} 0 & -\frac{\mu E}{2\hbar} (e^{i\omega t} + e^{-i\omega t}) \\ -\frac{\mu E^*}{2\hbar} (e^{i\omega t} + e^{-i\omega t}) & \omega_0 - \omega \end{pmatrix} \begin{pmatrix} 1 & 0 \\ 0 & e^{-i\omega t} \end{pmatrix} \\ &= \hbar \begin{pmatrix} 0 & -\frac{\mu E}{2\hbar} \\ -\frac{\mu E^*}{2\hbar} & -\Delta \end{pmatrix} \end{aligned} \quad (2.4)$$

where  $\Delta = \omega - \omega_0$  and the rotating wave approximation (RWA) is applied to the final result. One can easily notice that it is the general Rabi oscillation Hamiltonian. The eigenvalues and eigenstates are calculated as

$$\begin{aligned} \text{Eigenvalues} & \left( \frac{\mu^2 |E|^2}{4\hbar\Delta}, -\hbar\Delta - \frac{\mu^2 |E|^2}{4\hbar\Delta} \right) \\ \text{Eigenstates} & \left( 1 - \frac{\mu^2 |E|^2}{4\hbar^2 \Delta^2}, \begin{pmatrix} \frac{\mu E}{2\hbar\Delta} \\ 1 - \frac{\mu^2 |E|^2}{4\hbar^2 \Delta^2} \end{pmatrix} \right) \end{aligned} \quad (2.5)$$

under the assumption that  $\hbar|\Delta| \gg \mu|E|/2$  which is far-detuned case. If the rotating frame  $\omega$  is reversed again, the second Eigenvalue becomes  $\hbar\omega_0 - \mu^2|E|^2/4\hbar\Delta$ . Figure 2.10 represents those Eigenvalues and Eigenstates. Note that the Eigenstates can be treated as that of bare Hamiltonian  $\hat{H}_0$  under the adiabatic approximation. If the detuning  $\Delta$  is negative, the light is red-detuned. As a result, the ground state is attractive to the light intensity maximum and the excited state is repulsive. The blue-detuned light is the opposite case. The ground state dipole potential is defined as  $U_{dip} = \mu^2|E|^2/4\hbar\Delta$ . The first order term of the Eigenstates shows that there are small amount of upper state population  $\mu^2|E|^2/4\hbar^2\Delta^2$ . Accordingly, the scattering rate is  $\Gamma_{sc} = \Gamma\mu^2|E|^2/4\hbar^2\Delta^2$  where  $\Gamma$  is spontaneous decay rate. The relation

$$\hbar\Gamma_{sc} = \frac{\Gamma}{\Delta}U_{dip} \quad (2.6)$$

is acquired. As  $\Delta$  increases, the light potential induced scattering rate  $\Gamma_{sc}$  is suppressed compared to  $U_{dip}$ . Thus we may assume that far-detuned dipole trap is conservative potential.

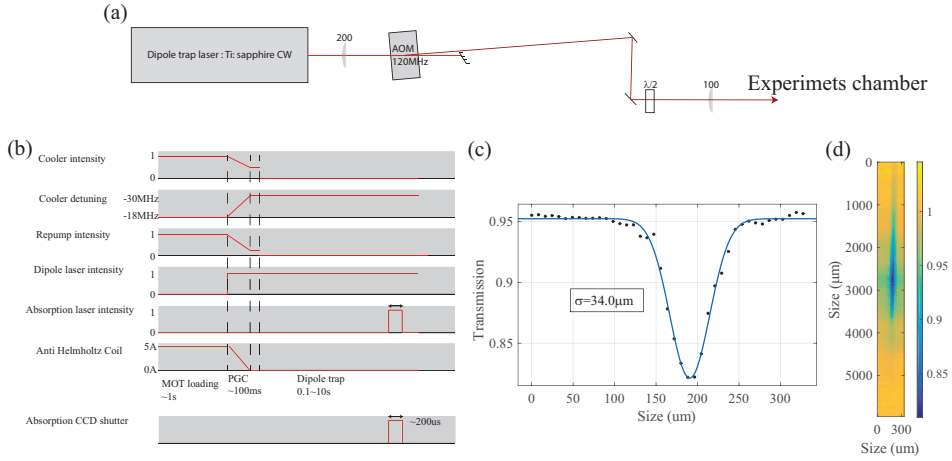


Figure 2.11: (a) Dipole trap laser optical parts. These parts are additional to Figure 2.7(a). The microscope imaging parts in Figure 2.7(b) are replaced to these. (b) The pulses and trigger timing sequence for ODT absorption imaging experiments. (c) An absorption profile of ODT in radial direction. (d) An absorption image of ODT.

We first demonstrate a large volume ODT setup in Figure 2.11. The dipole trap laser in Figure 2.11(a) has 1.1 W diffracted laser power and 810 nm wavelength; thus, the estimated peak trap potential was 760  $\mu\text{K}$ .

The experimental time sequence was similar to that of Figure 2.8. In this experiment, the absorption image of trapped atoms was captured. The absorption beam had 7.5 mm diameter, 0.1  $I_s$  intensity where  $I_s$  is saturation intensity of  $^{87}\text{Rb}$  F=2 to F'=3 cycling transition. The absorption pulse duration is less than 200  $\mu\text{s}$ . From the absorption image, one can recover the atomic density. The formula is,

$$\log \frac{I_f}{I_i} = -\sigma_{eg} \int n_0 e^{-x^2/2\sigma^2} dx \quad (2.7)$$

where  $I_f$ ,  $I_i$  are final and initial intensity of absorption beam, respectively,  $\sigma_{eg}$  is resonant cross section given by  $\sigma_{eg} = \hbar\omega\Gamma/2I_s = 290.7 \times 10^{-15} \text{m}^2$ ,  $n_0$  is atom density, and  $\sigma$  is Gaussian width of the absorption profile in Figure 2.11(c). Note that homogeneous density of the atomic cloud is assumed. As a result, the estimated density is  $n_0 = 0.55 \times 10^9 \text{cm}^3$ . Note that the density decay time was only a few second, and faster than exponential decay. It is due to two-body inelastic collisional loss [52] but the detail will be discussed later.

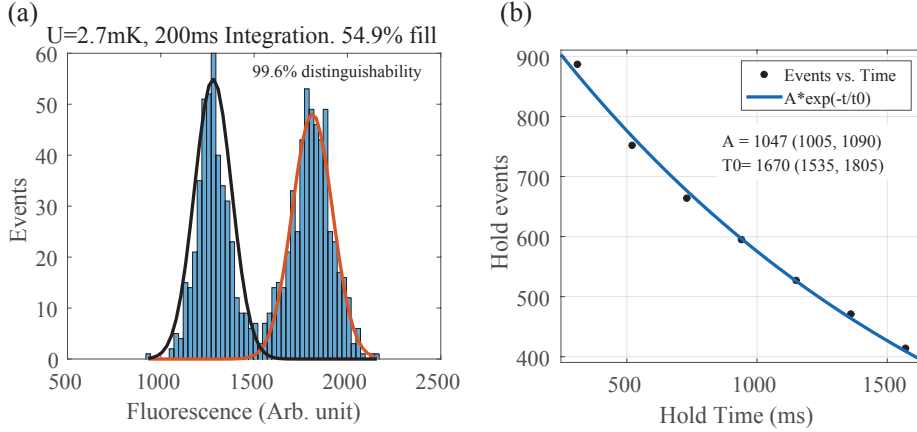


Figure 2.12: My single atom loading results. (a) its histogram. (b) Single atom loss curve.

Many atoms are easily trapped inside ODT as shown above.

How can we achieve single-atom ODT then? Amazingly, single-atom trapping inside the ODT is just as simple as those many atoms ODT.

### 2.3.1 The single-atom optical dipole trap

In 2001, single atom loading inside a micrometer size dipole trap was demonstrated [54]. The reference observed that 50 % of one atom and 50 % of zero atom loading was possible in the micrometer size ODT. There were no more than two atoms loading inside micro-ODT. The mechanism of such a sub-Poissonian loading was discussed in Ref. [55]. The mechanism is now called "collisional blockade"; Initially many atoms inside the micro-ODT collide with each other. By overlapping the PGC beam (red-detune) for cooling them, they rapidly (within a few micro seconds) photo-associated with each other by forming a dimer and the dimer escaped from the trap. This two-body trap loss mechanism is dominant in the micro-ODT. As a result, only one or zero atom remained in the trap.

The photo-association has two energy branch [56]; one is attractive and the other is repulsive. The attractive branch is accountable for the two-body loss when the red-detune lasers are used. The repulsive branch can be utilized to control the loss mechanism [56]; Instead of two-body loss, by using blue-detune lasers, one can introduce one-body loss in the micro-ODT. As a result, high efficiency (> 80%) single-atom loading inside the micro-ODT was demonstrated [56].

In this experiment, only red-detune lasers have used for single-atom loading. One of the early result is shown in Fig. 2.12. The single-atom trap probability was measured as 55 %. Even though the blue-detune laser isn't utilized, it already exceeds 50 %, suggesting that there are some one-body loss mechanism other than that. The lifetime of single-atom trap was only 1.5 s. The lifetime could be optimized in the later experiment, reached to 40 s.

### 2.3.2 Characterization of the single-atom trap

The single-atom trap is generated by red detuned, highly focused Gaussian beam. In this case, the trap potential can be approximated as [52],

$$U(r, z) \approx -U \left[ 1 - 2 \left( \frac{r}{w_0} \right)^2 - \left( \frac{z}{z_R} \right)^2 \right] \quad (2.8)$$

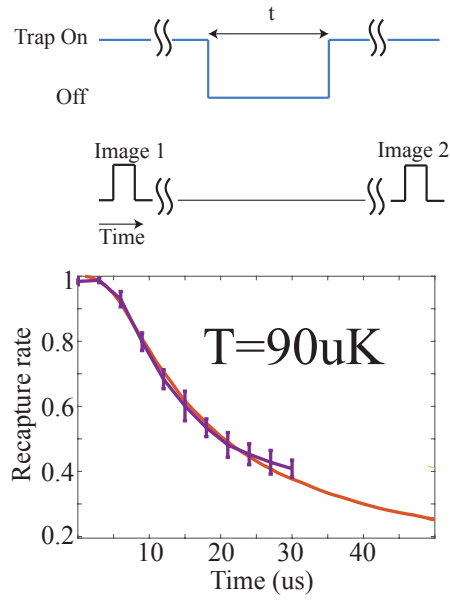


Figure 2.13: Measured single atom temperature by release and recapture method presented in Ref. [57]. My measurement pulse sequences are shown.

where  $w_0$  is the Gaussian beam waist at the focal point,  $z_R$  is the Rayleigh length, and  $U$  is the trap depth for the atoms. Note that the trap depth calculation code for Matlab is shown in Chapter 6, Appendix.

The trap potential is a 3D harmonic potential, with trap frequencies  $\omega_r = (4U/mw_0^2)^{1/2}$  for radial and  $\omega_z = (2U/mz_R^2)^{1/2}$  for axial direction. The atom temperature inside the trap and the radial trap frequency can be measured in the experiment [57, 58]; for the atom temperature, release and recapture method [57] is used. The experimental result in Fig. 2.13 is fitted by a Monte-Carlo method. For the radial trap frequency, double release and recapture method [58] is used. The experimental result in Fig. 2.14 is fitted by exponential decaying cosine curve. The exponential decay is due to trap inhomogeneity from the Harmonic potential approximation and high atom temperature.

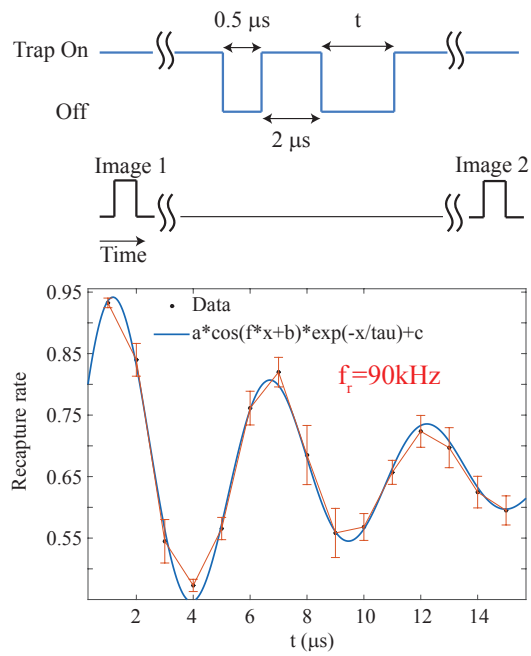


Figure 2.14: Measured single atom trap frequency in radial direction. The method was presented in Ref. [58]. My measurement pulse sequences are shown.

## Chapter 3. Dynamic phase holograms for single atom optical traps

### 3.1 Spirit of the approach

Laser cooling and trapping of atoms has enabled the construction and manipulation of quantum systems at the single-atom level [59, 60, 61, 62, 63, 64, 65, 66, 67]. To create scalable and highly controllable quantum systems, e.g., a large-scale quantum information machine, further development of this bottom-up approach is necessary. The implementation of these systems has crucial prerequisites: scalability, site distinguishability, and reliable single-atom loading onto sites. The previously considered methods [68, 69, 70, 71] satisfy the two former conditions relatively well; however, the last condition, loading single atoms onto individual sites, relies mostly on probabilistic loading, implying that loading a predefined set of atoms at given positions will be hampered exponentially. Two approaches are readily thinkable to overcome this issue: increasing the single-atom loading efficiency [72, 73, 74, 75] and relocating abundant atoms to unfilled positions [76, 77]. Realizing the atom relocation idea, in particular, is directly related to how many atoms can be transportable independently and simultaneously.

In that regards, using holographic optical tweezers is advantageous because arbitrary potentials can be designed for atoms [64, 70]. The optical tweezers are the image determined by the wave propagation integral, e.g., Fourier transformation (FT), so the hologram for a complex potential can be designed using a numerical method often based on iterative FT algorithms (IFTAs) [70]. When being used in conjunction with an active holographic device such as spatial light modulators (SLM), the algorithms can produce dynamic optical potentials, of which the many applications include dynamic in situ atom manipulation [78, 79, 80, 81], quantum logic gate [82], pattern formations in an addressable optical lattice [77], and real-time feedback transportation of atoms [65]. However, there has been no scheme implemented for the rearrangement of many atoms, with the full degree of control ( $2N$  for  $N$  atoms) in two dimensional (2D) space.

### 3.2 The proof-of-principle: random mask algorithm

In the below, I demonstrated a dynamic holographic single-atom tweezer with unprecedented degrees of freedom of  $2N$ . In a proof-of-principle experiment conducted with cold  $^{87}\text{Rb}$  atoms, simultaneous rearrangements of up to  $N = 9$  single-atoms were successfully performed. This method may be further applicable to deterministic  $N$  single-atom loading, coherent transport [78, 79], and controlled collisions [80, 81].

#### 3.2.1 Experimental concept and flicker-free beam steering algorithm

Figure 3.1 shows the concept of our experiment and the first demonstration of  $N$  single-atom transport with  $2N$  motional degrees of freedom. The set-up consists of an active holographic device (LC-SLM), an imaging system, and a cold  $^{87}\text{Rb}$  atom chamber, as shown in Figure. 3.1a. When the holograms were transferred by a two-lens system to the entrance pupil of a high numerical aperture ( $\text{NA} = 0.5$ ) lens [70], the optical tweezers had a beam radius of  $w_o = 1.14 \mu\text{m}$ , and the trap frequencies

were measured as  $f_r = 100$  kHz and  $f_z = 17$  kHz for radial and axial directions, respectively [57]. The temperature of the trapped atoms was measured as  $T = 110(10)$   $\mu$ K using the release and recapture method [58], where the error was the  $1\sigma$  band of each optical tweezer.

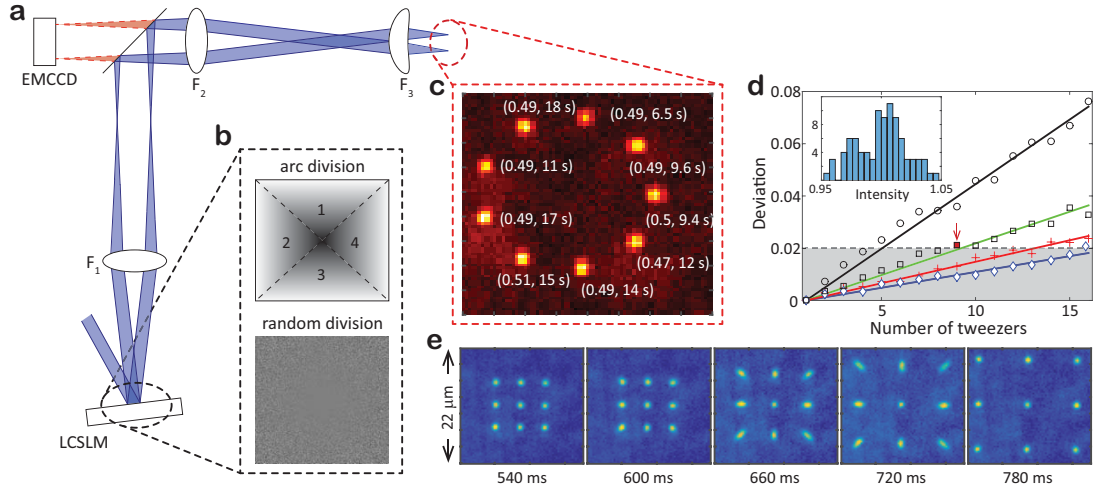


Figure 3.1: **Set-up for single-atom holographic transport.** **a**, The optical system for hologram transfer and trap imaging. **b**, Schematic 2D phase planes of the liquid crystal spatial light modulator (LC-SLM) in gray scale. One of them intuitively illustrates the working principle (arc division), and the other shows real hologram (random division), respectively. **c**, An example of loaded single atoms in a tweezer array, represented with  $22 \times 22 \mu\text{m}^2$  size 500 cumulative images. The parenthesis denotes the loading probability and life time. **d**, The intensity standard deviation as a function of  $N_t$  for the random division. The data points were calculated for various beam waists  $W$  at the SLM window (circles for  $W = 1$  mm, squares for 2 mm, crosses for 3 mm, and diamonds for 4 mm) and the solid lines are the linear fits to the data. The inset presents the intensity histogram of  $W = 2$  mm for  $N_t = 9$  of the red mark. **e**, An in situ single-atom array expansion movie.

Schematic examples of our trap generation algorithm are represented in Figure. 3.1b. Our algorithm uses the simplest analytic form of beam steering, *i.e.*, the linear phase  $\phi(x) = k_x x$ . This phase modulation directly couples the modulation plane (Fourier domain) control parameter,  $k_x$ , to the image plane position,  $X = Fk_x/k$ , with one-to-one correspondence, where  $F$  is the lens focal length and  $k$  is the wave-vector of the trap light. Then, the given function becomes a flicker-free solution, because a linear combination of two phases,  $\alpha k_1 x + (1 - \alpha)k_2 x$  with  $\alpha \in [0, 1]$ , is again a linear phase which smoothly sweeps the two focal points,  $X_1 = Fk_1/k$  and  $X_2 = Fk_2/k$  (see Methods for more details). To obtain more than a single optical tweezer, the modulation plane is divided into several sub-planes as in Figure. 3.1b [83]. When each sub-plane is assigned to each linear phase and the division is randomized in the single-pixel resolution of the device, this method effectively preserves the diffraction limit of the individual optical tweezers focused onto the image plane. Note that the required trap laser power in this manner scales with  $N_t^2$ , where  $N_t$  is the number of optical tweezers, so it is inefficient compared to the IFTA, which scales with  $N_t$  because the IFTA coherently sums over the entire modulation plane for every tweezer. Nevertheless, the proposed algorithm concedes power efficiency for independent controllability.

### 3.2.2 Simultaneous transport of $N$ single atoms

An image accumulating 500 snapshots from different loading events is shown in Figure. 3.1c. The 3D molasses continuous imaging [68, 84] captured a snapshot every 60 ms with 50 ms exposure time, where the single-event atom visibility exceeded 99.99%. If  $N_t$  increase, the number of SLM pixels per single optical tweezer would decrease, thus degrading the optical tweezer shape and intensity regularity. In Figure. 3.1d, the deviation of the normalized peak intensity  $\delta$  (the y-axis) is given proportional to the number of tweezers  $N_t$  (the x-axis) and inversely proportional to the beam waist  $W$ , i.e.,  $\delta \propto (N_t - 1)/W$ . This behavior can be understood as following: The peak intensity of each tweezer follows the binomial distribution  $B(M, 1/N_t)$ , where  $1/N_t$  is the success probability and  $M \approx W^2$  is the number of active SLM pixels, so the normalized variance is given by  $\bar{\sigma} = \sigma/\mu = \sqrt{(N_t - 1)/M}$ , where the mean and variance are  $\mu = M/N_t$  and  $\sigma^2 = M(N_t - 1)/N_t^2$ , respectively. In addition, there are  $\sqrt{N_t - 1}$  events that equally contribute to this normalized variance, so we get  $\delta \propto (N_t - 1)/\sqrt{M} \propto (N_t - 1)/W$ . To maintain an acceptable quality of the optical tweezers for the experiments, we chose  $N = 9$  and  $W = 2$  mm (the beam waist), limited by the laser power and relay optics dimensions, respectively. In our experiment, the standard deviation of the normalized peak intensity below 0.02 is tested, and a setup with a bigger laser power would support more optical tweezers. Note that, because of the  $N_t^2$  power-scaling, diffused light will eventually wash out the tweezer potential and the maximally available tweezers in our method is estimated to be  $N_t^{\max} = 100$ . Figure 3.1e shows an array-rearrangement demonstration. The series of images each accumulating also 500 snapshots of the individual experiments demonstrates that the initially prepared 3-by-3 square array of single atoms with a spacing of  $d = 4.5$   $\mu\text{m}$  expands to an array of twice the lattice spacing of  $2d$ . Figure 3.2 shows a single-atom transport example; in this case,  $N$  single atoms are moved from an initial array along a predefined path. Because each atom moves in 2D with parameters  $(X_i, Y_i)$  for  $i = 1$  to  $N = 9$ , the total degrees of freedom of movement is  $2N = 18$ .

### 3.2.3 Single-atom array synthesis demonstration

A proof-of-principle demonstration of the in situ single-atom array synthesis is presented in Figure. 3.3. In a three-step feedback loop of initial atom loading in  $N_{\text{init}} = 9$  sites, read-out, and rearrangement, as shown in Figure. 3.3a, an atom array of  $N_{\text{final}} = 1, 2, 3,$  or  $4$ , is produced. After the atoms are initially loaded at the sites, the first computer checks the occupancy of each site by reading out the electron multiplying charge-coupled device (CCD) images. A 9-bit binary information that represents the occupancy is then sent to the second computer, which has a look-up table (LUT) of atom rearrangement trajectories, each stored in DRAM as a sequence of 30 holograms, between all possible initial and final pairs of atom arrays. It takes 0.6 seconds from the read-out to the retrieval of an appropriate trajectory (Note that, using a fast graphic processing unit greatly can reduce this time and also make the LUT unnecessary [85]). Then, the second computer sequentially loads the holograms to the SLM at a speed of 30 frame-per-second to move the atoms along the trajectory. The initial, and four types of final cumulative images are represented by the atom number histograms in Figures. 3.3b and 3.3c. The individual final images are independent experiments that form one, two, three, or four atom arrays out of nine.

Compared with the binomial distribution of the initial histogram, the final histogram in Figure. 3.3d has non-Poissonian distribution. The loading efficiency curves of the final arrays are presented with red points for the data from the number histograms of at least 500 events. The black dotted line follows  $0.5^N$ , which is the loading efficiency in the collisional blockade regime, and the blue dashed line follows

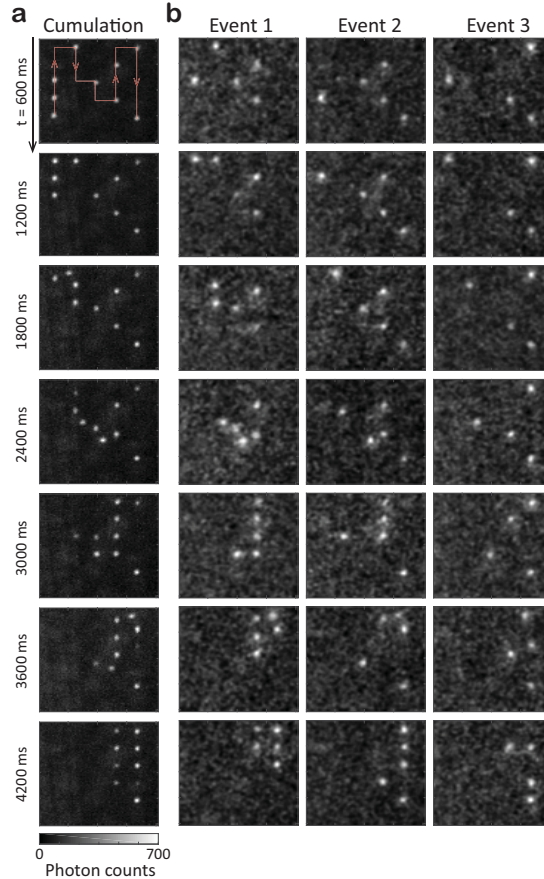


Figure 3.2: **Single-atom transport example.** **a**, Transient cumulative images of 500 snapshots showing that nine atoms move the predefined path (red arrows) sequentially. **b**, Three selected single events having four atoms or more. Every snapshot represents the same  $26 \times 26 \mu\text{m}^2$  area. The images are Gaussian-filtered for clarity.

the cumulative binomial distribution given by

$$P_{\text{lim}}(N) = \sum_{n=N}^9 \binom{9}{n} p^n (1-p)^{9-n}, \quad (3.1)$$

and the red line is

$$P_{\text{exp}}(N) = P_{\text{lim}}(N) \times p_s^N, \quad (3.2)$$

where  $p = 0.48$  is the initial loading probability and  $p_s = 0.86$  is the experimental (moving) success probability from the fitting.  $1 - p_s$  is composed of the background collisional and moving losses. During the entire feedback process, the background collisional loss is estimated to be 0.13 and the moving loss is estimated to be 0.01. The moving success rate, as expected, has high fidelity and a deterministic transport has been reliably completed. The  $N_{\text{final}} = 4$  case exhibits six-fold enhancement in loading efficiency, compared with the  $p = 0.5$  collisional blockade regime.

### 3.2.4 Discussion

The physics behind this demonstration is the capability of holographic optical tweezers to sustain trapped atoms while the hologram is being actively updated, but this has been considered impossible

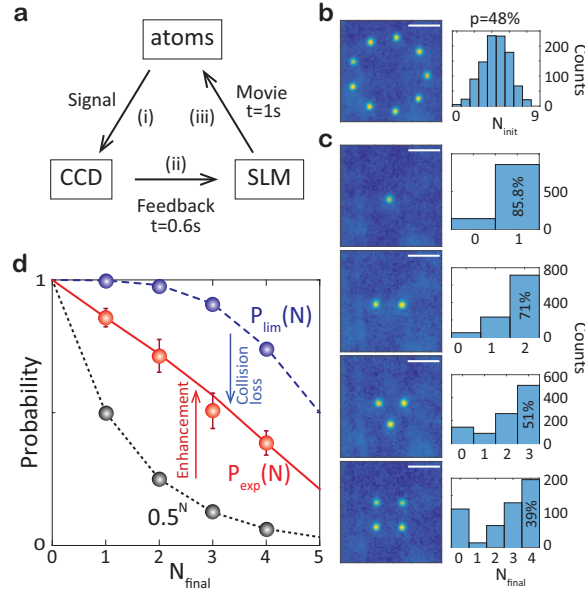


Figure 3.3: **In situ single-atom array synthesis.** **a**, The feedback-control loop sequence: (i) signal gathering and processing with a charge-coupled device (CCD), (ii) state resolving and solution finding, (iii) solution execution with a spatial light modulator (SLM). **b**, The cumulative image of initially loaded  $N = 9$  atoms (left), accompanied by the corresponding number histogram (right), where the scale bar size is  $5\ \mu\text{m}$ . **c**, From the initial 9 sites, one, two, three, and four atoms are rearranged through single feedback loop. **d**, Success probabilities of the atom rearrangement:  $p = 0.5$  (black dotted line), experiments (red line and data points), and theoretical limit (blue dashed line). The error bar depicts the standard deviation of time-binned 100 events.

because of intensity flickering [86, 87]. If conventional IFTAs are used to generate individual holograms to form the required optical potentials, the frame-to-frame evolution does not necessarily maintain an appropriate in-between potential (see Figure. 3.4a). While the intensity flickering is not an issue for macroscopic particles suspended in a solution [88], microscopic particles (e.g., atoms) do not wait until the missing potential recovers or cannot resist excessive displacement heating. Even with a fast device such as a digital micromirror device (50-kHz frame) [89] or for ultracold atoms [90], a large portion of the trapped atoms is lost. The trap-loss simulation (see Methods) performed as a function of the frame rate,  $f$ , of the device and the trap frequency,  $f_r = 1/2\pi\sqrt{4U/mw_0^2}$ , supports the idea that the intensity flickering hinders the trap stability (see Figures. 3.4b and 3.4c). In particular, a constant loss exists because of the significant intensity flickering in the adiabatic region ( $f_r \gg f$ , Region ① in Figure. 3.4c). In the non-adiabatic region ( $f_r < f$ , Region ② in Figure. 3.4c), single steps do not lose atoms (because the intensity flickering is fast enough); however, in this region, either the atoms boil up fast via displacement heating or current technologies are not applicable. The holographic transport of single atoms, therefore, requires an alternative algorithmic approach (this work) to reduce the intensity flickering.

The feature of the LC-SLM most strongly coupled to the intensity flicker is the finite modulation depth  $\Phi (= 2\pi)$ . When a linear phase gradually changes from  $k_1x$  to  $k_2x$ , as depicted in Figure. 3.5a, certain regions (shaded) are flicker-free (because there are no phase jump), but the rest are not. An ideal flicker-free evolution could be achieved with infinitesimal change of  $\Delta k$ , but it would then take infinite time to transport atoms. In experiment with a finite  $\Delta k$ , we may quantify the intensity flicker

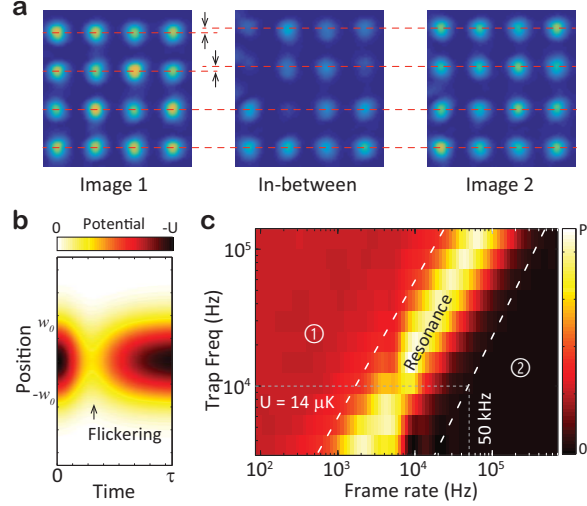


Figure 3.4: **Intensity flicker of IFTA transport.** **a**, Stroboscopic measurement of optical images of the trap array. Two different images are generated using an IFTA and the LC-SLM. The two upper lows in the second and third frames (right) are slightly shifted up, by the gaps indicated by the arrows, from the first frame (left). **b**, The transient potential for the trap loss simulation. The trap waist is  $w_o = 1.14 \mu\text{m}$ , the transient time  $\tau = 1/f$  where  $f$  is frame rate, and the displacement  $w_o/18$ . The color scale is normalized by the peak potential,  $-U$ . **c**, Trap loss landscape by the flickering potential (b). The color scale normalized by  $P_l$  represents the loss probability at time  $\tau$  which varies by  $0.005 - 0.04$  according to the initial trap condition ( $T/U = 1/18 \sim 1/12$ ).

by comparing the shaded region (denoted by  $R$  that is the field amplitude for a tweezer, normalized to one) with the un-shaded region (denoted by  $1 - R$ ). When the phase evolves from  $k_1x$  to  $k_2x$ , the fields from shaded region and un-shaded region interfere destructively, because the un-shaded region experiences  $\Phi$  phase jump while the shaded region is stationary. In Figure. 3.5b, the arrows represent  $R$  (stationary) and  $1 - R$  (with a transient angle  $\theta$ ), respectively. Then, the peak intensity of an optical tweezer varies between 1 (the vector-sum maximum) and  $(2R - 1)^2$  (the minimum), so the difference between them, that quantifies the intensity flicker, is given by  $4R(1 - R)$ . In Figure. 3.5c, the survival probability change of the loaded atoms on the traps is shown. Between the two time-lapses for natural decays, the hologram movie was played to displace the optical tweezer, while snapshots were being taken in every 60 ms. Each measured atom decay curve shows the transport loss due to the intensity flicker induced by the  $5\text{-}\mu\text{m}$  displacement of the optical tweezer. The sudden probability drop,  $p_{\text{loss}}$ , is measured for each  $R$  value, and, from the measurement, the single-frame loss probability,  $P_l = 1 - (1 - p_{\text{loss}})^{1/n}$ , where  $n$  is the number of frames in each displacement, is obtained as in Figure. 3.5d. Note that  $1 - R$  is proportional to the displacement step,  $\Delta x$ . For example,  $R = 0.96$  and  $0.94$  correspond to  $\Delta x = 180 \text{ nm}$ , and  $270 \text{ nm}$  respectively. When the result is compared with the adiabatic intensity flickering model (see Methods), the measured atom temperature agrees well with the temperatures of the two theory lines,  $107$  and  $140 \mu\text{K}$ , respectively, in Figure. 3.5d. The agreement, therefore, supports that the dominant moving loss mechanism is the intensity flicker. Because the theory predicts that the single-frame loss can be exponentially decreased as a function of  $R$ , the high fidelity holographic transport is achievable: for example, when we consider an empirically defined movable region of  $R > 0.96$ , which is about  $180\text{nm}$  step, the fidelity after a  $5\text{-}\mu\text{m}$  transport can exceed  $\sim 0.99$ . Note that the deviation of data from the

theory line at smaller  $R$  may come from stray B-field and the vector light shift of the optical tweezer, both of which cause force on atoms while the molasses is being turned on. As  $R$  is smaller, the trapped atoms are more vulnerable to the force and thus the loss has more increasing tendency.

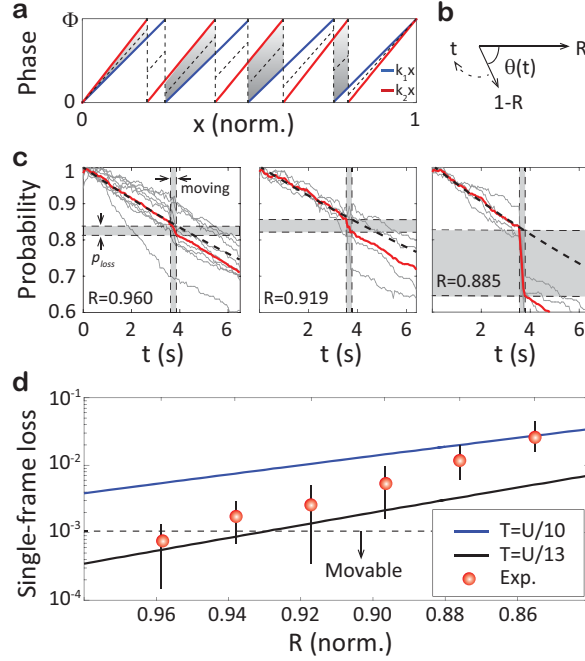


Figure 3.5: **Transport loss mechanism.** **a**, Schematic modulated two linear phases. The  $x$ -axis is normalized to 1. The sum of the shaded regions is  $R$  which is proportional to field strength. **b**, Transient vectorial representation of the flicker effect. **c**, The experimentally measured loss probabilities are shown for three different tweezer displacements  $\Delta x = 180 \mu\text{m}$ ,  $360 \mu\text{m}$ , and  $520 \mu\text{m}$ , respectively. Each data point (gray) is the average of 1,000 experimental runs, the red solid line is the average value of the data points, and the black dashed line is the loss without the displacement. The  $x$ -axis is the time-lapse after the array loading, and the  $y$ -axis is the single-atom survival probability measured using 1,000 cumulative events and normalized to 1. **d**, Single-frame losses measured for various  $R$ s. The red circles are extracted single-frame data from **c** and the error bars represent the standard deviations of the different sites. The solid lines are from the adiabatic intensity flicker model (see Methods for more details).

Our method can be further improved by increasing the number of atoms and the efficiency of initial loading. Besides simply increasing the number of dynamic holographic tweezers, one may use a passive diffractive optical element (DOE) in addition. A commonly available 6-by-6 passive DOE, for example, can capture  $N = 9$  atoms with a probability exceeding 99.8% at  $p = 0.48$ , so subsequently an active element (SLM) can pick up and move them by taking the full advantage of “all” available SLM tweezers. Also, the more stable traps, such as passive DOE or acousto-optic modulators (AOM), can be used to store them for an extended time. (Note that the AOM-based method for 2D transportation uses  $N_1 + N_2$  diffracted beams to make an array of  $N_1 \times N_2$  tweezers, so the moving degrees of freedom in that case is limited by  $N_1 + N_2$ .) Furthermore, lowering the background collision can further improve the performance: in a low-pressure ( $10^{-11}$  Torr) chamber that allows  $p_s = 0.97$ , the probability of creating a completely packed 3-by-3 atom array is expected to be as high as 80%.

In summary, the analytic approach to optical potential design has demonstrated the holographic transport of single-atom arrays. The systematic analysis of intensity flicker enabled the moving loss to

be parameterized; thus, we could find and achieve the deterministic transport regime using a holographic method. An individual atom has its own degrees of freedom in the image plane; thus, total moving degrees of freedom of  $2N$  was achieved, which demonstrates unprecedented space controllability. Furthermore, overlapping Fresnel lens pattern [94] can transport the array in the axial direction, suggesting that total  $3N$  degrees of freedom is also possible. We also formed an in situ feedback loop for atom array rearrangement, which is a proof-of-principle demonstration of high-fidelity atom array preparation. Its possible application is not limited to the deterministic array preparation but may be extended to many-body physics with arranged atoms and coherent qubit transports.

### 3.2.5 Methods

**Experiments** The active holographic device was a liquid crystal SLM (HOLOEYE, PLUTO), a reflective phase modulator array of  $1920 \times 1080$  pixels with an  $8 \mu\text{m}^2$  pixel size and the first-order diffraction efficiency was  $\sim 50\%$ . The far-off-resonant trap (FORT) beam of  $P_{\text{total}} = 1.1$  W from a Ti:sapphire continuous-wave laser (M SQUARED, SolsTiS) was tuned at  $\lambda = 820$  nm to illuminate the SLM with a beam radius of  $W = 2$  mm in a near-orthogonal incident angle. The diffracted beam from the SLM was imaged onto the intermediate image plane by an  $F_1 = 200$  mm lens, and then re-imaged onto the entrance pupil of the objective lens by a second lens (doublet,  $F_2 = 200$  mm). The objective lens (Mitutoyo, G Plan Apo) was an infinity-corrected system, having a focal length of  $F_3 = 4$  mm, a numerical aperture of  $\text{NA} = 0.5$ , and a long working distance of 16 mm with 3.5 mm-thick glass-plate compensation. Then the given laser power was able to sustain up to  $N_t = \sqrt{P_{\text{total}}\eta_d\eta_s/P_o} = 9$  optical tweezers with a trap depth of  $U = 1.4$  mK, where the diffraction efficiency was  $\eta_d = 0.5$ , the optical system loss  $\eta_s = 0.5$ , and the optical power  $P_o = 3.4$  mW.

The cold  $^{87}\text{Rb}$  atom chamber was a dilute vapor glass cell in a constant pressure of  $3 \times 10^{-10}$  Torr. It had four  $100 \times 40$  mm<sup>2</sup> clear windows with a thickness of 3.5 mm. The  $^{87}\text{Rb}$  atoms from a getter were captured by a six-arm 3D magneto-optical trap (MOT) with a beam diameter of 7.5 mm ( $1/e^2$ ), a detuning of  $-18$  MHz from the  $5S_{1/2}(F = 2) \rightarrow 5P_{3/2}(F' = 3)$  hyperfine transition, and  $dB/dz = 15$  G cm<sup>-1</sup>. After an initial MOT loading operation for 2.8 s, the atom density became  $\sim 10^{10}$  cm<sup>-3</sup> (equivalent to 0.2 atoms per single trap volume), so the  $-46$ -MHz detuned 3D molasses and the FORT were overlapped for 200 ms to achieve the collisional blockade regime of the  $p = 0.5$  filling probability in every site [68]. After this, the magnetic-field gradient and the molasses were turned off for 100 ms to dissipate residual cold atoms and then the 3-D molasses were turned back on for continuous imaging. The scattered photons were collected by the same objective lens  $F_3$  and imaged onto the CCD (Andor, iXon3 897) through the lens  $F_2$  with an overall efficiency of  $\eta_c = 0.02$ . The image plane of  $26 \times 26 \mu\text{m}^2$  was captured as a snapshot in every 60 ms. The trap lifetime was measured as 12 seconds, consistent with the effect of the background gas collision.

**Single-atom detection** The scattering cross-section is given by  $\sigma = \sigma_0/[1 + 4(\Delta/\Gamma)^2 + I/I_{\text{sat}}]$ , where the resonant cross-section is  $\sigma_0 = 2.907 \times 10^{-9}$  cm<sup>2</sup>, the natural line width  $\Gamma = 5.746$  MHz, the saturation intensity  $I_{\text{sat}} = 1.669$  mW cm<sup>-2</sup>, the detuning  $\Delta = -100$  MHz (Stark shift is considered), and the intensity  $I = 27$  mW cm<sup>-2</sup>. Each atom in an optical tweezer emits  $2.87 \times 10^5$  photons per second. With the overall detection efficiency of 0.02 and the exposure time of 50 ms, we collect 280 photons per atom. It corresponds to a signal-to-noise ratio (SNR)  $> 5$  for the CCD. When a Gaussian noise is assumed, the theoretical discrimination probability between zero and single atom is given with  $5\sigma$  significance or 99.99995%. In the experiments, a background photon noise exists, but the histogram shows the success probability exceeding 99.99%.

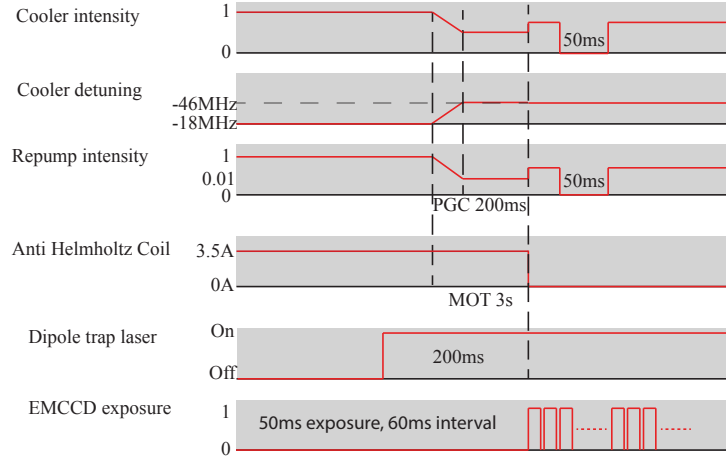


Figure 3.6: The experimental sequence table.

The figure 3.6 summarizes the experimental sequence described above.

**Heating in optical tweezers** There are several heating sources for trapped atoms including the FORT scattering, the intensity noise, the beam pointing fluctuation; however, none of them are a significant heating source. The heating caused by the photon scattering from FORT is estimated as  $7 \mu\text{K s}^{-1}$  at the peak intensity, which is negligible in our trap. The intensity fluctuation ( $\Delta I$ ) and beam pointing fluctuation ( $\Delta\omega_o$ ) by the LC-SLM voltage update are up to 6% and 5%, respectively; its noise spectrum, however, is less than 500 Hz. The parametric heating has harmonic resonances at  $\omega_r/2n$  [91, 92], which are far from 500 Hz. The quantitative heating rate has not been estimated; however, any atom loss difference is not observed during the one second transport without the molasses. Empirically the low frequency noise does not degrade the trap capability in our 1.4 mK deep trap. Utilizing an intensity feedback control to the diffraction beam will diminish the intensity fluctuation [93]; thus, a lower trap depth would be achievable.

**Dynamic range and resolution of the control space** The optical tweezers are separated from the zeroth order diffraction by  $X_{01} = F_1 F_3 / F_2 \times k_1 / k > 5 \mu\text{m}$  to avoid the cross-talk, which sets the lower limit  $X_{01}^{\min} = 5 \mu\text{m}$  of the dynamic range of the control space. The upper limit is empirically given by  $X_{01}^{\max} = 45 \mu\text{m}$ , because the diffraction efficiency decreases as  $k_1$  increases. Note that the entrance pupil diameter of the objective lens is  $D \sim 2NA F_3$  and the initial beam diameter  $2W = 4 \text{ mm}$  at the SLM is (de)magnified by the ratio  $F_2 / F_1 = 1$  to fit with  $D$  for optimal performance, which results in  $X_{01} = D / 2NA \times k_1 / k$ , independent of the focal lengths of the system. In our experiment, a safe working area of  $26 \times 26 \mu\text{m}^2$  is used for the optical tweezer patterns and the imaging plane. The discrete phase induces a beam steering error [95] but the amount of the error is only 4 nm in our system with 256 gray levels. Thus the resolution is limited by 4 nm, which is much smaller than the long term drift (100 nm) and the LC-SLM refresh fluctuation (100 nm).

**Adiabatic intensity flicker model** The probability for an atom initially trapped in a potential  $U$  to escape from an adiabatically lowered potential  $U'$  is approximately given by

$$P_l = \int_{U'}^{\infty} \frac{E^2}{2(k_B T')^3} e^{-\frac{E}{k_B T'}} dE, \quad (3.3)$$

where  $T' = T \sqrt{U'/U}$  is the temperature of the Boltzman distribution [58]. In our experiment, the lowest trap potential is given by  $U' = (2R - 1)^2 U$ . The solid lines in Figure. 3.5d are the numerically obtained results of Eq. (3.3) for  $T = U/13$  and  $T = U/10$ , respectively.

**Intensity flicker estimation** The finite modulation depth ( $0 \leq \phi \leq \Phi$ ) of the SLM phase restricts the ideal linear phase to a modulated phase in a sawtooth shape. We consider two SLM phases  $\phi_1(x) = \text{mod}(k_1x + \Phi/2, \Phi)$  and  $\phi_2(x) = \text{mod}(k_2x + \Phi/2, \Phi)$ , where  $\Phi \in 2\pi N$ ,  $x \in [-D/2, D/2]$ ,  $D = 4.6$  mm is the size of the active SLM window, and we assume  $k_1 \leq k_2$  without loss of generality. The phase evolution from  $\phi_1(x)$  to  $\phi_2(x)$  is then given by  $\phi(x, t) = \phi_1(x)e^{-t/\tau} + \phi_2(x)(1 - e^{-t/\tau}) = k_1xe^{-t/\tau} + k_2x(1 - e^{-t/\tau}) - \Phi N_1(x)e^{-t/\tau} - \Phi N_2(x)(1 - e^{-t/\tau})$ , where  $N_{1,2}(x) = [k_{1,2}x/\Phi]$  is a function defined with the Gauss' symbol  $[x] = x - \text{mod}(x)$  and  $\tau$  denotes the response time. The condition  $N_1(x) = N_2(x)$  defines the flicker-free evolution regions (the shaded regions in Figure. 3.5a). In our experiment, the flicker-free regions are divided into two regions respectively satisfying  $N_1(x) = N_2(x)$  and  $N_1(x) = N_2(x) - 1$ , because  $R$  is large enough for an atom transport or  $(k_2 - k_1)(D/2) < 2\Phi$ . As a result,  $R$  defined by the sum of the flicker-free regions divided by  $D/2$  is given by

$$\begin{aligned} R &= \frac{2\Phi}{D} \sum_{n=1}^{N_2^f} \left\{ \frac{n}{k_2} - \frac{(n-1)}{k_1} \right\} + 1 - \frac{2\Phi}{k_1 D} N_2^f \\ &= \frac{\Phi}{k_2 D} N_2^f (N_2^f + 1) - \frac{\Phi}{k_1 D} N_2^f (N_2^f + 1) + 1 \end{aligned} \quad (3.4)$$

for the case of  $N_1(D/2) = N_2(D/2) \equiv N_2^f$  and

$$\begin{aligned} R &= \frac{2\Phi}{D} \sum_{n=1}^{N_2^f} \left\{ \frac{n}{k_2} - \frac{(n-1)}{k_1} \right\} \\ &= \frac{\Phi}{k_2 D} N_2^f (N_2^f + 1) - \frac{\Phi}{k_1 D} N_2^f (N_2^f - 1) \end{aligned} \quad (3.5)$$

for the case of  $N_1(D/2) \neq N_2(D/2)$ . The  $R$  in Eq. (3.4) can be further simplified to

$$R = 1 - \frac{k_2 D + 2\Phi}{4\Phi} \left( 1 - \frac{k_1}{k_2} \right) \quad (3.6)$$

under the assumption  $N_1 = N_2 \approx k_2 D/2/\Phi$ . The obtained analytic result for the  $R$  is within 2% difference from the actual numerical value estimated by considering the circular active SLM window, the Gaussian beam profile of the optical tweezers, the 2D nature of the  $k_1$  and  $k_2$ , and the discrete pixel size of the SLM. Within the experimental variation of  $k_1$  and  $k_2$ ,  $R$  varies from 0.86 to 0.96 as shown in Figure. 3.5d.

**Single-frame displacement limit** The maximum single-frame displacement  $\Delta X_{01} = \frac{D}{2k\text{NA}} \Delta k$  is also given as a function of  $R$ . When Eq. (3.6) is expressed with  $k_2 D = 2k\text{NA} X_{01}$  and  $1 - k_1/k_2 = \Delta X_{01}/X_{01}$ , we obtain

$$\frac{\Delta X_{01}}{X_{01}} \leq \frac{2(1-R)\Phi}{2\text{NA}kX_{01} + \Phi}, \quad (3.7)$$

so the single-frame displacement is proportional to  $1 - R$ .

**The trap loss simulation in Figures. 3.4b and 3.4c** For a pair of initial and final trap potentials, which have  $N$  trap sites, two phase holograms are calculated using Gerschberg-Saxton algorithm, respectively. Some of the sites in the initial trap potential are separated by  $1/18w_o$  from the final trap potential. The in-between holograms are constructed by  $\phi_1 e^{-t/\tau} + \phi_2(1 - e^{-t/\tau})$ , which generate the transient behavior of a single trap potential as shown in Figure. 3.4b. Then, the trajectories  $(p, q)$  of the 1D classical Hamiltonian equation of motion calculated by the symplectic Euler method are used to estimate the trap loss probability in Figure. 3.4c, where we use a loss criteria of  $|q(t)| > 2.5w_o$  and the initial energy and positions are sampled using the Monte-Carlo method.

**Random mask algorithm analysis**

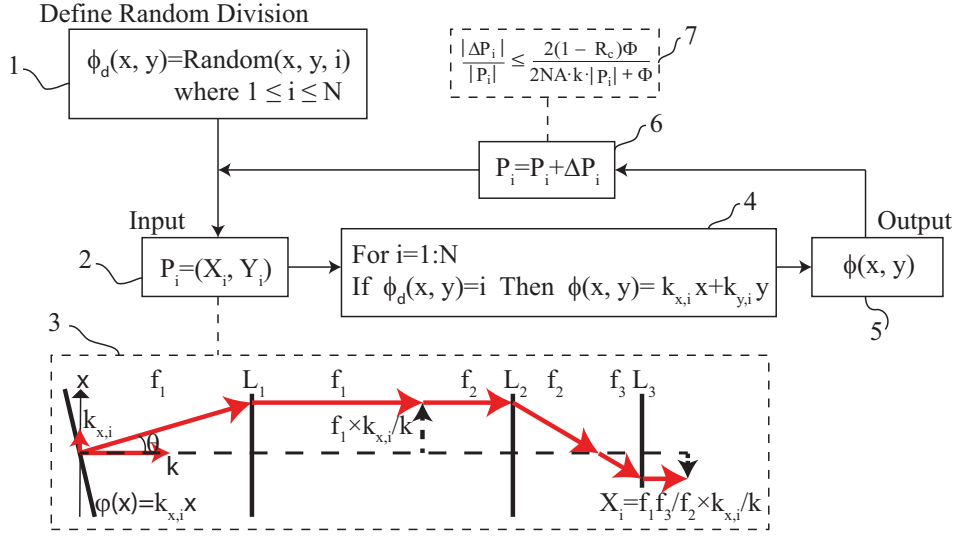


Figure 3.7: Random mask algorithm scheme.

The linear phase is an analytic solution of beam steering [95]. The linear phase is the flicker-free evolution of phase that is essential for single atom transport [3]. Its implementation is relying on the liquid crystal spatial light modulator (LCSLM) that has gray scale (256-level) discrete phase step. The 256 gray scale is sufficient to be regarded as continuous phase in that the minimum resolution of beam steering is [3]. The below enumerated descriptions correspond to Figure 3.7.

1. The phase modulation plane of the LCSLM is defined by  $(x,y)$ . Then the each  $(x,y)$  is temporally assigned by random integer  $i$ . This step is defined by random division.
2. The position of the  $i$ -th tweezer on the target image is defined by  $P_i$ .
3. The linear phase  $\phi(x)$  and the position  $P_i$  has one-to-one correspondence. The relation is given by  $X_i = f_1 f_3 / f_2 \times k_{x,i} / k$  where the laser beam wave-number  $k$ , the focal length of the lens  $f_{1,2,3}$  of the imaging system.
4. Assign the phase  $\phi_d$ .
5. The resulting phase plane  $\phi(x,y)$  generates tweezers on the target image that are positioned at  $P_i$ .
6. After that, the position  $P_i$  are displaced by  $\Delta P_i$ .
7. The restriction on the displacement is defined for reliable single atom transport.

Iterative operation of LCSLM from 2-6 generates hologram movies that the tweezers are individually displaced according to the position.

### 3.3 Scale Improvement; superposition algorithm

The random mask algorithm has a major defect for scaling up the system size, which is  $N^2$  requirement of laser power due to decreasing diffraction efficiency as the division increases. An immediate remedy is by using superposition algorithm, which is just superposing the multiple linear phases,  $\exp\{i\Phi\} = \sum_j \exp\{ik_j x\}$ . It provides  $N$  scaling of required power, yet compromise the versatility of geometric position. The superposed sites interfere each others and it introduces detrimental effect when the sites are periodically situated.

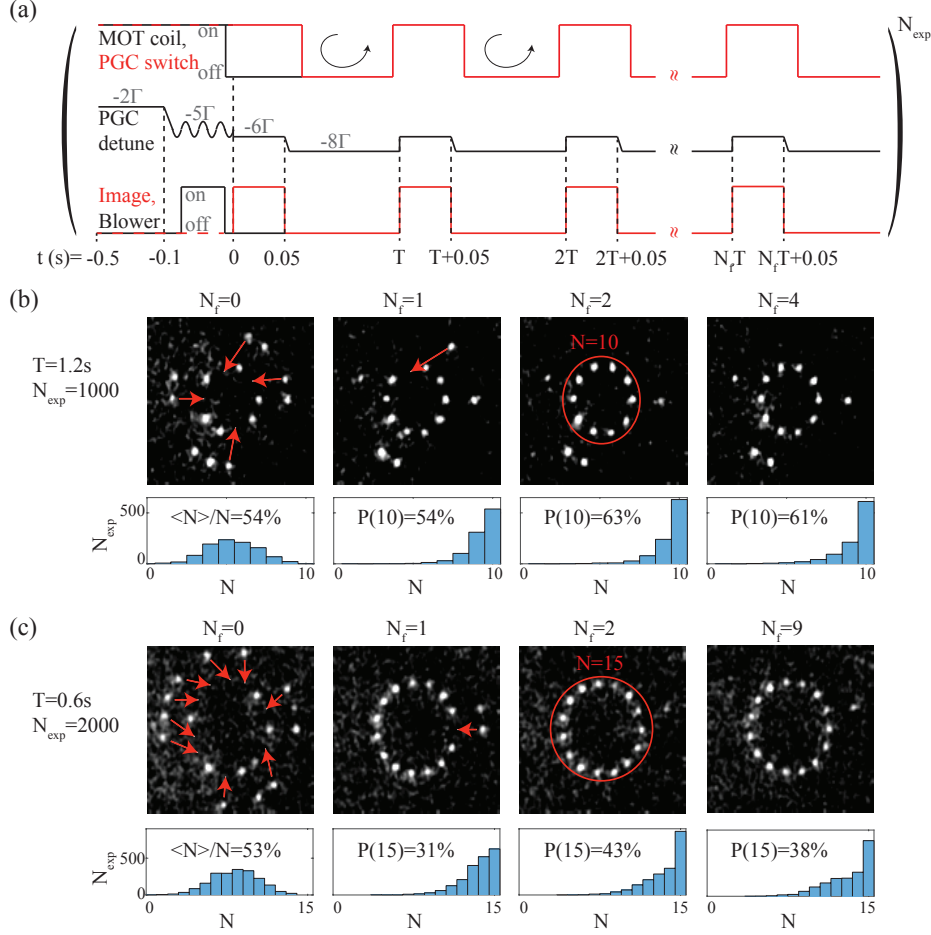


Figure 3.8: (a) Time sequence of the generic experiments. At first, 3D MOT was loaded and soon after detuning of the MOT beam was decreased for PGC stage. The 1 kHz sinusoidal modulation of the detuning was for optimization of single-atom loading rate on the various traps having different depths. Then the MOT coil (anti-Helmholtz) was turned off and the PGC detune was fixed for single-atom fluorescence imaging. After capturing the image, the detune was further decreased and PGC beam was turned off for time  $T=0.5$  s that is feed-back operation period. The imaging and feed-back sequence periodically repeated for pre-defined number  $N_f$ . Then the entire sequence runs for  $N_{exp}$ .  $\Gamma$  denotes spontaneous decay rate of  $5P_{3/2}$  ( $2\pi \times 6$  MHz). (b)  $N=10$  circular array deterministic generation. (c)  $N=15$  circular array deterministic generation.

Thus, superposition algorithm is suitable for aperiodic structures such as multiple rings. The deterministic preparation of ring array is demonstrated in Figure 3.8.

## 3.4 Versatility Improvement: a modified Gerchberg-Saxton algorithm

Holographic optical tweezer, the optical device that utilizes dynamic holograms to produce a real-space optical field movie, is a powerful tool to generate a large number of optical focal points with arbitrary geometries and also capable of dynamically reconfiguring their geometry in unmatched parallelism. This device has drawn much attention from the field of optical manipulation [96, 97], and is applied on a broad range of research topics including exotic photonic structure assembly [98], position tracking [99], nanoscopy [100], and single-atom trapping [101, 102]. Especially, the holographic single-atom trapping has drawn many attention recently in that highly tunable quantum systems for many-body quantum physics and quantum information science are achievable by single-beam scheme [103, 44]. In that regards, formation of large number of optical tweezers that are completely filled with single atoms per site has been an important issue.

A latest demonstration on single-atom sorting methods [43, 104, 105] has resolved this issue and progress the field of research; Single-atom tweezer quantum systems by holographic optical manipulations [106, 107, 108]. Among the methods, dynamic holographic optical tweezer (DHOT) which is our previous work [43] has known to be a promising technique for such particle trapping and sorting due to its multi-dimensional tunability and parallelism [97, 43, 109]. However, it is still demanded to develop more efficient algorithms due to the major two issues; Our previous proof-of-principle demonstrations [43, 42] had limited power efficiency and relied on a look-up table search for atom sorting.

In this section, I describe how those issues have overcome; the power efficiency is significantly increased from  $1/N^2$  to  $1/N$  by optimizing a hologram generation method based on Gerchberg-Saxton algorithm, and the look-up table search for atom sorting is replaced by Hungarian algorithm [110]. The method utilizes the versatility and parallelism of the active spatial light modulator (SLM) as well as enables real-time operation for elusive single-atom trap in arbitrary 2D shape. At first, the experimental setup and experimental procedure for the implementation is described. After that, the details of the hologram algorithm is explained. Lastly, I show the results; defect-free single-atom array, and discuss its scalability of atom numbers and 3-dimensional performance.

### 3.4.1 Upgrade of spatial light modulator

Beforehand, I compared two SLM performances such as stability and efficiency in Figure 3.9. The upgraded SLM shows superior performance for both efficiency and stability.

### 3.4.2 Experimental setup and procedure

Our single-atom tweezer trap setup consists of a Fourier-domain hologram device and  $^{87}\text{Rb}$  magneto-optical trap (MOT), similar to our earlier reports [43, 42, 110]. Phase holograms were generated by using a phase-only SLM (Meadowlark, XY series) which had  $512 \times 512$  pixels of each  $16 \times 16 \mu\text{m}^2$  size, high diffraction efficiency 85%, and fast refresh rate exceeding 2 kHz for minimizing phase errors and intensity fluctuations. A 820-nm laser beam (M-squared, SolsTis,  $\text{TEM}_{00}$  and linear polarization) was expanded

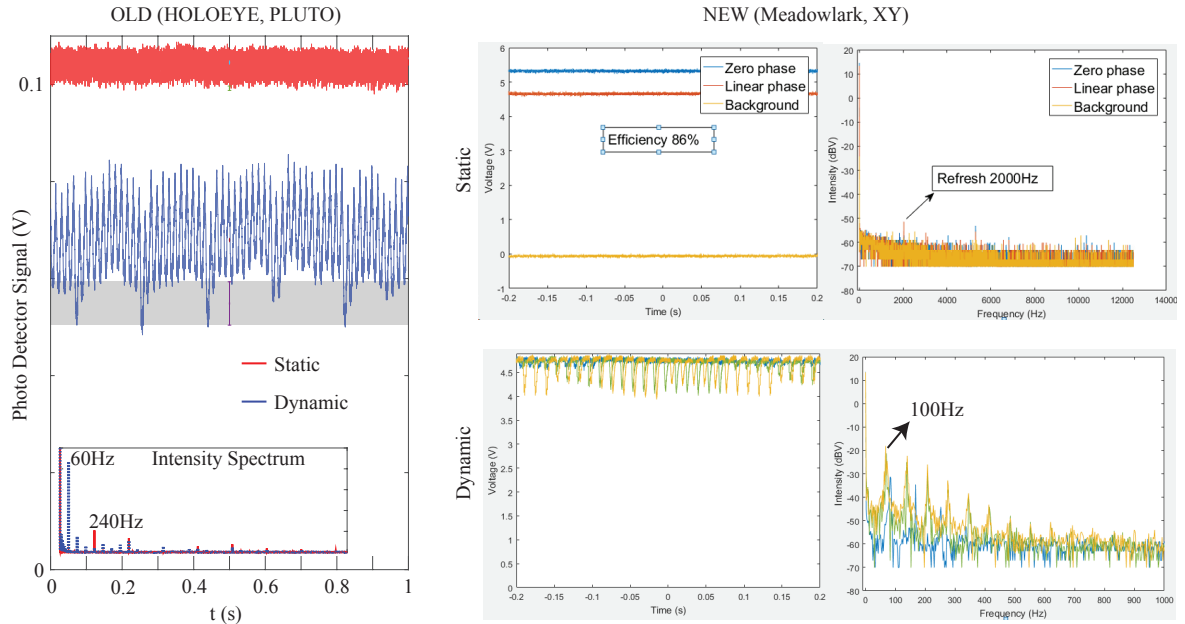


Figure 3.9: Two SLM performance comparison. Old one had used before this session of my thesis. New one have used after this session of my thesis. (OLD) the diffracted beam was measured by using photo-diode for both static and dynamic traps. The diffraction efficiency is about 50 % (not shown). The intensity spectrum was shown in linear scale as well. The old device has low (240 Hz) refresh rate, thus the phase fluctuation directly coupled to the intensity noise showing strong spectrum noise peak even in the linear scale. For the dynamic traps, the situation becomes worse showing stronger intensity fluctuation. (NEW) Both the diffracted beam and zero order beam was measured as well as background noise. In the frequency domain, any significant noise peaks have observed. Note that the spectrum is log scale. For the dynamic traps, the saw-tooth intensity traces have observed as expected from the ideal theory of liquid crystal hydro-dynamics. In the spectrum (log scale), harmonics of frame rate have observed.

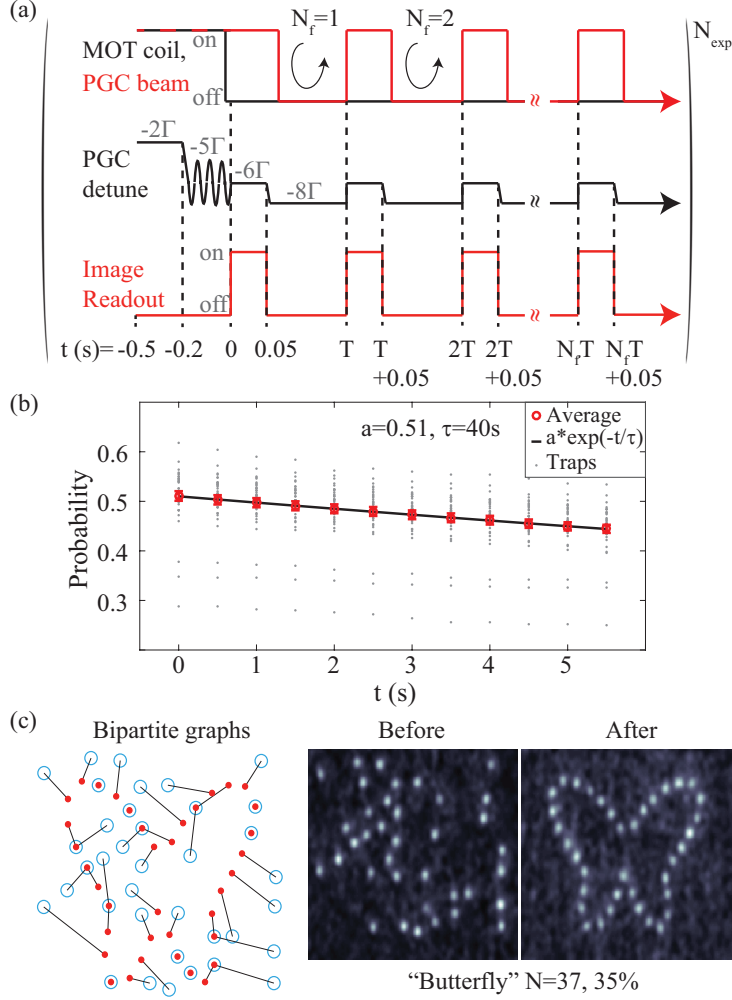


Figure 3.10: (a) Time sequence of the generic experiments described in Figure 3.8 is used again. (b) Lifetime of static (without feed-back operation) single-atom traps. Grey dots are results from individual traps. Red dots are average of the traps. Black line is exponential fit resulting in initial loading rate of 0.51 and lifetime of 40 s. During continuous feed-back operation, lifetime reduced to 20 s. (c) An example of feed-back operation. The 96 total traps including targets were initially loaded. The bipartite graphs connect between single-atom and target site. The blue circles and red dots are single-atom and target sites, respectively. The single-atom transport paths are straight lines corresponding to the links of graphs. The single-shot fluorescence images before and after the feed-back operation represent the result of the graphs. The "Butterfly" is composed of 37 single-atom, having 35% peak filling rate at  $N_f=3$  for  $N_{exp}=500$ .

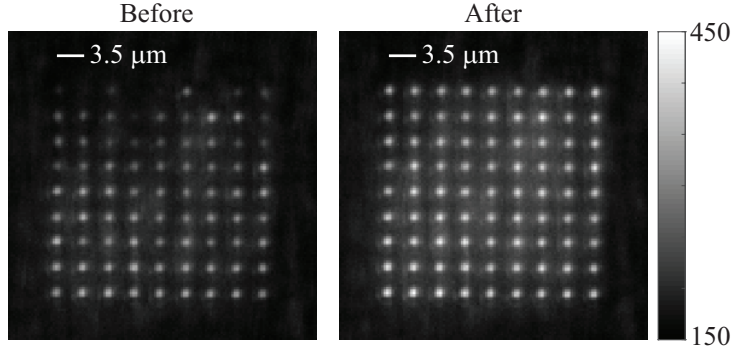


Figure 3.11: Average of hundreds of single-atom fluorescence images before and after the aberration compensation (see text). Each images are resulting from the different hologram. Both have the same color scale and dimension.

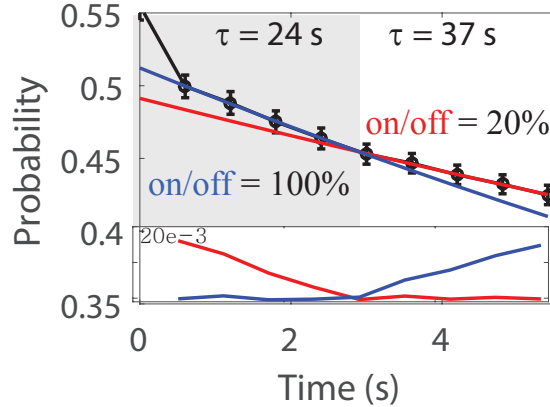


Figure 3.12: Lifetime improvement by applying on/off cycle of PGC beam. The duty cycle 20 % is applied. (Inset) the residue of the exponential fit.

and collimated to 8 mm for covering the entire SLM area, before the beam was near-normal ( $80^\circ$ ) reflected from the SLM surface. Then the phase modulated beam was transferred onto the entrance pupil of the 0.5 NA objective lens (Mitutoyo, G-Plan apo  $50\times$ ) by the telescope ( $F_1=400$  mm,  $F_2=200$  mm). Finally, the objective lens transfers the hologram to the single-atom dipole traps of around 1 mK depth and  $1 \mu\text{m}$  waist inside the vacuum chamber to spatially overlap with  $^{87}\text{Rb}$  MOT. Then, each traps are partially ( $\sim 0.5$ ) filled with  $^{87}\text{Rb}$  single atoms. The partially loaded trap array is analysed to fill out the pre-defined targets by simultaneous atom shuttling as shown in Fig. 3.10(c).

Fig. 3.10 (c) shows an example of successful feedback operation for preparing a single-atom array, "Butterfly", composed of 37 targets and 59 redundant sites randomly scattered around the targets. Note that the fluorescence images are 2D Gaussian filtered for clear view. We utilize Hungarian algorithm to design efficient and complete matchings between the redundancies and the targets [110]. The algorithm has the computational complexity  $\sim O(n^3)$  and generates bipartite graphs between the loaded sites and the target sites by minimizing a constraint. The constraint was the sum of length square of the links in the graphs. The links of the graphs, straight lines, were directly used as transport paths. As a result, the paths automatically avoid collisions between each others during simultaneous shuttling [110]. Finding the complete matching from total 100 sites to any targets took only 10 ms by using a personal computer

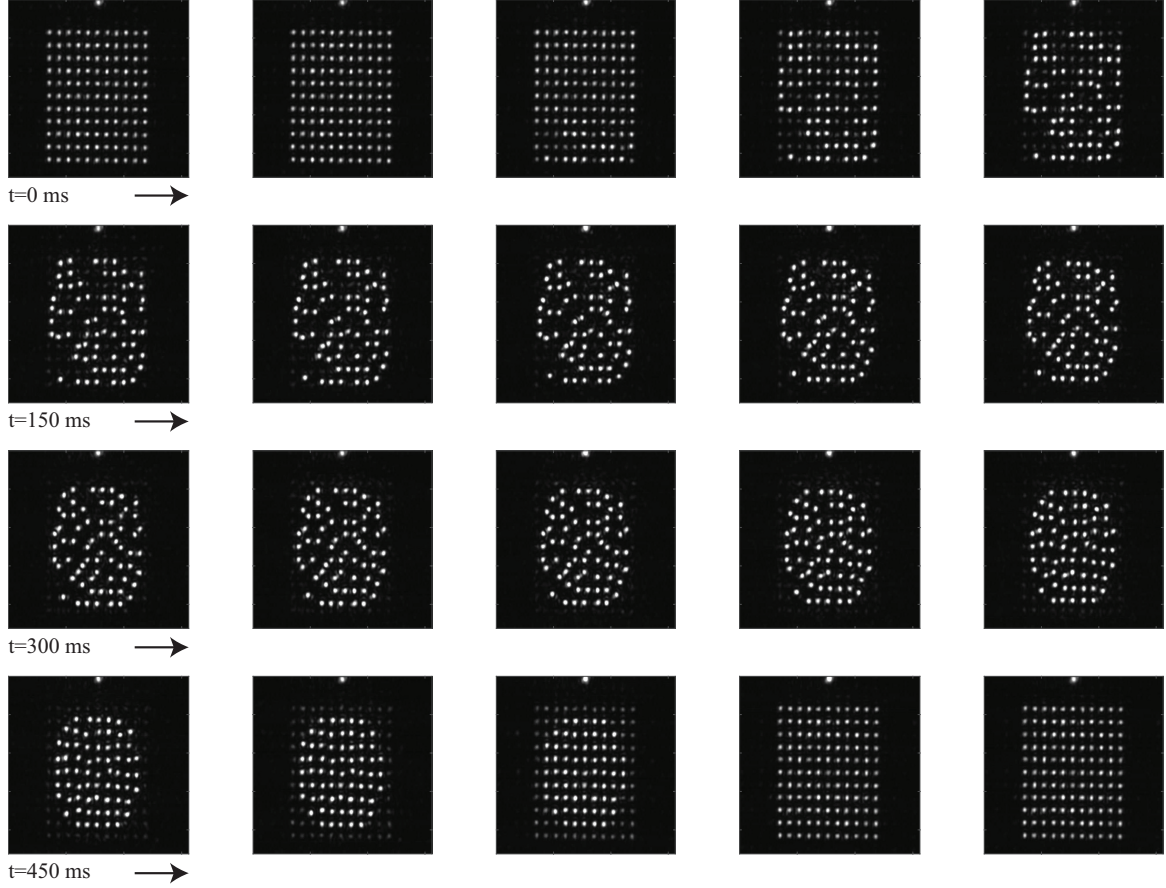


Figure 3.13: An example of feedback operation. They are measured optical images from the intermediate plane when a computer-simulated atom loading information is given. The purpose is to gather the atoms in the square lattice to its center for defect-free array formation.

(Intel CPU, i7-6700K).

In Fig. 3.10(a), the detailed experimental sequence for the generic feedback operation is shown. At first, 3D MOT was loaded by 780 nm laser. Then, detuning of the MOT beam was decreased for polarization gradient cooling (PGC). The 1 kHz sinusoidal modulation of the detuning was applied for optimization of single-atom loading rate on the array of different trap depths. The atom temperature was  $80 \mu\text{K}$ . The fine-tuned PGC enabled us to achieve efficient initial loading condition,  $\sim 0.5$ . Then the MOT coil was turned off and the PGC detune was fixed for single-atom fluorescence imaging. After capturing the image, the detune was further decreased and PGC beam was turned off for time  $T = 0.5 \text{ s}$ , where  $T$  is feedback operation period. The imaging and feedback periodically repeated for pre-defined number  $N_f$ . Then the entire sequence runs for  $N_{exp}$ .

Before turn off the MOT coil, 780 nm resonant beam was used for blowing away the itinerant cold atoms to maximize the trap lifetime. As a result in Fig. 3.10(b), the lifetime of static traps are measured as 40 s which is almost limited by background vapor pressure  $3 \times 10^{-10} \text{ Torr}$ . We found that turning off the PGC beams during the feedback period  $T$  reduces the shuttling loss.

The aberration from the SLM and transfer optics were compensated by using the methods described in Refs. [111, 112]. Those methods require direct measurements of the hologram images. Although it was not possible to directly measure the trap intensity inside the vacuum chamber due to the chamber size, instead, the traps in the intermediate image plane were measured and used for the aberration

compensation. The resulting quality of the traps in terms of the min-max intensity over its average was 85%-115%. This was enough for achieving successful single-shot fluorescence measurement fidelity above 99.9% within 40 ms camera exposure. The aberration corrections are essential for achieving the large field-of-view (FOV) of the image plane. As shown in Fig 3.11, the comparison images before and after the compensation clearly exhibit the extended FOV with more homogeneous atom fluorescence. The corrections are also important for reducing shot-to-shot hologram image fluctuation.

Note that Figure 3.12 shows the improved trap life-time when the PGC beams are periodically switched on and off. This observation means that the trap life-time can be longer when the PGC beams are off. This is my empirical finding to optimize the lifetime, not showing fundamental improvements for optical trapping. If the PGC beam could cool down the atoms below 30  $\mu\text{K}$ , 100 % duty cycle may show better performance.

For more intuitive understanding of the system, the details of 11 by 11 square array during the feedback operation period  $T$  are shown in Fig. 3.13. They are optical images measured at the intermediate image plane. At first, the computer-simulated single-atom loading configuration and its graphs for atom shuttling are generated. Then, the hologram movies are calculated and runs. The empty sites are removed during the atom shuttling to avoid collisions between the others. After almost finishing the shuttling, the removed traps are recovered and the original array shape is maintained for indefinite operations.

## 3.5 Weighted, induction, and zero-pedding Gerchberg-Saxton algorithm

We developed a power efficient (scales in  $N$ ) hologram generation algorithm based on Gerchberg-Saxton (GS) algorithm that could maintain trapped single-atom while shuttling them via hologram change. Also, we achieved fast calculation speed ( $>60$  Hz) by using graphic process units (GPU, NVidia, GTX Titan-X Pascal) and open source library (CUDA and ArrayFire). In particular, the GPU-accelerated calculation was highly parallel, enough to maintain the frame-per-second (fps) even up to several thousands of trap sites (computational scalability). In comparison, our previous prototype synthesizer was limited by the power efficiency (required power scales in  $N^2$ ) and also the calculation speed ( $<10$  Hz) [43, 42]. Here, we call it wiz-GS algorithm.

### 3.5.1 Review

In our context, GS algorithm is an iterative 2D-Fourier transform algorithm that calculates the phase  $\Phi(X, Y)$  in the Fourier domain to produce the optical field  $T(x, y)$  in the image plane.  $T(x, y)$  is real number, normalized to 1. There are coordinates  $(x_\alpha, y_\alpha)$  which represent trap positions satisfying  $T(x_\alpha, y_\alpha) = 1$  and 0 elsewhere. We exclude  $(x = 0, y = 0)$  to remove the unwanted zero-th order beam. The flow of algorithm is as follows: the amplitude  $\mathcal{A}(X, Y)$  in the Fourier domain is given by a constant (Gaussian) in our case, and the initial phase  $\Phi_0(X, Y)$  is usually chosen arbitrary. The complex field  $\mathcal{A} \exp(i\Phi_0)$  is Fourier-transformed to give a result in the image plane. Then, the amplitude of the result  $A(x, y)$  is substituted by  $T(x, y)$ , and inverse-Fourier transformed. Again in the Fourier domain, the amplitude is substituted by  $\mathcal{A}(X, Y)$ , and the new complex field  $\mathcal{A} \exp(i\Phi_1)$  is acquired by finishing single iteration. These processes are iterated up to the  $i$ -th time and the resulting  $\Phi_i(X, Y)$  is used as the phase mask  $\Phi(X, Y)$ . Then, the result becomes  $T(x, y) \approx |\mathbb{FT}[\mathcal{A} \exp(i\Phi)]|$ .

Such GS algorithm for generating single-atom tweezer traps has proven its versatilities [101], yet

been known that it is impossible to transport single-atom trapped in. Because the SLM based transport uses a movie via frame update, rather than continuous sweep of trap, it has been believed that the frame-transit intensity fluctuation (or intensity flicker) of the traps are too huge to retain the trapped atoms [113]. If the frame rate surpasses the trap frequency, the intensity flicker could be ignored as like the case of macroscopic particles or ultra-cold atoms [109, 114]. However, the single-atom trap frequencies usually reach an order of 100 kHz. Therefore, reducing the fluctuation is the viable way for achieving the transport of trapped atoms.

### 3.5.2 Issues to be addressed

The problem is defined in a more formal way as follows: Suppose that the traps at the  $k$ -th frame are given by  $E^{(k)}(x, y) = \mathbb{FT}[\mathcal{A} \exp(i\Phi^{(k)})]$ . Note that  $|E^{(k)}(x, y)| \approx T^{(k)}(x, y)$ . Define  $E(t)$  and  $\Phi(t)$  as frame-transit functions such that  $E^{(k,k+1)} = E(t_{0,1})$  and  $\Phi^{(k,k+1)} = \Phi(t_{0,1})$  for all spatial coordinates where  $t \in [t_0, t_1]$  without loss of generality. Then the traps are re-written by

$$E(t) = \mathbb{FT}[\mathcal{A} \exp(i\Phi(t_0)) \exp\{i(\Phi(t_1) - \Phi(t_0))w(t)\}], \quad (3.8)$$

where the hologram transient is  $\Phi(t) = \Phi(t_0) + (\Phi(t_1) - \Phi(t_0))w(t)$  with  $w(t)$  a global transient function satisfying  $w(t_0) = 0$ ,  $w(t_1) = 1$ , and monotone. The phase evolution is always continuous and bound to a certain value, e.g.  $\Phi \in [0, 2\pi]$ . So, the problem becomes how to maintain  $E(t) - E(t_{0,1}) \ll 1$  for the set of  $(x_\alpha^{(k,k+1)}, y_\alpha^{(k,k+1)})$ : Two conditions which are  $|\Phi(t_1) - \Phi(t_0)| \ll 1$  for preserving diffraction efficiency (the first condition) and  $|(x_\alpha^{(k+1)}, y_\alpha^{(k+1)}) - (x_\alpha^{(k)}, y_\alpha^{(k)})| \ll w_0$  for continuity (the second condition) are respectively required to maintain the frame-transit intensity. If the first condition,  $|\Phi(t_1) - \Phi(t_0)| \ll 1$ , holds for all  $X, Y$ , then  $E(t)$  is approximated to

$$E(t) = E(t_0) + \{E(t_1) - E(t_0)\}w(t), \quad (3.9)$$

and the sum over Eq. 3.9 for all  $(x, y)$  shows energy conservation for all  $t$  because  $\sum_{x,y} E(t_1) = \sum_{x,y} E(t_0)$ . In a more intuitive way, the first condition prevents energy leakage to other diffraction orders thus preserves the overall intensity of the traps during frame-transit. Although this condition does not guarantee energy conservation of individual traps, this is strongly supported by both simulation and experimental results. The second condition can be easily understood by considering two Gaussians  $\exp(-2x^2/w_0^2)$ , and  $\exp(-2(x - \delta)^2/w_0^2)$  corresponding to  $T(x_\alpha^{(k,k+1)}, y_\alpha^{(k,k+1)})$ , respectively. As the frame evolves in time, the Gaussian deforms by conserving the overall intensity according to the first condition. So, if the second condition holds, the transient minimum of the intensity is then given by  $\exp(-\delta^2/2w_0^2)$ . Thus, the frame-transit fluctuation is arbitrarily lowered by reducing the displacement between consecutive frames.

So far, only mathematical conditions for retaining and shuttling single-atom via dynamic phase holograms have discussed. We describe our modified GS algorithm satisfying the conditions thus minimizing the transient fluctuation as shown in Fig. 3.14. The modification combines three indispensable utilities which are called weighted, induction, and zero-padding, respectively. We dubbed it as wiz-GS algorithm. In addition to them, phase reduction could more improve the performance. All those individual modifications have been introduced in the ref. [101, 115, 116, 117]. So, we focus on describing more technical parts in details.

### 3.5.3 Weighted-GS

The weighted function modifies the target  $T(x, y) \rightarrow T_i(x, y)$  at every iteration according to the calculation or direct measurement of  $A(x, y)$ . The modification is as follows,

$$T_i(x_\alpha, y_\alpha) = \frac{T_{i-1}(x_\alpha, y_\alpha) \langle A(x_\alpha, y_\alpha) \rangle_\alpha}{\langle T_{i-1}(x_\alpha, y_\alpha) \rangle_\alpha A(x_\alpha, y_\alpha)}, \quad (3.10)$$

where the initial condition  $T_0$  equals to  $T$ . The meaning is that the discrepancies between  $A$  and  $T$  is actively over-shoot. Note that  $T_i$  should be normalized as well, otherwise detrimental in long-run. Performance-wise, using directly measured  $A$  for each iteration is much better, however, we can use calculated  $A$  only because realization of imperfect trap images would induce atom loss. The main benefits of weighted function are increased resemblance of the final result to the target and faster convergence.

### 3.5.4 Induction-GS

The induction function refers the phase of the previous frame  $\Phi^{(k-1)}$  to the initial phase of the next frame  $\Phi_0^{(k)}$ . The similarity between the successive phases ( $|\Phi^{(k)} - \Phi^{(k-1)}| \ll 1$ ) is empirically guaranteed by the induction. Also, the required number of iteration is reduced.

### 3.5.5 Zero-padding-GS

The zero-padding function extends the range of the coordinates in Fourier domain  $(X, Y)$  to  $(N_z X, N_z Y)$ . As a result, the resolution in image plane is multiplied by  $N_z$ . This is important to satisfy the second condition. For example, initial Fourier domain is  $512 \times 512$  pixel of SLM and incident beam covers the entire domain. If we use only the initial domain size, the accessible resolution in image plane is limited by beam waist  $w_0$ . Instead, we extend Fourier domain by adding fictitious zero phases surrounding the original domain, and conduct iteration of the algorithm. The resolution limit becomes better by the factor  $1/N_z$ . The drawback is increased complexity of  $N_z \log(N_z)$  for Fourier transform. However, current high-end GPU can perform 2D-FFT in parallel thus array size of up to  $2048 \times 2048$  could be handled without attenuation on fps in our case.

### 3.5.6 Phase reduction

The additional function, phase reduction, utilizes the range of phase  $\Phi \in [0, 4\pi]$  instead of  $[0, 2\pi]$ . This further reduces phase difference between successive frames  $|\Phi^{(k)} - \Phi^{(k-1)}|$ . The process occurs after finishing a phase calculation, post-process of the algorithm. For the precess, the calculated phase range is constrained to  $\Phi^{(k)} \in [\pi, 3\pi]$ . Then the process is as follows. First, if the cases

$$\Phi^{(k)} - \Phi^{(k-1)} > \pi \quad \& \quad \Phi^{(k)} > 2\pi \quad (3.11)$$

are both satisfied, then operates  $\Phi^{(k)} = \Phi^{(k)} - 2\pi$  pixel-wise. Second, if the similar conditions hold,

$$\Phi^{(k)} - \Phi^{(k-1)} < -\pi \quad \& \quad \Phi^{(k)} < 2\pi \quad (3.12)$$

operates  $\Phi^{(k)} = \Phi^{(k)} + 2\pi$  pixel-wise as well. It means that the phase reduction is (un)wrapping the phase to minimize physical phase rotation.

By combining all the functions in the algorithm, the transit-fluctuation is minimized up to theoretical limit as shown in Fig. 3.14.

The spatial coordinates in both  $(X, Y)$  and  $(x, y)$  are discrete in physical realization. The trap position  $(x_\alpha, y_\alpha)$  only occupies one pixel in the computation.

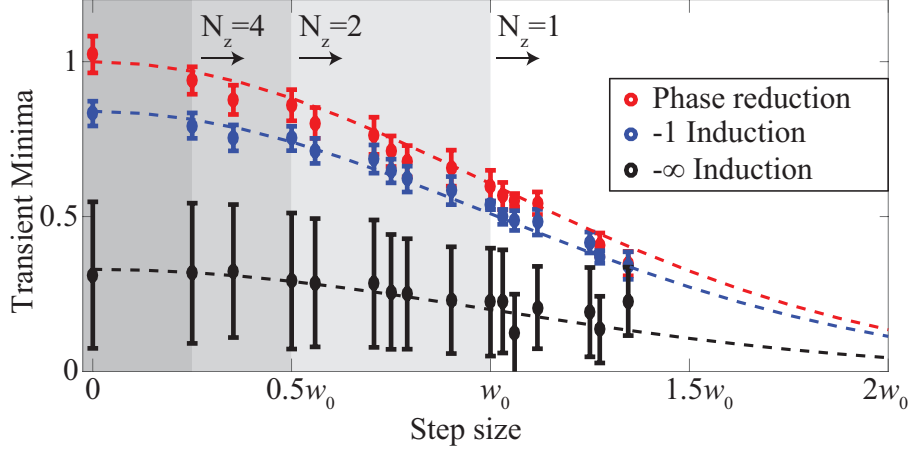


Figure 3.14: Monte-Carlo simulation of trap intensity transient minima vs. step size (in unit of trap waist) for various algorithm modifications. Dotted-lines are  $C \times \exp(-x^2/2w_0^2)$  where  $C$  is 0.3, 0.8, and 1 (theoretical limit) for black, blue, and red, respectively. Shaded areas represent extended accessibility of smaller step size when zero-padding multiplier  $N_z$  is applied (see text). The errorbars represent standard deviation.

### 3.5.7 Algorithm performance

Now, we have efficient and fast dynamic holograms for real-time feedback operation. To apply those ingredients for reliable single-atom array formation, a slight technical variation on the implementation is required to resolve collision issues. Even though the collisions between filled traps are automatically avoided thank to Hungarian algorithm [110], collisions between filled and empty traps which are also detrimental for reliable shuttling are not considered yet. Our strategy is removing empty traps while shuttling the others. This is done by further modifying the target  $T_i^{(k)}$ . First, traps are classified into filled,  $(x_{\alpha(f)}, y_{\alpha(f)})$ , and empty traps,  $(x_{\alpha(e)}, y_{\alpha(e)})$ , respectively. Then the weights are calculated separately; the weights of empty targets  $T_i(x_{\alpha(e)}, y_{\alpha(e)})$  are gradually changed at different frame by a global factor, e.g., pre-defined numbers  $(0.7, 0.4, 0.1, \dots, 0.4, 0.7, 1)$  for each frame  $k = 1, 2, 3, \dots, f_{\#} - 2, f_{\#} - 1, f_{\#}$ , where  $f_{\#}$  is the number of total frames. Also,  $(x_{\alpha(f)}, y_{\alpha(f)})$  and  $(x_{\alpha(e)}, y_{\alpha(e)})$  are switched each others if needed at the middle of frame number  $f_{\#}/2$ . Such an amplitude modulation and position swaps are important for reliable and indefinite execution.

We conducted Monte-Carlo simulations for  $i=5$ ,  $f_{\#}=15$ ,  $N_z = 4$ , and  $11 \times 11$  square lattice with various modified GS algorithm where the fps is over 60 Hz. The results (one of them are shown in Fig. 3.13) are shown in Fig. 3.14. The black, blue, and red dots correspond to conventional GS, wiz-GS, and wiz-GS+phase reduction, respectively. The last result could reach to the theoretical limit.

Due to the limit of our SLM, the phase reduction could not be implemented in our experiments. Instead a built-in utility so-called overdrive [115] has been tested. It is overshooting the SLM voltage pixel-wise for minimizing phase transient. Unfortunately, the overdrive does not improve the overall performance in our application mainly due to the condition  $|\Phi^{(k)} - \Phi^{(k-1)}| \ll 1$  already holds relatively well. Also, our SLM is driven by PCIe card which consume data transfer time of  $\sim 2$  ms per frame. Direct frame transfer via GPU would improve fps from 60 Hz to 70 Hz in our current resource.

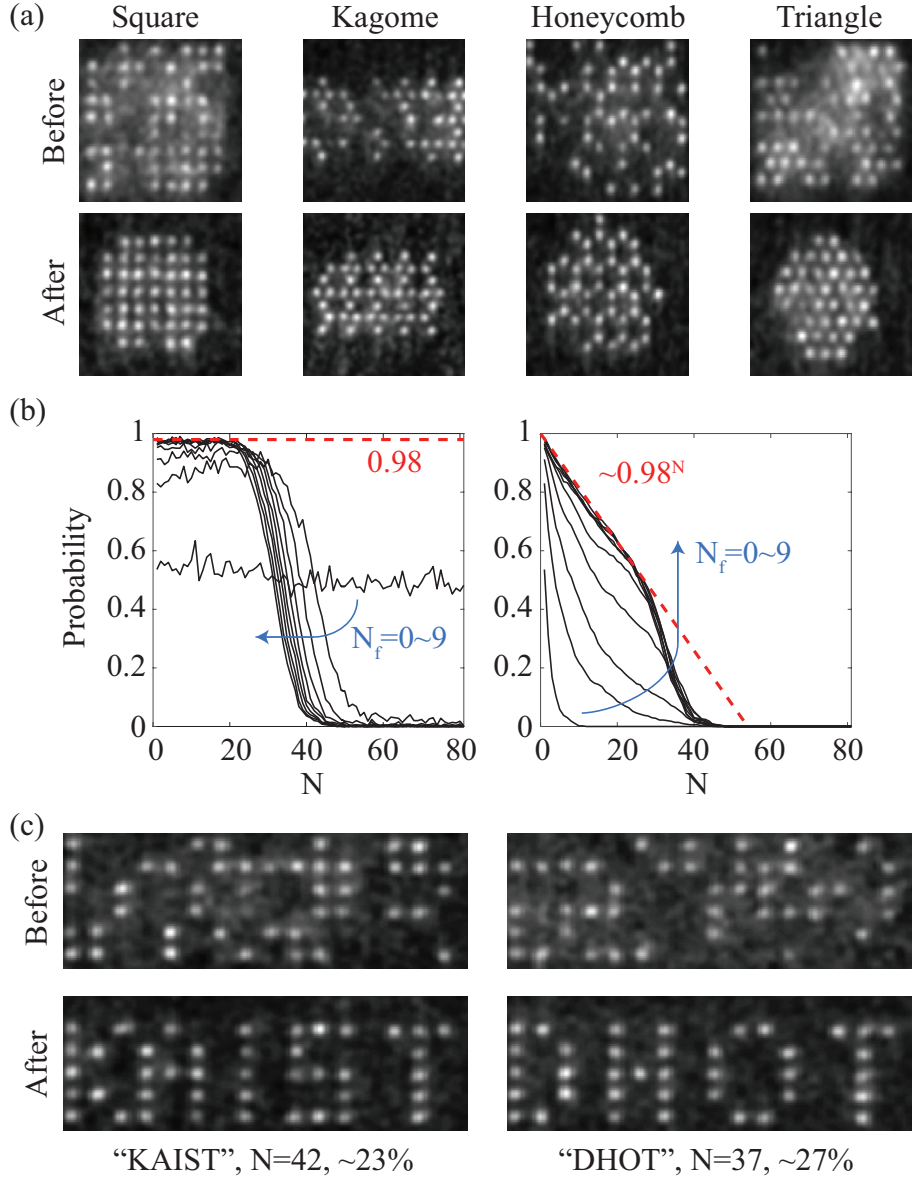


Figure 3.15: (a) Examples of compaction for various 2D arrays of initial 81 sites. (b) Black lines are loading probability of individual (left) and accumulated (right) sites from the center of array for the honeycomb lattice. (c) Examples of deterministic loading from initial 96 square lattice, representing capital letters. All the results were acquired by the same algorithm parameters, i.e. wiz-GS where  $i = 5$ ,  $N_z = 4$ ,  $n_i = -1$ , and  $f_{\#} = 15$  (see Algorithm section). The nearest distance is  $3.7 \mu\text{m}$  for all the arrays.

### 3.5.8 Results

Figure 3.15 (a) shows before and after images of compaction of 2D arrays from initial 81 sites to its center. In 'compaction' mode, all single atoms are simultaneously moved to form a defect-free 2D array, e.g., square, kagome, honeycomb, or triangle.

For showing more detailed results, the loading probabilities for honeycomb array are shown in Fig. 3.15(b); The left (right) plot is the (cumulative) single-atom loading probability for each site  $N = 1 - 81$ . The initial probability show  $\sim 0.5$  for entire array as expected, meanwhile the probabilities after several times of feedback reach to  $\sim 0.98$ . Considering the fact that feedback loop time is  $T = 0.5$ , the trap lifetime at dynamic equilibrium (even if shuttling is not needed, holograms are re-calculated continuously) is estimated as  $\tau=25$  s ( $0.98=\exp\{-T/\tau\}$ ). Compared to the static lifetime 40 s, the stability is decreased. It can be improved by implementing better aberration correction and PGC cooling (current 80  $\mu\text{K}$  to 30  $\mu\text{K}$  or lower). The right graph represents the probabilities of forming defect-free array larger than  $N$ . Nearly linear decay curve at the saturation matches well to the saturation probability 0.98. In Fig. 3.15 (c), examples of the second mode, 'deterministic loading', are presented. Compared to the previous mode, only pre-defined number of atoms are used for forming a complex shape of array, while the remains are reserved for next feedback stage.

### 3.5.9 Discussion

Speaking of fps, 60 Hz ( $i = 5$ ,  $N_z = 4$ ) is our current computational limit (i7-6700K, GTX Titan-X pascal), which is far slower than the SLM limit of 200 (500) Hz with(out) overdrive. Aside from hardware upgrade, parallel processing the frame calculation would improve fps much efficiently, though it should be carefully approached as the induction is an essential property for enabling atom shuttling. In Fig. 3.16, the transient minima are plotted for various induction parameter,  $n_i$  where the number refers to the history of previous phase. Here,  $-\infty$  means random initial phase. As shown in the plots, the overall energy conserving performances (red dots) are nearly maintained even up to  $n_i = 4$ . However, that of individual traps are significantly degraded as gray dots scatter away. Nevertheless, the frequency of detrimental effect (minima $<0.5$ ) is still kept low ( $< 1\%$ ) for  $n_i = 2$  and it may be worth taking the small loss for the sake of speed.

Our current limit for scalability are due to limited trap laser power, dynamic loss of atoms while shuttling, and collisional loss of atoms from the background. At our current trap wavelength 820 nm, about 3 mW power is required for individual trap. If the transmission of objective lens and transfer optics are optimized to 90 %, total 3.9 W power to support 1000 traps is required including SLM diffraction loss, which is readily achievable for commercial lasers. The shuttling loss occurs due to high atom temperature and trap inhomogeneity. Trap inhomogeneity should be diminished by applying the aberration correction using direct imaging [104] or indirect atomic fluorescence detection [102, 118], otherwise induces fluctuation on  $T/U$  and causes shuttling loss. If  $(I_{max} - I_{min})/I_{avg}$  can be down to 0.1, the global laser cooling process becomes more efficient. Then, by further optimizing the PGC or utilizing Raman cooling [119], the atom temperature can be down even below 10  $\mu\text{K}$  and the ratio, temperature over trap depth, may reach to 0.01, predicting frame-transit loss below  $10^{-10}$  in theory for 0.85 transient minima [43]. The background collision loss can be lowered by an order if double-MOT chamber is utilized. Thus the array lifetime  $\tau/N$  can exceeds the feedback time  $T$  even up to 1000 atoms. As the array larger, however, the shuttling distance increases about few times . Thus the number of frame for feedback,  $f_{\#}$ , should be multiplied in order to keep the shuttling loss low enough, inevitably

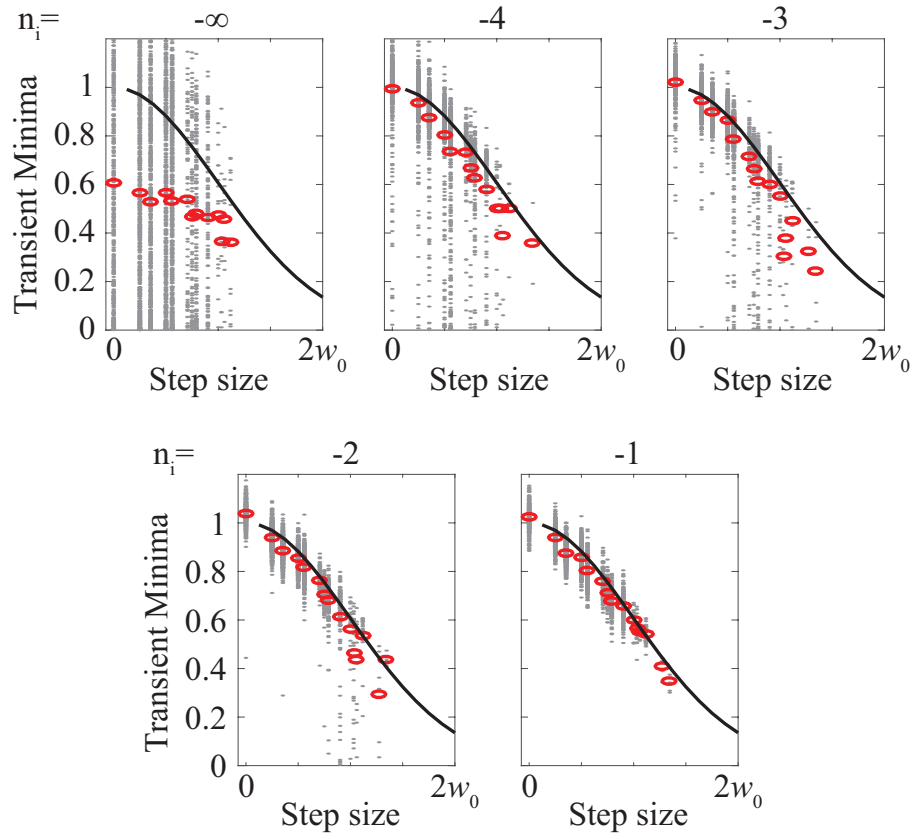


Figure 3.16: Monte-Carlo simulation of trap intensity transient minima vs. step size (in unit of trap waist) for various induction  $n_i$ , where  $\Phi_0^{(k)} = \Phi^{(k-n_i)}$  and wiz-GS+phase reduction. Black lines are  $\exp(-x^2/2w_0^2)$ . Gray dots are individual results and red dots are average of them.

table 3.1: Future perspectives for larger scale arrays.

	current	future
temperature	80 $\mu\text{K}$	10 $\mu\text{K}$
tau	40 s	400 s
fps	60	180
N(=tau/T)	80	800

increasing  $T$ . Hopefully, the parallel frame calculation by compromising the full induction,  $n_i = -1$ , to two or three may boost the fps to some extent. By combining them all together, from 1000 to 500 trap sites 'compaction' is viable in principle.

Lastly, we would like to discuss extension to three-dimensional array. For the 3D optical tweezers, 3D GS algorithm has been demonstrated [120, 121, 122]. However, its computational complexity is not reducible to an extent for real-time calculation of our frame movie. Instead, we propose the multi-plane 2D-GS algorithm [123], or just conventional GS with Fresnel lens random masking [42] for a few layers of 2D array. Especially the random masking only scales the complexity linearly to the number of layers, compromising the diffraction efficiency. It would be enabling real-time calculation even with our current resources up to 2 or 3 layers. The 3D layer imaging technique is also readily applicable in our setup [124].

## 3.6 Source code

I provide the source code of the holographic array synthesizer with the description of the program architecture. Figure 3.17 is a flowchart of the data throughout the entire hardware and software. First, the single-atom array fluorescence image is captured by the EMCCD. The EMCCD is controlled by the customized Labview including Matlab code inside. I would call it camera Labview. The camera Labview generates several text files, which are including individual array position, atom loading information, and target assignment information. The stand-by C++ program is dedicated to generate and execute hologram movies as fast as possible based on the information given by the text files. After then, the camera captures the array again and the sequence runs indefinitely. The entire trigger pulses are generated by another Labview called trigger Labview, except for the C++. The C++ is triggered by the text file.

### 3.6.1 Matlab

First, Matlab code is attached. This code is self-consistent, meaning that the Monte-Carlo simulation of a given array can be conducted without any hardwares (require GPU anyway) by copy and paste the entire codes below. The Matlab 2016 or above, and decent GPU is recommended for execution.

Define the grid for SLM.

```
xxx=-255:256;
[X, Y]=(meshgrid(xxx,xxx));
X=gpuArray(single(X));Y=gpuArray(single(Y));
```

The positions of tweezers are defined. The unit is arbitrary.

```
%%
Iter=2;
```

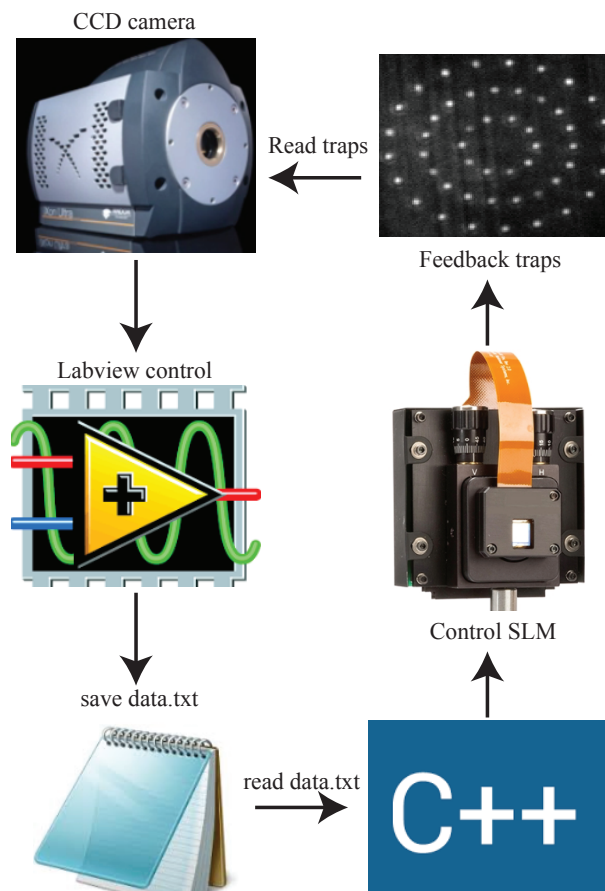


Figure 3.17: The data flowchart for the single-atom array synthesis.

```

for iter=1:Iter;iter %% iteration for atom loading events

%% positioner
%zigzag low 50distance 60deg 55site
[posX, posY]=meshgrid(-650:50:650, 290+sqrt(3)*25/2);
[posX1, posY1]=meshgrid(-675:50:675, 290-sqrt(3)*25/2);
posX=[posX';posX1'];
posY=[posY';posY1'];

```

The positions of tweezers are sorted according to the distances from the origin.

```

originX=0;originY=290;% origin position, user defined
posD=sqrt((posX-originX).^2+(posY-originY).^2);% distance from the origin
[posDsort, sorter]=sort(posD);% sorting distance

```

Define target and the frame number.

```

targeter=1:16; %used for deterministic loading. user dependent.

assigned=zeros([length(targeter),1]);
targeterxor=setxor(1:length(posX),targeter);
posX=[posX(targeter); posX(targeterxor)];
posY=[posY(targeter); posY(targeterxor)];
posXE= repmat(posX', [length(targeter),1]);
posYE= repmat(posY', [length(targeter),1]);
posXt=posX(1:length(targeter));posYt=posY(1:length(targeter));
posXtE= repmat(posXt, [1,length(posX)]);
posYtE= repmat(posYt, [1,length(posY)]);
framenum=20;
frameinc=(1:framenum)/framenum;
frameinc= repmat(frameinc, [length(posXt),1]);
posXtEf= repmat(posXt, [1,framenum]);
posYtEf= repmat(posYt, [1,framenum]);
posXEf= repmat(posX, [1,framenum]);
posYEf= repmat(posY, [1,framenum]);

```

Define the position and the single-atom fluorescence threshold on the camera. This is required when only the real experiment is concerned.

```

% %zigzag 60deg 55 site
% These positions and threshold values are used for CCD data treatment.
xx=[451 436 421 407 392 377 363 348...
    333 319 304 289 275 260 245 231...
    217 202 188 173 158 144 129 114...
    100 85 70 459 444 429 415 400...
    385 371 356 341 327 312 297 283...
    268 253 238 224 209 194 180 165...

```

```

        151 136 122 107 93 78 63];
yy=[24 24 24 24 24 24 24 24...
    24 24 23 23 23 23 23 23...
    23 22 22 22 22 22 22 21...
    21 21 21 12 12 12 12 12...
    12 12 11 11 11 11 11 11...
    11 11 10 10 10 10 10 10...
    10 9 9 9 9 9 9];
thress=[190 178 214 244 184 208 220 208...
        190 190 208 208 232 178 190 208...
        214 226 232 184 196 190 226 202...
        196 208 202 196 190 202 190 196...
        202 196 196 184 196 178 190 190...
        208 190 202 208 202 190 202 178...
        202 196 214 226 220 214 184];

```

This part is required when 'deterministic loadng' mode is operated.

```

% %This part is used for 'deterministic' mode.
% %Current mode is 'compactification' ('entropy lowering'), thus de-activated.
% xx=[xx(targeter), xx(targeterxor)];%deterministic
% yy=[yy(targeter), yy(targeterxor)];%deterministic
% thress=[thress(targeter), thress(targeterxor)];%deterministic
%
% digital=zeros(1,length(xx));%deterministic
% loading=zeros(length(xx),1);%deterministic
% loading2=zeros(length(xx),1);%deterministic
% loadingE=zeros(length(targeter),length(xx));%deterministic
% assigned=zeros(length(targeter),1);%deterministic

```

The initial phase making part.

```

%% phase maker
% Initial phase generator at the very start.
% Current option is random superposition phase as the initial.
if iter==1;
suminit=gpuArray(single(zeros(512)));
for k=1:length(posX);
    suminit=suminit+exp(1i*0.0012*(posX(k).*X+posY(k).*Y+2*pi*rand(1)));
% suminit=suminit+exp(1i*0.0012*(posX(k).*X+posY(k).*Y));
end;
phaseGSW1=angle(suminit);%(-pi : pi) domain
phaseGSW1=mod(uint32((phaseGSW1+pi)*255/2/pi),256);% 8bit 0-255 domain
% phaseGSW1=phaseinitial;
end;

```

The cost function generation and matching by Hungarian algorithm. The Matlab function 'munkres' is required, where it is attached in Appendix.

```

%% cost matrix generation
tic
loading=randi(2,[length(posX),1])-1;% random integer number generation 0,1

sumloading=sum(loading);

posXt=posX(sorter(1:sumloading)); % entropy lowering
posYt=posY(sorter(1:sumloading)); % entropy lowering
posXE= repmat(posX', [length(posXt),1]); % entropy lowering
posYE= repmat(posY', [length(posYt),1]); % entropy lowering
posXtE= repmat(posXt, [1,length(posX)]); % entropy lowering
posYtE= repmat(posYt, [1,length(posY)]); % entropy lowering
% targetsorted=[1:length(posXt)]; % deterministic

loadingE= repmat(loading', [length(posXt),1]);
tic
costmat=zeros(length(posXt),length(posX));
costmat=((posXE-posXtE).^2+(posYE-posYtE).^2).^(2/2)./loadingE;

costmat(isnan(costmat))=Inf;
assigned=(munkres(costmat)');
loading2=zeros(length(loading),1);
loading2=loading;
loading2(assigned==0)=1;
assignedlist(1:length(posXt),iter)=assigned;
assignedlistnum(iter)=length(posXt);
% assigned(assigned==0)=targetsorted((assigned==0));%deterministic,
% %un-assigend value to self value.
assigned(assigned==0)=sorter((assigned==0)); % low entropy

unassigned=setxor(1:length(loading),assigned);

```

The moving paths for each traps are defined according to the given matching solution. Note that 'deterministic loading' mode is de-activated.

```

clear posXpath;
clear posYpath;
posXpath=(zeros(length(posX),framenumber));
posYpath=(zeros(length(posY),framenumber));
for kqq=1:framenumber;%%path generation colliding path
posXpath(:,kqq)=posX;
posXpath(assigned,kqq)=(posX(assigned)-(posX(assigned)-posXt)/(framenumber)*(kqq));
posYpath(:,kqq)=posY;

```

```

posYpath(assigned,kqq)=(posY(assigned)-(posY(assigned)-posYt)/(framenumbers)*(kqq));
if kqq>framenumbers/2;
    posXpath(loading==0,kqq)=posX(sorter(sumloading+1:end)); % low entropy
    posYpath(loading==0,kqq)=posY(sorter(sumloading+1:end)); % low entropy
% posXpath(loading2(targetsorted)==0,kqq)=posX(assigned(assigned>length(posYt)));
% %deterministic loading
% posYpath(loading2(targetsorted)==0,kqq)=posY(assigned(assigned>length(posXt)));
% %deterministic loading

end;
end;

```

For call-out the C++ program, the data is written in the storage.

```

if trig==2;
loading2(unassigned)=0;%deterministic, remainder removal for certain condition.
end;

toc
trig=1;
save('C:\Program Files\ArrayFire\v3\examples\ModifiedGSWAlgorithm\posXpaths.txt'...
,'posYpath','-ascii');
save('C:\Program Files\ArrayFire\v3\examples\ModifiedGSWAlgorithm\posYpaths.txt'...
,'posXpath','-ascii');
save('C:\Program Files\ArrayFire\v3\examples\ModifiedGSWAlgorithm\assign.txt'...
,'unassigned','assigned','-ascii');
save('C:\Program Files\ArrayFire\v3\examples\ModifiedGSWAlgorithm\load.txt'...
,'loading2','trig','-ascii');

```

Re-scaling of paths. It is user defined.

```

posMetric=0.0012;
posX=gpuArray(single(posX*posMetric));posY=gpuArray(single(posY*posMetric));
posXpath=gpuArray(single(posXpath*posMetric));
posYpath=gpuArray(single(posYpath*posMetric));
assignedful=[unassigned; assigned];

```

Zero-padding part.

```

%% oversampler
numover=4;
[XX,YY]=meshgrid(1:512*numover,1:512*numover);
XX=gpuArray(single(XX));YY=gpuArray(single(YY));
gaussianform=exp(-((XX-512*numover/2).^2+(YY-512*numover/2).^2)/118^2);
circle=1-floor(((XX-512*numover/2).^2+(YY-512*numover/2).^2)/(512/2)^2);
circle=circle>0;
maske=gpuArray(gaussianform.*circle);

```

```
phaseover=gpuArray(single(zeros(512*numover)));
```

The number of iteration  $i$  for the GS algorithm is defined.

```
%% GSW operation
weights=gpuArray(single(ones(length(posX),1)));
peakvalues=gpuArray(single(zeros(length(posX),1)));
% phaseGSW1=phaseinitial;
for qq=1:framenum; [iter, qq]%moving
targetamp=gpuArray(single(zeros(512*numover)));
GSWiter=5;
if qq==framenum;
    GSWiter=5;
end;
```

The pixel crosstalk compensation [112]. It is user dependent.

```
rf=0.7;
sf=0.9;
psf=single(exp(-(X).^2/rf+(Y).^2/rf).^sf));
psf2=fft2(psf);
```

The weight and phase modulation depth are defined.

```
weighter=gpuArray(single(zeros([1,framenum])));
weighter(1:end)=0.1;
weighter(1:3)=[0.7 0.4 0.2];
weighter(framenum-4:framenum)=[0.1 0.1 0.4 0.7 1];
phasedepth=2;%2=2pi 4=4pi etc.
```

The wiz-GS operation.

```
for gswiter=1:GSWiter; % GSW iteration
    phaseGSW2=single(abs(iff2(fft2(phaseGSW1).*abs(psf2)/max(max(abs(psf2))))));
    phaseover(512*numover/2-255:512*numover/2+256,...
    512*numover/2-255:512*numover/2+256)=phaseGSW2/255*phasedepth*pi;
    phaseoverfft=(fftshift(fft2(maske.*exp(1i*(phaseover)))));
    peakvalues=(diag(phaseoverfft(round(posYpath(:,qq)/posMetric/(1.271*8/numover)+...
    512*numover/2),round(posXpath(:,qq)/posMetric/(1.271*8/numover)+512*numover/2))));

    weights(loading==1)=weights(loading==1).*mean(abs(peakvalues(loading==1)))/...
    abs(peakvalues(loading==1))/mean(weights(loading==1));

    if qq>3 && qq<framenum-3;
        weights(loading==0)=0.1;
    else
        weights(loading==0)=weights(loading==0).*mean(abs(peakvalues(loading==0)))/...
        abs(peakvalues(loading==0))/mean(weights(loading==0));
    end;
end;
```

```

    % weights(loading==0)=weights(loading==0)*(1/qqq+1/(framenumbers-qqq+1));
    weights(loading==0)=weights(loading==0)*weighter(qqq);
end;

for q=1:length(posX);
    qq=assignedful(q);
    targetamp(round(posYpath(qq,qqq)/posMetric/(1.271*8/numover)+512*numover/2),...
    round(posXpath(qq,qqq)/posMetric/(1.271*8/numover)+512*numover/2))=...
    gpuArray(single(0));
    targetamp(round(posYpath(qq,qqq)/posMetric/(1.271*8/numover)+512*numover/2),...
    round(posXpath(qq,qqq)/posMetric/(1.271*8/numover)+512*numover/2))=...
    weights(qq);
end;

%% GSW algorithm in Wikipedia
A=(ifft2(fftshift(targetamp.*exp(1i*angle(phaseoverfft)))));
phaseGSW1=angle(A(512*numover/2-255:512*numover/2+256,...
512*numover/2-255:512*numover/2+256));
phaseGSW1=mod(uint32((phaseGSW1+2*pi)*255/phasedepth/pi),256);
end;

% if qqq>1;%phase reduction for phasedepth=4
% phaseGSW1=phaseGSW1-uint32((phaseGSW1-phaseGSW1history(:, :, qqq-1))>256/4 &...
% phaseGSW1>256/2)*256/2;
% phaseGSW1=phaseGSW1+uint32((phaseGSW1-phaseGSW1history(:, :, qqq-1))<-256/4 &...
% phaseGSW1<256/2)*256/2;
% end;

end;
end;
end;

```

### 3.6.2 C++

The C++ code is for real-time feedback operation. It shows 60 fps for  $i = 5, N_z = 4$  when  $512 \times 512$  SLM is used. This code is stand-alone, designed to drive the Meadowlark XY-series (PCI-E) SLM. However, the matching information should be given by the .txt files. The examples of .txt files are shown in the above Matlab code.

```

#include <arrayfire.h>
#include <cstdio>
#include <cstdlib>
#include <fstream>
#include <vector>
#include <time.h>

```

```

#include "stdafx.h" // Does nothing but #include targetver.h.

#include <vector>
#include <cstdio>
#include <conio.h>
#include "Blink_SDK.H" // Relative path to SDK header.

#include <string.h>

using namespace af;

// Typedef for the container for our phase targets.
typedef std::vector<unsigned char> uchar_vec;

void loadArraysFromFiles(array &posXpath, array &posYpath, array &assigned)
{
    // posXpath and posYpath
    {
        std::vector<float> posXpathVec(35 * 20); // Current size from files
        std::vector<float> posYpathVec(35 * 20); // Current size from files

        std::ifstream posXFile("posXpaths.txt");
        if(!posXFile.is_open())
            std::cerr << "Error: posXpaths.txt failed to open" << std::endl;

        int i = 0;
        while(!posXFile.eof()) {
            posXFile >> posXpathVec[i++];
        }

        std::ifstream posYFile("posYpaths.txt");
        if(!posYFile.is_open())
            std::cerr << "Error: posYpaths.txt failed to open" << std::endl;

        i = 0;
        while(!posYFile.eof()) {
            posYFile >> posYpathVec[i++];
        }

        posXpath = array(20, 35, posXpathVec.data()).T();
        posYpath = array(20, 35, posYpathVec.data()).T();
    }
}

```

```

}

// assigned
{
    std::vector<float> assignVec(35); // Current size from files

    std::ifstream assignFile("assign.txt");
    if(!assignFile.is_open())
        std::cerr << "Error: assign.txt failed to open" << std::endl;

    int i = 0;
    while(!assignFile.eof()) {
        assignFile >> assignVec[i++];
    }
    assigned = array(35, assignVec.data()).as(u32);
}
}

void loadTrig(array &loading, array &trig){
    // loading and trig
    {
        std::vector<float> loadingVec(36); // Current size from files

        std::ifstream loadingFile("load.txt");
        if (!loadingFile.is_open())
            std::cerr << "Error: load.txt failed to open" << std::endl;

        int i = 0;
        while (!loadingFile.eof()) {
            loadingFile >> loadingVec[i++];
        }

        array loadingA(36, loadingVec.data());
        loadingA = loadingA.as(u32);
        loading = loadingA(seq(35));
        trig = loadingA(end);

        //af_print(loadingA(end));
    }
}

int main(int argc, char *argv[])
{

```

```

try {
    af::info();

    // SLM initialize
    const int board_number = 1;

    // Construct a Blink_SDK instance with Overdrive capability.

    const unsigned int bits_per_pixel = 8U;
    const unsigned int pixel_dimension = 512U;
    const bool is_nematic_type = true;
    const bool RAM_write_enable = true;
    const bool use_GPU_if_available = true;
    const char* const regional_lut_file = "slm4205_820.txt";
    const char* const loadlutfile = "slm4205_820nm_P8.lut";

    unsigned int n_boards_found = 0U;
    bool constructed_okay = true;

    Blink_SDK sdk(bits_per_pixel, pixel_dimension, &n_boards_found,
                  &constructed_okay, is_nematic_type, RAM_write_enable,
                  use_GPU_if_available, 2U, regional_lut_file);

    // load_LUT for non-overdrive
    //sdk.Load_LUT_file(board_number, loadlutfile);

    // Check that everything started up successfully.
    bool okay = constructed_okay && sdk.Is_slm_transient_constructed();

    if (okay)
    {
        enum { e_n_true_frames = 3 };
        sdk.Set_true_frames(e_n_true_frames);
        sdk.SLM_power(true);
        okay = sdk.Load_linear_LUT(board_number);
    }
    else
    {
        printf("gg");
    }

    //

    // Load Arrays From Files

```

```

array posXpath, posYpath, loading, trig, assigned;
loadArraysFromFiles(posXpath, posYpath, assigned);
loadTrig(loading, trig);
// These variables are not used here. Define them later.
//array weights = constant(1, loading.elements(), f32);
//array peakValues = constant(0, loading.elements(), c32);
//
//int frameNumber = posXpath.dims(1);

const array X = iota(dim4(1, 512), dim4(512, 1), f32) - 256.f;
const array Y = iota(dim4(512, 1), dim4(1, 512), f32) - 256.f;

array suminit = constant(0, 512, 512, c32);
array suminit1 = constant(0, 512, 512, c32);

{
    // prep work
    static const cfloat factor(0, 0.0012); // same as 1i * 0.0012
    // Generate loading.eelements random numbers along 3rd
    dimension and then tile
    array randVals = tile(2 * Pi * randu(1, 1, loading.elements(),
        ↪ f32), X.dims(0), X.dims(1), 1);

    // This tiles each values into a matrix and the 3rd dimension is
    ↪ for k
    // New dimensions are 512 x 512 x loading.elements()
    array posXpathVals = tile(moddims(posXpath(span, 0), 1, 1,
        ↪ loading.elements()),
        X.dims(0), X.dims(1), 1);
    array posYpathVals = tile(moddims(posYpath(span, 0), 1, 1,
        ↪ loading.elements()),
        Y.dims(0), Y.dims(1), 1);

    suminit1 += sum(exp(factor*
        ((posXpathVals * tile(X, 1, 1, loading.elements()))
        + (posYpathVals * tile(Y, 1, 1, loading.elements()))
        + randVals))
        , 2);

    // Clear the temporary arrays so that memory is not locked
    randVals = array();
    posXpathVals = array();
    posYpathVals = array();
}

```

```

array phaseGSW1 = arg(suminit1);
// Do round instead of u32 cast. Important to do %256 after
array phaseGSW11 = round(((phaseGSW1 + 2 * Pi) * (255 / (2 * Pi)))) %
    ↪ 256; // Do Round
array phaseGSW2 = constant(0, 512, 512, c32);
array phaseAmp = constant(1, 512, 512, f32);
array phaseU = constant(128, 512 * 512, u8);
static const int numOver = 4;
static const int numOver512 = 512 * numOver;

// These require +1 because meshgrid does 1 index
array XX = iota(dim4(1, numOver512), dim4(numOver512, 1), f32) + 1;
array YY = iota(dim4(numOver512, 1), dim4(1, numOver512), f32) + 1;

const array gaussianForm = exp(-(pow(XX - (numOver512 / 2), 2) + pow(YY
    ↪ - (numOver512 / 2), 2))
    / (2.f * 118 * 118));
const array gaussianForm2 = exp(-(pow(X, 2) + pow(Y, 2))
    / (2.f * 118 * 118));
array circle = 1 - floor((pow(XX - (numOver512 / 2), 2) + pow(YY - (
    ↪ numOver512 / 2), 2))
    / ((512 / 2) * (512 / 2)));
array circle2 = 1 - floor((pow(X, 2) + pow(Y, 2))
    / ((512 / 2) * (512 / 2)));
circle = circle > 0;
circle2 = circle2 > 0;

const array maske = gaussianForm * circle;
const array mask = gaussianForm2 * circle2;

array phaseover = constant(0, numOver512, numOver512, c32);
array phaseoverfft = constant(1, numOver512, numOver512, c32);
array targetAmp = constant(0, numOver512, numOver512, f32);
array phaseR = constant(0, numOver512, numOver512, c32);

const int GSWiter = 5;
const float rf = 0.7;
const float sf = 1;

const array psf = exp(-pow(((X * X) / rf) + ((Y * Y) / rf), sf)).as(f32
    ↪ );
array psf2 = fft2(psf);

```

```

psf2 = abs(psf2) / tile(max(abs(flat(psf2))), psf2.dims());

array weights = constant(1, loading.elements(), f32);
array peakValues = constant(0, loading.elements(), c32);
int frameNumber = posXpath.dims(1);

static const cfloat oneI(0, 1);
array loading0Idx = where(loading == 0); //loading.elements() is the number
    ↪ of elements. seq(loading.elements()) is 0:1:#-1

array loading1Idx = where(loading == 1);
array weighter = constant(0.1, frameNumber, 1, f32);
weighter(0) = 0.7; // ((float)0.8, (float)0.6, (float)0.4, (float)0.2);
weighter(1) = 0.4;
weighter(2) = 0.1;
weighter(frameNumber-5) = 0.1; // ((float)0.4, (float)0.6, (float)0.8,
    ↪ (float)1, (float)1);
weighter(frameNumber - 4) = 0.1;
weighter(frameNumber - 3) = 0.4;
weighter(frameNumber - 2) = 0.7;
weighter(frameNumber - 1) = 1;
af_print(weighter);
array qq = assigned(seq(loading0Idx.elements())) - 1;
array qq1;
if (loading0Idx.elements() == loading.elements()){
    loading1Idx = loading0Idx;
    qq1 = qq;
}
else{
    seq qass(loading0Idx.elements(), loading.elements() - 1); // seq
    ↪ qass(a,a)=a
    qq1 = assigned(qass) - 1;
}

// The offsets here are 0 indexed so thats why the increment/decrement
const seq S(numOver512 / 2 - 256, numOver512 / 2 + 255);

while (1){

    FILE *f;

    while (1){

```

```

Sleep(1);
loadTrig(loading, trig);
//printf("%d", trig.nonzeros());
if (trig.nonzeros()){ //from here to qqq-for-loop : 13ms.

    break;
}

}

trig = 0;

loadArraysFromFiles(posXpath, posYpath, assigned);

loading0Idx = where(loading == 0);
loading1Idx = where(loading == 1);

qq = assigned(seq(loading0Idx.elements())) - 1;

if (loading0Idx.elements() == loading.elements()){
    loading1Idx = loading0Idx;
    qq1 = qq;
}
else{
    seq qass(loading0Idx.elements(), loading.elements() - 1); // seq qass(a,
    ↪ a)=a
    qq1 = assigned(qass) - 1;
}

}

timer::start();
for (int qq = 0; qq < frameNumber; qq++) {

    for (int gswiter = 0; gswiter < GSWiter; gswiter++) {
        phaseGSW1 = abs(iff2(fft2(phaseGSW11.as(f32)) * psf2)).
        ↪ as(f32); //+2Hz (5iter)
        phaseGSW2 = mask * exp(oneI * (phaseGSW1 * 0.0246)); // *
        ↪ phaseAmp;
        phaseover(S, S) = phaseGSW2;
        phaseoverfft = shift(fft2(phaseover), phaseover.dims(0) /
        ↪ 2, phaseover.dims(1) / 2);
        //peakValues = diag(phaseoverfft(
        //round(posYpath(span, qq) / (1.271 * 8 / numOver) + (
        ↪ numOver512 / 2 - 1)),
        //round(posXpath(span, qq) / (1.271 * 8 / numOver) + (

```

```

    ↪ numOver512 / 2 - 1)))));
peakValues = diag(phaseoverfft(round(posYpath(span, qq)
    ↪ / (1.271 * 8 / numOver) + (numOver512 / 2 - 1)),
    ↪ round(posXpath(span, qq) / (1.271 * 8 / numOver)
    ↪ + (numOver512 / 2 - 1)))));

if (loading0Idx.elements() == loading.elements() ||
    ↪ loading1Idx.elements() == loading.elements()){
    weights(span) *= tile(mean(abs(peakValues(span)),
        ↪ loading.elements() / abs(peakValues(span)
        ↪ ) / tile(mean(weights(span)), loading.
        ↪ elements()));

    targetAmp(round(posYpath(span, qq) / (1.271 * 8 /
        ↪ numOver) + (numOver512 / 2 - 1)) + round(
        ↪ posXpath(span, qq) / (1.271 * 8 / numOver)
        ↪ + (numOver512 / 2 - 1)) * targetAmp.dims
        ↪ (0))
        = weights(span);
}
else{
    array pv1a = abs(peakValues(loading1Idx));

    array pv0a = abs(peakValues(loading0Idx));

    if (qq > 2 && qq < frameNumber - 3){
        weights(loading0Idx) = tile(weighter(qq),
            ↪ loading0Idx.elements());
    }
    else{
        weights(loading0Idx) *= (tile(mean(pv0a),
            ↪ loading0Idx.elements() / pv0a
            ↪ / tile(mean(weights(loading0Idx)),
            ↪ loading0Idx.elements())
            ↪ * tile(weighter(qq), loading0Idx.
            ↪ elements()));
    }

weights(loading1Idx) *= tile(mean(pv1a), loading1Idx.elements() / pv1a / tile(
    ↪ mean(weights(loading1Idx)), loading1Idx.elements()));
    /* (1 / ((float)qq + 1) + 1 / ((float)
    ↪ frameNumber - ((float)qq + 1) + 1));

// Use linear indexing = y * d0 + x

```

```

// Simply doing targetAmp(x, y) will result in M*N
    ↪ number of elements.
// This worked in the for loop as both x and y
    ↪ were 1.
// But when using batched mode, x and y are 121
    ↪ each result in 14641 values
// while weights(qq) is 121 only.
// So use linear indexing.
targetAmp(round(posYpath(qq, qq) / (1.271 * 8 /
    ↪ numOver) + (numOver512 / 2 - 1)) +
    round(posXpath(qq, qq) / (1.271 * 8 /
    ↪ numOver) + (numOver512 / 2 - 1)) *
    ↪ targetAmp.dims(0))
    = weights(qq);

targetAmp(round(posYpath(qq1, qq) / (1.271 * 8 /
    ↪ numOver) + (numOver512 / 2 - 1)) +
    round(posXpath(qq1, qq) / (1.271 * 8 /
    ↪ numOver) + (numOver512 / 2 - 1)) *
    ↪ targetAmp.dims(0))
    = weights(qq1);
}
/*for (int q = 0; q < loading.elements(); q++) {
    array qq = assigned(q)-1;
    targetAmp(round(posYpath(qq, qq) / (1.271 * 8 /
    ↪ numOver) + (numOver512 / 2-1)),
    round(posXpath(qq, qq) / (1.271 * 8 / numOver) +
    ↪ (numOver512 / 2-1)))
    = weights(qq);
}*/

phaseR = ifft2(shift(targetAmp * exp(oneI * arg(
    ↪ phaseoverfft)), numOver512 / 2, numOver512 / 2));
//phaseR = ifft2(shift(targetAmp , numOver512 / 2,
    ↪ numOver512 / 2));
phaseGSW1 = arg(phaseR(S, S));
phaseGSW11 = round(((phaseGSW1 + (6.2832)) * (40.5845)))
    ↪ % 256; // Do Round
}

unsigned char *puc = phaseGSW11.as(u8).host<unsigned char>(); //
    ↪ 7ms

```

```

        //printf("elapsed seconds: %g\n", timer::stop());
        okay = sdk.Write_overdrive_image(board_number, puc);
        //okay = sdk.Write_image(board_number, puc, pixel_dimension);
        targetAmp = constant(0, numOver512, numOver512, f32);
        af::freeHost(puc);

    }
    sync(); printf("elapsed seconds: %g\n", frameNumber / timer::stop());

    f = fopen("load.txt", "w");
    for (int i = 0; i < loading.elements()+1 ; i++){
        fprintf(f, "%d\n", 0);
    }
    fclose(f); // 1ms
    //printf("elapsed seconds: %g\n", timer::stop());
    //system("PAUSE");

}

    system("PAUSE");

} catch (af::exception& e) {
    fprintf(stderr, "%s\n", e.what());
    throw;
}

return 0;
}

```

## Chapter 4. A Rydberg atom quantum simulator

In this chapter, the constructed single-atom array synthesizer is used for a Rydberg quantum simulation experiment. In details, the  $^{87}\text{Rb}$  single-atom array of zigzag chain is formed and excited to  $67S_{1/2}$  Rydberg state. The excitation manifests global sudden quench on the array. The experiment is designed to simulate sudden quench dynamics of quantum Ising-like spin-1/2 system. The observed dynamics show the thermalization that any postulated randomness or coupling to baths are not required. The below sections are describing the experimental details.

### 4.1 Brief Introduction

Rydberg atom is an excited atom to a high principal quantum number, usually  $n \geq 10$  [125]. The orbital size is proportional to  $n^2$  according to Bohr model. The size becomes as large as  $1 \mu\text{m}$  for  $n \sim 100$ . The binding energy is proportional to  $n^{-2}$ , and the energy difference between nearby states is  $n^{-3}$ . The transition dipole moment between nearby Rydberg states, e.g.  $\langle nP | er | nS \rangle$ , is proportional to  $n^2$  as well. However, the transition dipole moment between the ground and a Rydberg state, e.g.  $\langle 5P | er | nS \rangle$ , is proportional to  $n^{-1.5}$  because the wave-function overlap between those levels are reduced [126].

The lifetime (spontaneous decay) of Rydberg states is expected to be longer than that of lower lying states due to the decreasing dipole moment,  $n^{-1.5}$ . Indeed, the lifetime scales by  $n^{-3}$  [126]. If  $n$  increases, the blackbody radiation of thermal background induces stimulated emission to the other nearby Rydberg states. It affects to the effective lifetime of the Rydberg states. For example,  $n \sim 60S$  Rydberg states of Rubidium atoms have  $\sim 200 \mu\text{s}$  spontaneous decay time and  $\sim 200 \mu\text{s}$  blackbody induced decay time. Thus the net lifetime is only  $\sim 100 \mu\text{s}$  [127].

Nevertheless, the lifetime of  $100 \mu\text{s}$  is long enough to observe its quantum nature, and the Rydberg states can be assumed as a good quantum system. For example, Rabi oscillation between  $n = 5$  and  $n \sim 60$  of Rubidium atom is considered. To observe the coherence of the system, Rabi frequency should be much faster than  $10 \text{ kHz}$ . The modern laser technologies are matured enough to exceed  $1 \text{ MHz}$  Rabi frequency between those levels.

Additionally, Rydberg atoms have strong dipole interaction. A Rydberg state, such as Rubidium  $60S$ , has zero dipole moment however the electron cloud is as large as sub-micrometer. If such two Rydberg atoms are close enough, they interact due to induced dipole-dipole. For example, two Rubidium  $67S$  atoms have  $2\pi \times 5 \text{ MHz}$  repulsive interaction at  $5 \mu\text{m}$  distance from each other. The interaction is  $V = -C_6/r^6$ , where  $C_6$  is van-der Waals coefficient and  $r$  is inter-atomic distance [128]. The coefficient is calculated by direct diagonalization method with open source program [129].

In the above sense, Rydberg atoms have been a promising candidate for a quantum information platform and quantum simulator [130, 131].

### 4.2 Rydberg atom excitation

For Rubidium atoms, UV laser of  $297 \text{ nm}$  wavelength is required to excite the ground state atoms to a Rydberg state by one-photon transition. Such experimental setups have been demonstrated in tweezer traps and optical lattice [132, 133, 134].

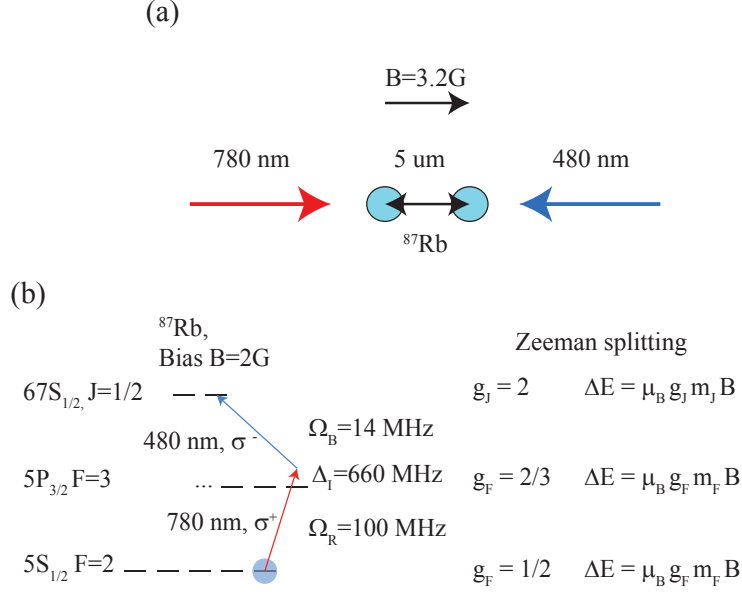


Figure 4.1: (a) Counter-propagating two-photon excitation to a Rydberg state. The B field defines quantization axis. (b) Graphical representation of our Rydberg excitation scheme with Rabi frequency and detuning ( $1/2\pi$  scaled). The Rydberg hyper-fine splitting is an order of 10 kHz thus it is treated in  $J$  basis. Zeeman splittings of individual states are shown as well, where the two-level scheme ( $|5S_{1/2}, F = 2, m_F = 2\rangle$  and  $|67S_{1/2}, J = 1/2, m_J = 1/2\rangle$ ) is robust against magnetic field fluctuation.

In this experiment, Rydberg excitation by two-photon transition (480 nm and 780 nm) is used. The two-photon excitation scheme has been widely used one [126, 130, 135, 44, 106, 107]. This scheme can access to both  $nS$  and  $nD$  states. The  $nS$  state has homogeneous van-der Waals interaction in which it is suitable for our application. In this case, the  $\sigma^\pm$  excitation scheme is robust against magnetic field fluctuation [126].

#### 4.2.1 Level scheme and Rydberg lasers

In the main experiment, the two lasers are counter propagating along the quantization axis  $67S$  and state is used as shown in Fig. 4.1.

To make robust two-level quantum system, the large detuning  $\Delta_I$  is introduced. The three-level Hamiltonian (with rotating wave approximation) is written as,

$$H_{three} = \begin{bmatrix} \frac{\Omega_B^2}{4\Delta_I} & \frac{\Omega_B}{2} & 0 \\ \frac{\Omega_B}{2} & \Delta_I & \frac{\Omega_R}{2} \\ 0 & \frac{\Omega_R}{2} & \frac{\Omega_R^2}{4\Delta_I} \end{bmatrix}. \quad (4.1)$$

By solving Schrödinger equation and applying adiabatic elimination on the intermediate level, the two-level system with two-photon Rabi frequency  $\Omega = \Omega_R \Omega_B / 2\Delta_I$  is derived. Note that the ac-Stark shift  $\Omega_{R,B}^2 / 4\Delta_I$  should be included for resonant condition, and the condition  $\Omega_R, \Omega_B \ll \Delta_I$  should be satisfied for eliminating the intermediate level.

For the experiment, the two Rydberg lasers (480 nm and 780 nm) are required. 780 nm Rydberg laser is a home-built external cavity diode laser (ECDL) and 480 nm Rydberg laser is a commercial

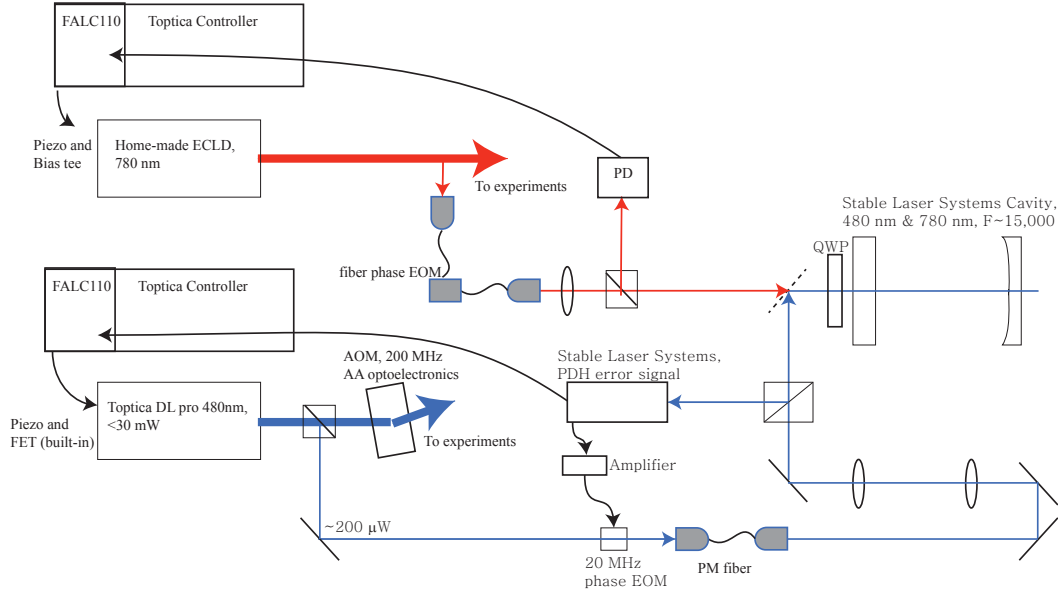


Figure 4.2: Two Rydberg lasers are frequency locked to external cavity setup. 480 nm and 780 nm lasers are 20 MHz phase modulated by free-space electro-optic modulator (EOM) and coupled to the cavity and then the Pound-Drever-Hall (PDH) signal is generated. An additional fiber phase EOM is used for 780 nm laser. The PDH signals are fed into the fast analogue lock servo (TOPTICA, FALC110). The lock servo generates the error signal to stabilize the laser frequencies to one of the cavity comb. The commercial 480 nm laser (TOPTICA, DLpro) enables to easily feed the error signal into the back-plane BNC connector. The home-built 780 nm laser needs to be modified for stable cavity lock; high frequency bias tee (Thorlab, TG100) is added for fast current modulation.

ECDL (TOPTICA, DLpro). Each laser is driven by a commercial electronics (TOPTICA, DL100) and has 30 mW power, respectively.

The laser frequencies should be stabilised to the known point to reliably excite the atoms to a Rydberg state. The frequency lock setup is shown in Fig. 4.2. The laser frequencies were locked to an ultra-low-expansion (ULE) Fabry-perot cavity (Stable Laser Systems, ATF-6010-4). The ULE cavity was cylinder shaped and of dual-wavelength, 15,000 finesse, and 1.5 GHz comb spacing. The cavity housing (Stable Laser Systems, VH6010-4) was kept in ultra low vacuum condition ( $< 10^{-7}$  Torr) and locked to precisely measured zero-crossing temperature of the cavity. The long-term temperature drift of the cavity was kept within 10 mK, resulting in absolute frequency drift below 1 kHz on both lasers. The achieved linewidths were estimated to below 10 kHz.

780 nm laser is locked to the first order sideband peak from the fiber EOM. The sideband peak is ranged from  $\sim 50$  MHz to  $\sim 500$  MHz, controlled by an external RF source (SRS, SG380). By sweeping the RF source, 780 nm frequency can be fine tuned. Note that the RF signals for every EOMs and AOMs are phase locked to a commercial 10 MHz reference clock (SRS, FS725).

## 4.2.2 Rydberg resonance finding

To find resonance frequency for Rydberg excitation, the electromagnetic induced transparency (EIT) is firstly used as shown in Fig. 4.3. The energies of Rydberg levels are given by the below as explained

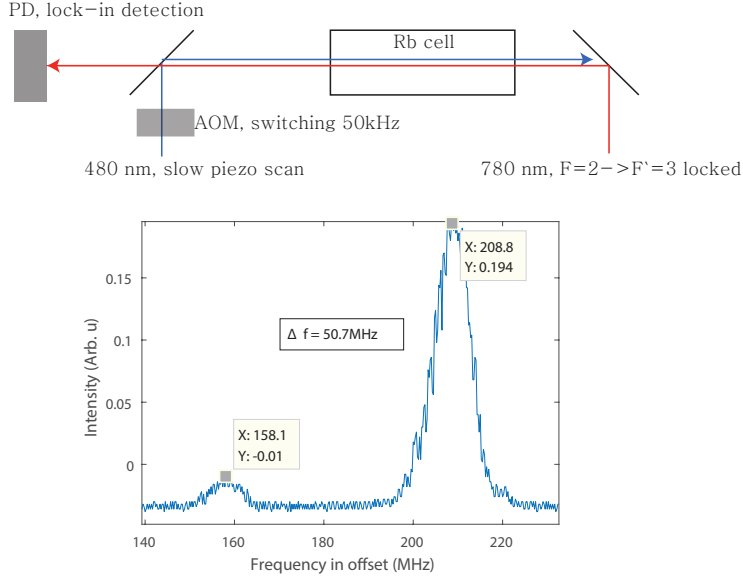


Figure 4.3: Rydberg EIT signal for 61D states. 780 nm laser is locked to  $F = 2 \rightarrow F' = 3$ . 480 nm laser frequency is slowly scanned by piezo transducer. 480 nm laser is switched 50 kHz by AOM. 780 nm laser is detected by PD and lock-in amplifier (SRS, SR830). The resulting Rydberg EIT signal shows 61D states.

table 4.1: Quantum defect for  $^{87}\text{Rb}$  Rydberg states [136].

$nS_{1/2}$	$\delta_0 = 3.131\ 180\ 7(8)$
	$\delta_2 = 0.178\ 7(2)$
$nD_{3/2}$	$\delta_0 = 1.348\ 094\ 8(11)$
	$\delta_2 = -0.605\ 4(4)$
$nD_{5/2}$	$\delta_0 = 1.346\ 462\ 2(11)$
	$\delta_2 = -0.594\ 0(4)$

in Ref. [136],

$$E_{n,l,j} = E_i - \frac{R^*}{[n - \delta(n,l,j)]^2}, \quad (4.2)$$

where  $E_i$  is the ionization energy threshold and

$$R^* = \frac{1}{1 + \frac{m_e}{m_{87\text{Rb}}}} R_\infty = h \times 3289.82119466(2)\text{THz} \quad (4.3)$$

is the corrected Rydberg constant for  $^{87}\text{Rb}$ . For large  $n$ , the quantum defects  $\delta(n,l,j)$  can be approximated by the Rydberg-Ritz parameters,

$$\delta(n,l,j) \approx \delta_0 + \frac{\delta_2}{(n - \delta_0)^2} \quad (4.4)$$

Define effective principal quantum number  $n^* = n - \delta(n,l,j)$ , then hyperfine splitting of  $nS$  state of  $^{87}\text{Rb}$  is estimated by  $\Delta_{HFS} = \frac{3}{8} \times 34(3)\ \text{GHz} \times n^{*-3}$ . For  $67S$  state,  $\Delta_{HFS} \sim 50\ \text{kHz}$  which is negligible for the other interaction strength. Indeed,  $67S_{1/2}$  state is represented in  $J$  basis as shown in Fig. 4.1. The quantum defect table for  $^{87}\text{Rb}$  Rydberg states are given in table. 4.1. Then, the absolute energies and fine structure splitting of  $nD$  can be calculated. By comparing the calculation and the measured

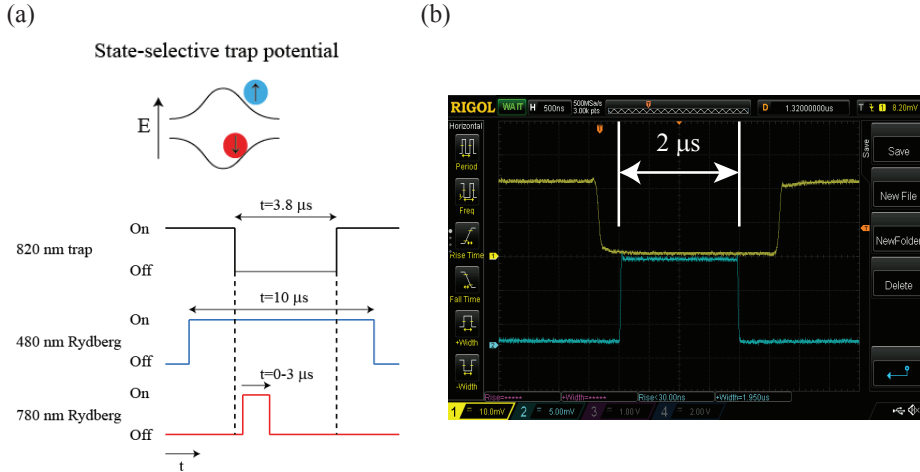


Figure 4.4: (a) The release & recapture protocol and the projection measurement. (b) Time trace of (yellow) switched 820 nm trap laser, and (blue) Rydberg 480 nm laser. The trap laser has rise/fall time of 100 ns.

energy difference in Fig. 4.3, the measured Rydberg EIT level is known as  $61D$ . For more convenient, the absolute wavelength of lasers are measured within 100 MHz accuracy by using the commercial wavelength meter (HighFinesse, WS7) and the calculated absolute energies are compared with it.

After finding the rough resonance frequency as the above method, the exact frequencies are found by using single-atom experiment.

### 4.2.3 The experimental protocol

The experimental protocol used here is so-called release & recapture protocol. It is widely used protocol in many similar experiments with two-photon excitation scheme [135, 44, 106, 107]. The schematic pulse time sequences of the protocol are shown in Fig. 4.4(a). The details are as follows: 480 nm Rydberg laser is turned on for 10 μs fixed duration. After 3 μs later, the dipole-trap beam is completely turned off for 3.8 μs fixed duration which is called release process in the protocol so that Rydberg levels were intact from the energy shift that was detrimental for reliable experiments. The interval should be short enough so that the trapped atom can be recaptured reliably. During the release period, the 780 nm Rydberg laser is switched on for 0-3 μs variable time with 100 ns step so that the Rydberg pulse length is precisely controlled. After the release period, the dipole-trap beam is turned on again for recapture process. This protocol naturally encompasses state-selective projection measurement of the ground and the Rydberg state. The recapture process itself is the state-selective detection between the ground and the Rydberg state because the dipole trap exerts repulsive force on the Rydberg state and rapidly kicks out the Rydberg atom while the ground state is recaptured again.

Switching of the three lasers (480 nm, 820 nm trap, and 780 nm) is performed with acousto-optic modulators (AOMs). Their rise/fall times were 50 ns, 100 ns, and 20 ns, respectively. All the switching speed satisfied the sudden quench condition we have discussed. The master triggers are generated by a computer controlled data acquisition board (NI, PCIe-6353), and more precise pulse width control is done by using delay generator (SRS, DG-535). The pulse time jitters and shot-to-shot power fluctuations are less than 10 ns and 2% (780 nm), 4% (480 nm), respectively, measured by using fast photo-detectors.

Those three lasers should be synchronously switched on and off for reliable experiment. The time

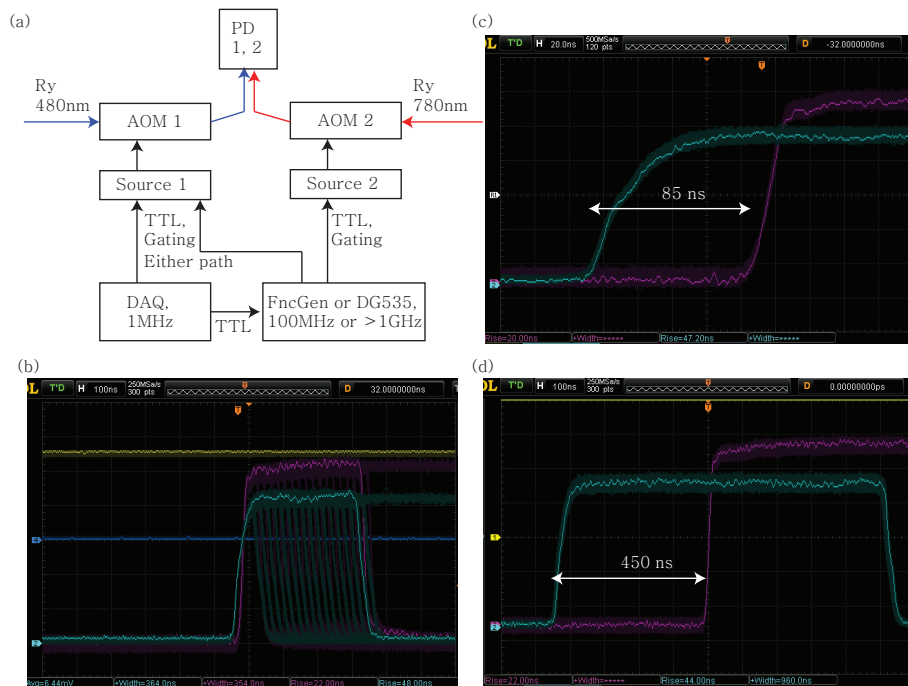


Figure 4.5: Rydberg pulse time analysis. (a) Analysis scheme. (b) Green (Ry 480 nm) and Red (Ry 780 nm) traces are optical pulses measured by fast PD (ET-2030, eotech). Both laser pulses are TTL gated by identical trigger generated from the function generator (DG4162, RIGOL). (c) 480 nm laser gating is generated from DAQ (6353, National Instrument) whereas 780 nm laser gating is generated from the DG535 (Stanford Research Systems). The DG535 is triggered by the same gating pulse of 480 nm laser. (d) 480 nm laser gating is generated from DAQ (6353, National Instrument) whereas 780 nm laser gating is generated from the DG4162. The DG4162 is triggered by the same gating pulse of 480 nm laser. The laser pulses arrive at the chamber or the fast PD after 250ns from the gating pulses.

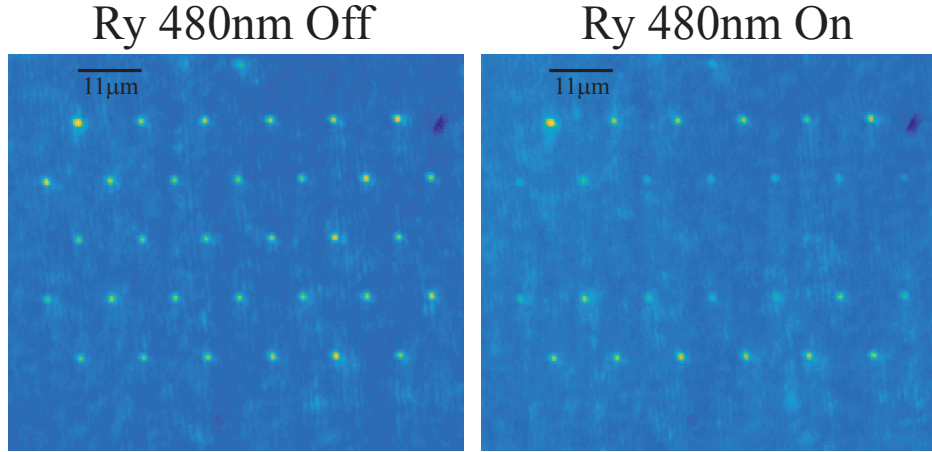


Figure 4.6: Rydberg 480 nm laser alignment scheme. The 480 nm laser beam has only 10  $\mu\text{m}$  diameter ( $1/e^2$ ). Tune the 480 nm wavelength to the near resonance of any Rydberg levels ( $nD_{5/2}$  is preferred) by using wave-meter. By turning on and off the laser, the penetration pattern on the atom array can be observed.

trace of those pulses are also measured by using the fast photo diode as shown in Fig. 4.4 and Fig. 4.5. By doing those measurement, the well time-aligned pulse sequence within 10 ns is achieved.

The beam diameters ( $1/e^2$ ) at the single-atom array are 80  $\mu\text{m}$ , 10  $\mu\text{m}$  for 780 nm, and 480 nm lasers, respectively. 480 nm laser beam size is small since the available power is limited to 10 mW. Two lasers are counter-propagating and the array is elongated along the propagation axis to achieve homogeneous interaction within 5% for the 2D area of over  $5 \times 100 \mu\text{m}^2$ .

Two Rydberg lasers are transferred to the single-atom chamber via single mode fiber. In front of the each fiber output port, a polarizer, quarterwave plate, and convex lens is located to focus the circular polarized beam onto the single-atom array. The 480 nm fiber delivers only Rydberg 480 nm laser. The 780 nm fiber delivers three kind of 780 nm beams;

1. Optical pumping beam,  $|5S_{1/2}, F = 2\rangle \rightarrow |5P_{3/2}, F' = 2\rangle$ , 3.3  $\mu\text{W}$  output power, switched by AOM.
2. Blowaway beam,  $|5S_{1/2}, F = 2\rangle \rightarrow |5P_{3/2}, F' = 3\rangle$ , 11  $\mu\text{W}$  output power, switched by AOM with extinction ratio  $> 60\text{dB}$ . Note that the AOM frequency also shifted for higher extinction ratio.
3. Rydberg beam, variable power.

The Rydberg laser alignment are done by observing continuously running MOT with overlapped trap array. For Rydberg 780 nm laser, the alignment is easily done. The 780 nm laser has large beam size and resonance condition on  $5P_{3/2}$  state. Those conditions make a lot easier to find whether the beam is aligned or not by observing blowaway of the trap array. For Rydberg 480 nm laser, the alignment is done by observing the blowaway pattern on the array as shown in Fig. 4.6. The 480 nm laser should be near resonant from  $5P_{3/2}$  to  $nD$  state where the blowaway condition is optimal.

#### 4.2.4 Stray electric field

Several experimental observations [128, 132, 137, 138] report that stray electric field inside a vacuum chamber exists. Such electric field induces energy shift on a Rydberg state. If the electric field is constant

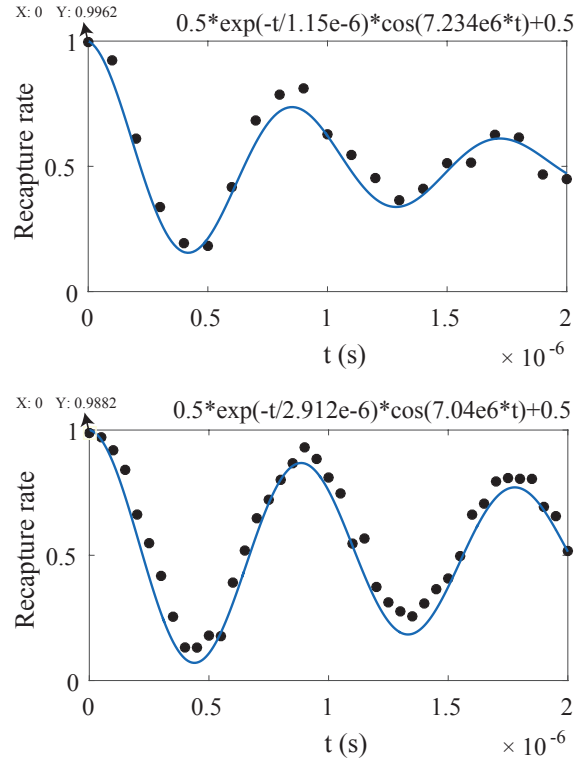


Figure 4.7:  $^{87}\text{Rb}$  Rydberg Rabi oscillation between  $|5S_{1/2}, F = 2, m_F = 2\rangle \rightarrow |6^7S_{1/2}, J = 1/2, m_J = 1/2\rangle$ . The protocol and excitation scheme were the same as in Fig. 4.1. The bias B-field was 2 G. (Up) Before ground connection of the nearby metals. (Down) After ground connection of the nearby metals. The oscillation was fitted by exponential decaying cosine function. The time-zero errors are 0.004 and 0.012, respectively.

over long time, it would not be a significant problem on a Rydberg atom experiment. However, those fields drift in long time scale [128, 138], usually several minutes to an hour. The origin of such field is known to be a glass surface charge, or laser induced charge.

Glass surface charge due to adsorbed Rb atoms [137] induces the amount of 10 – 100 mV/cm field at 1 cm apart from the surface. Laser induced charge due to high power laser or UV laser [132] is known that they are formed by surface layer desorption or deformed chemical bonding on the material.

In the Rydberg experiment, long-term drift of the electric field causes significant problem; the resonance condition for laser excitation of Rydberg state varies over time and reliable experiment would not be possible. It was reported that Indium-Tin-Oxide(ITO) coating on the nearby glass reduced those long-term drift [128].

Meanwhile, the Rydberg experiment by using atomic vapor cell does not suffer from the drift issue [138]. It has known that the atomic vapor cell acts as a Faraday cage. The cell has  $\sim 10^{-7}$  Torr at room temperature for Rb atoms. Inside the vapor cell surface, Rb atoms are adsorbed due to the high concentration. Those adsorbed atoms are assumed to be one of the main reason for forming the Faraday cage. In the Ref. [138], they exerted radio-frequency electric field pulse onto the vapor cell to change the electric field inside the cell. The Faraday cage had limited bandwidth for shielding the external field.

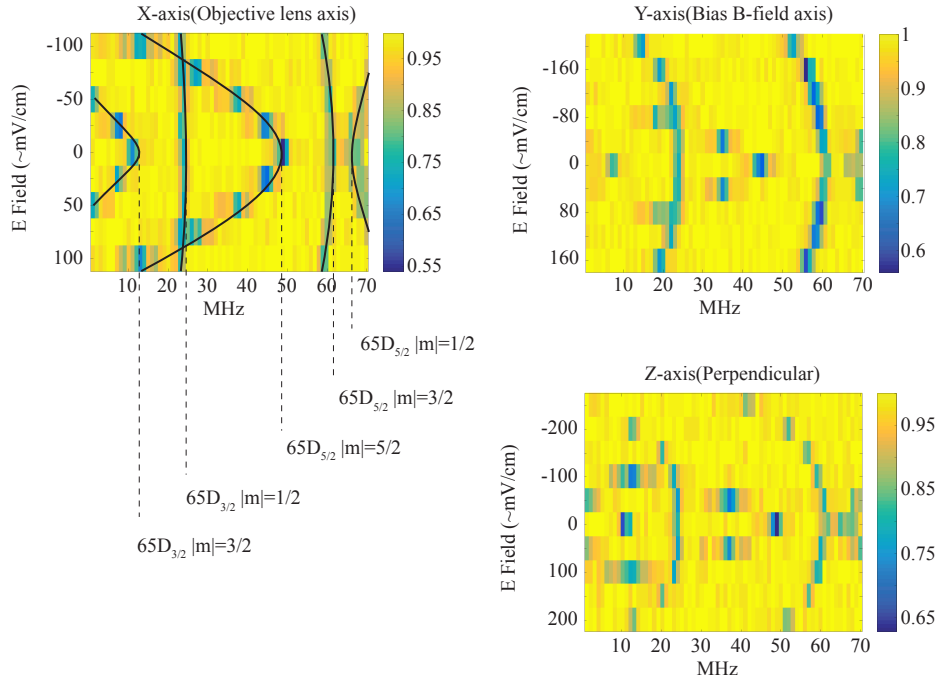


Figure 4.8: 3 dimensional electric field scan for  $^{87}\text{Rb}$  65D Stark map measurement. The experiment was done by using single-atom array and release & recapture protocol. There was no bias B-field and optical pumping on this experiment. The laser excitation scheme was the same for the other experiment; counter-propagating  $\sigma^\pm$  polarization. The quadrant metal plates [128] were placed outside the glass cell. The electric field was controlled by function generator to exert radio-frequency pulse. DC-field from the outside did not penetrate the glass cell. It is intriguing fact that the glass cell had only pressure of  $10^{-10}$  Torr, but still shows the feature of Faraday cage.

### Experiment1: Rabi oscillation

For finding the exact Rydberg resonance condition in my experiment, single-atom array was prepared and release & recapture protocol was used. The 780 nm fiber EOM driving frequency was scanned to observe whether the array was excited or not. In the first experiment, 65D Rydberg state resonance peak was found. It is observed that the resonance peak was shifted 2 MHz if Rb getter voltage was changed by 1 V. By this observation, it is suspected that the nearby metal voltage fluctuation may induce the electric field fluctuation inside the chamber.

To clarify the theory, I connected every nearby metal components to the stable ground. The Rabi oscillation experiment were conducted as shown in Fig. 4.7. Two Rabi oscillation show distinctive quality; the partially connected case (up) shows 1.15  $\mu$ s Rabi oscillation decay time, while the fully connected case (down) shows 2.91  $\mu$ s decay time. In the case of no-connection, the Rabi oscillation could not be observed.

Note that the intermediate level detuning from  $5S_{1/2}, F = 2$  to  $5P_{3/2}, F = 3$  was  $\Delta_I = 2\pi \times 660$  MHz. The 780 nm Rabi frequency,  $\Omega_{780} = 2\pi \times 100$  MHz, was calibrated by Stark shift measurement [139]. Then, the 480 nm Rabi frequency,  $\Omega_{480} = 2\pi \times 14$  MHz, was deduced by two-photon Rabi frequency,  $\Omega_{780}\Omega_{480}/2\Delta_I \sim 2\pi \times 1$  MHz. The rest of my experiment has done by this condition.

### Experiment2: Stark map

By connecting the nearby metals to the stable ground, the long-term electric field fluctuation is reduced to an extent that the Rabi oscillation can be measured. It is still ambiguous whether the inside electric field is true zero or not. Moreover, it would be better if the field can be tuned to true zero.

In the Ref. [128], 3D electric field control was done by mounting 2 facing quadrant metal plates inside a vacuum chamber. They controlled 3D field to find the exact zero field point by measuring 3D Stark shift map. As a result, an improved Rabi oscillation was acquired.

The quadrant electrodes are mounted outside the glass cell in my case. At first, DC voltage was applied on those electrodes. However, none of the expected amount of resonance shift was observed. This is the evidence that the glass cell acts as a Faraday cage. Next, square shape voltage pulse of 10  $\mu$ s is applied by a function generator (DG4162, RIGOL) only during the release & recapture period. The resulting 3D Stark map is shown in Fig. 4.8. The observed state is  $^{87}\text{Rb}$  65D. The Rydberg D state shows quadratic-like DC-Stark shift [138], with 5 branches. Those 5 branches are clearly distinguished in my experiment. If the electric field is true zero, the branches merge together to form 2 and 3 fold degeneracies of  $D_{3/2,5/2}$ . In my experiment, however, they never merge together. The estimated electric field strength is about  $\sim 100$  mV/cm. The amount of the field can not be compensated in any direction. This observation is barely understood and should be carefully investigated later, by applying UV ramp onto the glass cell or mounting the electrodes inside the chamber.

## 4.3 Toward many-body experiments

Applying Rydberg atom excitation on the highly controllable atomic systems such as tweezer traps and optical lattices is of an important step toward simulating quantum many-body system [131] or investigating quantum information science [130].

Recently, such systems have proven their capabilities for simulating Ising-like quantum spin system [44, 106, 107, 133, 134, 135]. In this section, Ising-like quantum spin-1/2 system of zigzag chain of

single-atom array is simulated.

### 4.3.1 Detailed balance of thermalization dynamics in Ising-like quantum magnets

Dynamics of large complex systems, such as relaxation towards equilibrium in classical statistical mechanics, often obeys a master equation [140]. The equation significantly simplifies the complexities but describes essential information of occupation probabilities. A related fundamental question is the thermalization, a coherent evolution of an isolated many-body quantum state into a state that seems to be in thermal equilibrium. It is valuable to find an effective equation describing this complex dynamics. Here, we experimentally investigate the question by observing sudden quench dynamics of quantum Ising-like models implemented in our quantum simulator, defect-free single-atom tweezers in conjunction with Rydberg atom interaction. We find that saturation of local observables, a thermalization signature, obeys a master equation experimentally constructed by time-resolved monitoring the occupation probabilities of prequench states and imposing the principle of the detailed balance. Our experiment agrees with theories, and demonstrates the detailed balance in a thermalization dynamics that does not require coupling to baths or postulated randomness.

#### Introduction

It is a long-standing question whether and how a closed many-body quantum system coherently evolves into a steady state [141, 142, 143]. As variety of quantum simulators have been developed recently, there are number of experimental reports on thermalization [36, 35, 144, 145, 146]. There are also theoretical mechanisms, such as the eigenstate thermalization hypothesis (ETH) [147, 148, 149, 150, 151, 152], that tell us whether the steady state is practically indistinguishable from an equilibrium thermodynamic ensemble.

By contrast, the principles of dynamics toward the steady state remain largely unknown. The thermalization dynamics has the complexity exponentially increasing with system size; hence, its computation is impractical for large systems. Recently, a master equation was derived [153] for describing the thermalization dynamics of a quantum spin system. It is constructed in terms of transition rates between the eigenstates of the prequench Hamiltonian, and well describes the time evolution of local observables towards steady-state values (excepts some coherent oscillations). It is powerful as the number of the rates necessary for the construction increases only linearly with system size. We experimentally construct the master equation by preparing optical dipole traps with unit occupation of  $^{87}\text{Rb}$  atoms, and monitoring the global sudden quench dynamics to a Rydberg level.

#### Rydberg quantum simulator

We utilized the recently developed single-atom array synthesizer [43, 104, 105, 110] in conjunction with global Rydberg atom excitation. In Fig. 4.9(a), defect-free  $^{87}\text{Rb}$  single-atom chains of various size  $N = 10 - 25$  were formed by using dynamic holographic optical tweezers; note the images of an  $N = 25$  zigzag chain of bending angle  $\theta = 60^\circ$  in Fig. 4.9(b). We fixed the interatom distance  $d = 4.0(2) \mu\text{m}$  and changed the zigzag angle  $\theta$  from  $45^\circ$  to  $180^\circ$ . The entire array was coherently driven to  $67S_{1/2}$  Rydberg state with homogeneous interaction strength by adopting widely used two-photon excitation [44, 106, 107, 126, 135] (see Fig. 4.14 in Supplements). Each atom  $i$  behaved as a pseudo spin-1/2 system composed of the ground state  $|5S_{1/2}, F = 2, m_F = 2\rangle \equiv |\downarrow_i\rangle$  and the Rydberg

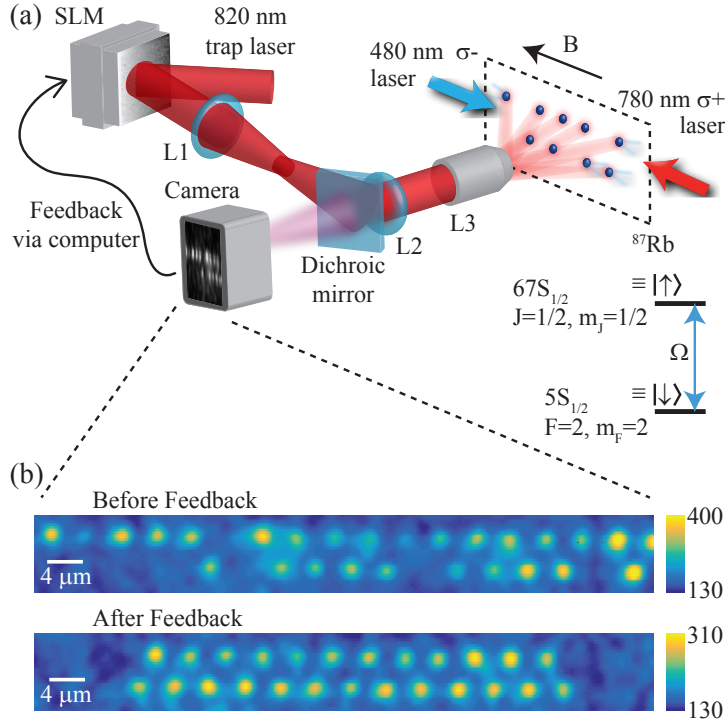


Figure 4.9: **Setup.** (a) The wave-front of trap laser is modulated by a liquid-crystal spatial light modulator (SLM) and imaged by a telescope (L1, L2) and an objective lens (L3). The fluorescence image of the trapped atoms is captured by a camera, and analyzed to feedback the SLM for array compactification by atom shuttling. Then, 480 nm and 780 nm lasers excite the array to  $67S$  Rydberg state, forming a tunable Ising-like spin-1/2 chain. (b) Zig-zag chain fluorescence images (Gaussian filtered for clarity).

state  $|67S_{1/2}, J = 1/2, m_J = 1/2\rangle \equiv |\uparrow_i\rangle$ , as intrinsic dephasing time  $16 \mu\text{s}$  was longer than experiment duration  $3 \mu\text{s}$  (see Supplements).

The system can be described by the Hamiltonian of an Ising-like spin-1/2 chain [44, 135, 106, 107],

$$H = H_0 + H_I = \sum_{i>j} V_{ij} \hat{n}_i \hat{n}_j + \sum_i \frac{\hbar\Omega}{2} \hat{\sigma}_x^{(i)} - \frac{\hbar\Delta}{2} \hat{\sigma}_z^{(i)}, \quad (4.5)$$

where  $\hat{n}_i = |\uparrow_i\rangle \langle \uparrow_i|$ ,  $\hat{\sigma}_x^{(i)} = |\uparrow_i\rangle \langle \downarrow_i| + |\downarrow_i\rangle \langle \uparrow_i|$ , and  $\hat{\sigma}_z^{(i)} = |\uparrow_i\rangle \langle \uparrow_i| - |\downarrow_i\rangle \langle \downarrow_i|$ . The first term  $H_0$  of Eq. (4.5), the repulsive van der Waals interaction  $V_{ij} = -C_6/|\mathbf{x}_i - \mathbf{x}_j|^6$  with coefficient  $C_6 = -470 \text{ GHz}/\mu\text{m}^6$  [129], behaves as interactions between the spins, while the second and third terms with Rabi frequency  $\Omega$  and detuning  $\Delta$  act as spin transverse Zeeman splitting  $H_I$ . The nearest neighbor interaction strength is estimated as  $V_{12}/2\pi\hbar = 14 - 25 \text{ MHz}$  for  $d = 4.0(2) \mu\text{m}$ , and the next nearest neighbor interaction strength  $V_{13}$  depends on  $\theta$ ;  $V_{13} = V_{12}/64$  for  $\theta = 180^\circ$  and  $V_{13} = V_{12}$  for  $\theta = 60^\circ$ . The fluctuation of  $V_{ij}$  is due to thermal atomic motions. There is a shot-to-shot noise on  $H_I$ , resulting in  $2 \mu\text{s}$  inhomogeneous dephasing time on collective Rabi oscillations (see Fig. 4.16 in Supplements); however, it does not qualitatively alter the equilibration dynamics under the parameters of  $H_0 \gg \hbar\Omega \gg \hbar|\Delta|$  [154].

### Thermalization

Initially,  $\Omega$  and  $\Delta$  are zero and the chain is in the ground state  $|\downarrow_1 \downarrow_2 \cdots \downarrow_N\rangle$  of  $H_0$ . Then, saying at  $t = 0$ , they are suddenly turned onto  $\Omega/2\pi = 1.0(1) \text{ MHz}$  and  $\Delta/2\pi = 0.0(1) \text{ MHz}$ . This global

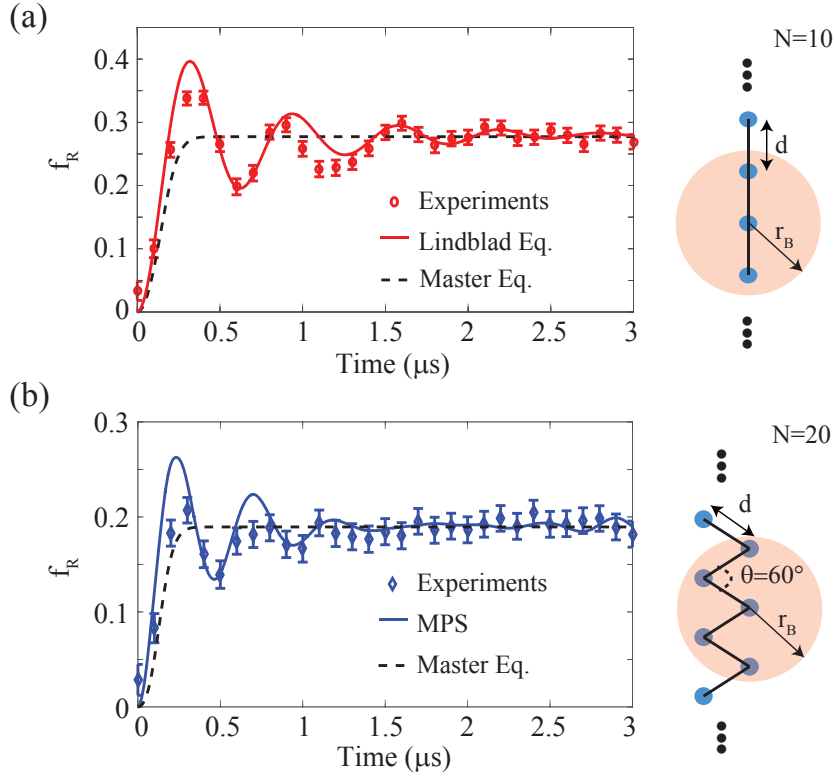


Figure 4.10: **Thermalization dynamics.** Time dependence of Rydberg fraction after the quench for (a) the linear chain of  $N = 10$  and  $\theta = 180^\circ$  and (b) the zigzag chain of  $N = 20$  and  $\theta = 60^\circ$ . The experimental data (circles) are compared with the computation (solid lines) and the result (dashed) of the master equation constructed based on the experimental data. The errorbars are standard error of the mean. Right panels: Chain configurations with blockade radius of  $r_B = (|C_6|/2\pi\Omega)^{1/6} = 6.5 \mu\text{m}$  and lattice spacing of  $d = 4.0(2) \mu\text{m}$ .

quench makes the measured Rydberg fraction  $f_R \equiv \sum_i \langle \hat{n}_i \rangle(t)/N$  change in time as in Fig. 4.10 (also see  $\sum_{i,j} \langle \hat{n}_i \hat{n}_j \rangle(t)/N^2$  in Fig. 4.18 of Supplements). The overall features of  $f_R$  are qualitatively the same for  $N \geq 10$ ;  $f_R$  shows coherent oscillations before it approaches to a steady-state value  $\bar{f}_R$ . The major frequency component of the oscillations occurs at  $\sqrt{2}\Omega$  for the linear chain and  $\sqrt{3}\Omega$  for the zigzag chain of  $\theta = 60^\circ$ , corresponding to the collective Rabi frequency of two or three atoms. The results agree with computations based on a Lindblad equation for  $N = 10$  and on matrix product states (MPS) for  $N = 20$  (see Supplements). Note that the shot-to-shot noise is taken into account for  $N = 10$ ; the noise effect becomes negligible for larger  $N$  [145, 150, 155].

Around the relaxation time  $t_{\text{relax}} = 1.5 - 2 \mu\text{s}$  for  $\theta = 60^\circ - 180^\circ$ , the oscillations are suppressed. We obtain the time-average  $\bar{f}_R$  at  $t \geq t_{\text{relax}}$ .  $\bar{f}_R$  follows the universal scaling behavior of  $\bar{f}_R \propto \alpha^\nu$  with  $\alpha \propto \hbar\Omega d^6/|C_6|$  (see Fig. 4.20 in Supplements). The measured exponent  $\nu = 0.16(2)$  agrees with the prediction [126, 156] based on the Hamiltonian  $H$ . All the above observations support that our system properly works as Rydberg quantum simulators [44, 106, 107, 157, 134].

### Detailed balance

To analyze the relaxation of  $f_R$ , we measure the probabilities  $P_n(t)$  with which there are  $n$  atoms in spin up  $|\uparrow\rangle$  at time  $t$ . In Fig. 4.11(a),  $P_n(t)$  exhibits coherent oscillations while diffuses to a steady-state

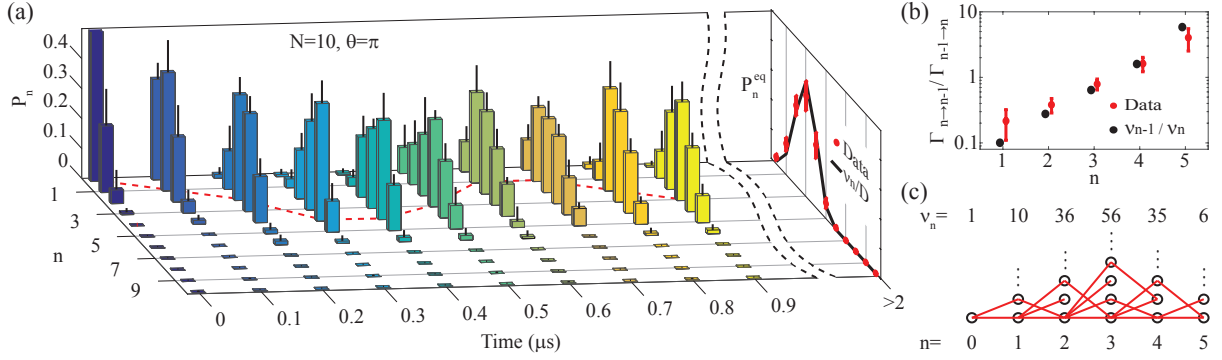


Figure 4.11: **Detailed balance in the linear chain of  $N = 10$ .** (a) The measured  $P_n(t)$  (color bars) and its standard deviation ( $\pm\sigma$ , overlaid black lines). At  $t > 2 \mu s$ , the measured data (red dots) and the theoretical predictions (black line) of the steady-state values  $P_n^{\text{eq}}$  are shown. The red dashed line evolves along the tallest bar, showing the coherent oscillation of  $P_n$ . (b) The ratio  $\Gamma_{n \rightarrow n-1} / \Gamma_{n-1 \rightarrow n}$  (red dots) of transition rates are obtained (with errorbar  $\pm\sigma$ ) from  $P_n^{\text{eq}}$ , and compared with the theoretical prediction (black dots). (c) Graph for the thermalization dynamics. Its nodes (circles) represent low-energy eigenstates of the prequench Hamiltonian  $H_0$ , classified by the number  $n$  of spin-up atoms in the states.  $\nu_n$  is the number of the eigenstates having  $n$  spin-up atoms. Each red link connecting two nodes indicates transitions between the corresponding states by  $H_I$ .

distribution. To describe the diffusion, we consider a master equation of the simplest form [140, 153]

$$\begin{aligned} \partial_t P_n(t) = & [P_{n+1}(t)\Gamma_{n+1 \rightarrow n}(t) + P_{n-1}(t)\Gamma_{n-1 \rightarrow n}(t)] \\ & - P_n(t)[\Gamma_{n \rightarrow n-1}(t) + \Gamma_{n \rightarrow n+1}(t)], \end{aligned} \quad (4.6)$$

where  $\Gamma_{n \rightarrow n \pm 1}(t)$  is the rate of transition from states with  $n$  spin-up atoms to those with  $n \pm 1$ . The other transitions of  $n \leftrightarrow n' (\neq n \pm 1)$  are negligible in our regime of  $H_0 \gg H_I$ , as they are higher-order processes of multiple spin flips by  $H_I$ .

The principle of the detailed balance,  $[P_{n+1}^{\text{eq}}\Gamma_{n+1 \rightarrow n} + P_{n-1}^{\text{eq}}\Gamma_{n-1 \rightarrow n}] = P_n^{\text{eq}}[\Gamma_{n \rightarrow n-1} + \Gamma_{n \rightarrow n+1}]$  and  $P_1^{\text{eq}}\Gamma_{1 \rightarrow 0} = P_0^{\text{eq}}\Gamma_{0 \rightarrow 1}$ , is obtained from the master equation in the steady state where  $P_n = P_n^{\text{eq}}$  and  $\partial_t P_n(t) = 0$ ; equivalently,  $\Gamma_{n \rightarrow n-1} / \Gamma_{n-1 \rightarrow n} = P_{n-1}^{\text{eq}} / P_n^{\text{eq}}$ . We obtain  $P_n^{\text{eq}}$  by the time average of  $P_n(t)$  at  $t \geq t_{\text{relax}}$ , and retrieve the microscopic information of  $\Gamma_{n \rightarrow n-1} / \Gamma_{n-1 \rightarrow n}$ , using the detailed balance relation. In Fig. 4.11, the results agree with the theoretical prediction [153, 158] of  $P_n^{\text{eq}} = \nu_n / D$  and  $\Gamma_{n \rightarrow n-1} / \Gamma_{n-1 \rightarrow n} = \nu_{n-1} / \nu_n$  obtained in the limit of  $H_I / H_0 \rightarrow 0$ , where  $\nu_n = \binom{N+1-n}{n}$  for the linear chain,  $\nu_n = \binom{N+2-2n}{n}$  for  $\theta = 60^\circ$ , and  $D = \sum_n \nu_n$  [158].

We explain the meaning of  $\nu_n$  for the linear chains as an example. In our relaxation dynamics,  $H_0 \gg H_I$  and the initial state is the ground state  $|\downarrow_1 \downarrow_2 \cdots \downarrow_N\rangle$  of  $H_0$ . In this case, it is enough to consider only low-energy eigenstates  $|\sigma_z^{(1)} \sigma_z^{(2)} \cdots \sigma_z^{(N)}\rangle$  of the prequench Hamiltonian  $H_0$ , from  $|\downarrow_1 \downarrow_2 \downarrow_3 \cdots\rangle$  to  $|\uparrow_1 \downarrow_2 \uparrow_3 \cdots\rangle$ , in which any two neighboring spins  $\sigma_z^{(i)}$  and  $\sigma_z^{(i+1)}$  cannot be simultaneously in spin up; the other higher-energy eigenstates can be ignored, since they are separated from the low-energy states in energy at least by  $V_{i,i+1}$ . Then,  $P_n(t)$  almost equals the probability of occupying the low-energy states of  $n$  spin-up atoms, and the possible values of  $n$  are  $0, 1, \dots, n_{\text{max}} = N/2$  for even  $N$  and  $0, 1, \dots, n_{\text{max}} = (N+1)/2$  for odd  $N$ .  $\nu_n$  is the number of the low-energy states of  $n$  spin-up atoms. Transitions between those of  $n$  and those of  $n \pm 1$ , occurring with a single spin flip by  $H_I$ , govern the relaxation dynamics in our regime of  $H_0 \gg H_I$  as in Fig. 4.11(c). In this case, the ratio  $\Gamma_{n \rightarrow n-1} / \Gamma_{n-1 \rightarrow n}$  of the transition rates

equals the ratio  $\nu_{n-1}/\nu_n$ . We emphasize that the ratios, microscopic information of the dynamics, are measured in our experiments.

The master equation in Eq. (4.6) efficiently describes the relaxation dynamics, as it has only  $2n_{\max}$  parameters of the transition rates  $\Gamma_{n \rightarrow n \pm 1}$ , which is much smaller than the size  $2^N$  of the Hilbert space. This allows us to experimentally construct the master equation. Among the  $2n_{\max}$  parameters,  $n_{\max}$  parameters are determined by the ratios  $\Gamma_{n \rightarrow n-1}/\Gamma_{n-1 \rightarrow n}$  measured applying the detailed balance. The other  $n_{\max}$  parameters are determined by using the probabilities  $P_n(t)$  and their derivatives  $\partial_t P_n(t)$  measured at the early stage of  $t \simeq 0$  before the coherent oscillations occur (see Supplements). In this step, we use the form of  $\Gamma_{n \rightarrow n \pm 1}(t) = 2\Omega^2 t T_{n \rightarrow n \pm 1}$  derived in Ref. [153], where  $T_{n \rightarrow n \pm 1}$ 's are time independent. Using the experimentally constructed master equation, we compute the time evolution of Rydberg fraction  $f_R(t)$  ( $= \sum_n n P_n(t)/N$ ) and  $\sum_{i,j} \langle \hat{n}_i \hat{n}_j \rangle(t)/N^2$  ( $= \sum_n n^2 P_n(t)/N^2$ ) and find that the result well describes the experimental data of the relaxation of  $f_R(t)$  in Fig. 4.10 (see also Fig. 4.18(a) in Supplements). Note that the master equation result does not show the coherent oscillations, since the higher-energy eigenstates and the processes of multiple spin flips are ignored in the master equation. All the observations imply that the thermalization dynamics obeys the master equation, similarly to dynamics to equilibrium in statistical mechanics.

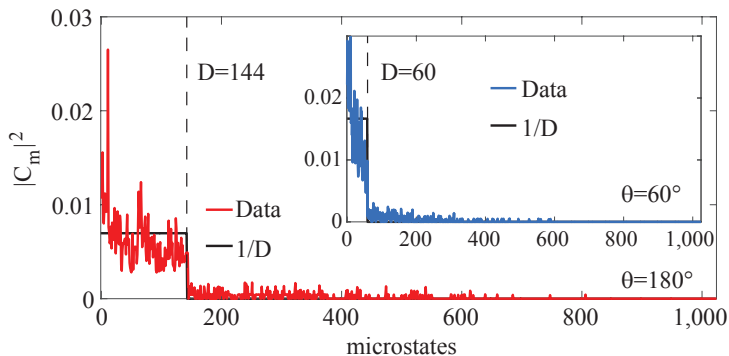


Figure 4.12: **Diffusion over prequench states.** Time average ( $t \geq t_{\text{relax}}$ ) of the measured probability  $|C_m|^2$  of occupying the  $m$ -th eigenstates of the prequench Hamiltonian  $H_0$  for the linear chain of  $N = 10$ . The position of the  $D$ -th eigenstate is indicated by the dashed line. Inset: The same for the  $\theta = 60^\circ$  zigzag chain of  $N = 10$ .

### Stead state

The thermalization dynamics can be considered as diffusion on the graph in Fig. 4.11(c), where each link has equal transition probability determined by  $H_I$ . This indicates that the relaxation time  $t_{\text{relax}}$  depends on the initial point of the diffusion [153, 158]. The initial state  $|\downarrow_1 \downarrow_2 \cdots \downarrow_N\rangle$  of this experiment is located at an edge of the graph. Hence the dynamics has a long relaxation time  $t_{\text{relax}}$  as in Figs. 4.10 and 4.11(a). When an initial state is located closer to the center of the graph, the resulting coherent oscillations become more rapidly suppressed with shorter  $t_{\text{relax}}$  [153].

We experimentally measured the steady-state values of the probability  $|C_m|^2$  with which the chain occupied the  $m$ -th eigenstate of the prequench Hamiltonian  $H_0$ . In the language of the diffusion on the graph,  $|C_m|^2$  is interpreted as the occupation probability of the node corresponding to the  $m$ -th eigenstate. As shown in Fig. 4.12, the result is  $|C_m|^2 \simeq 1/D$ , where  $D = \sum_n \nu_n$  is the total number

of the low-energy eigenstates. This demonstrates almost uniform spreading over the graph, namely over the low-energy eigenstates. Indeed, the experimental data of  $P_n^{\text{eq}}$  are close to  $\nu_n/D$ .

In Fig. 4.13, the experimental results of the steady-state values of the Rydberg fraction  $f_R$  are shown for  $N = 3 - 25$ . They agree with the computation based on the MPS. They are however slightly different from the ETH prediction. Indeed, the typical features of the ETH do not hold in our cases (see Supplements).

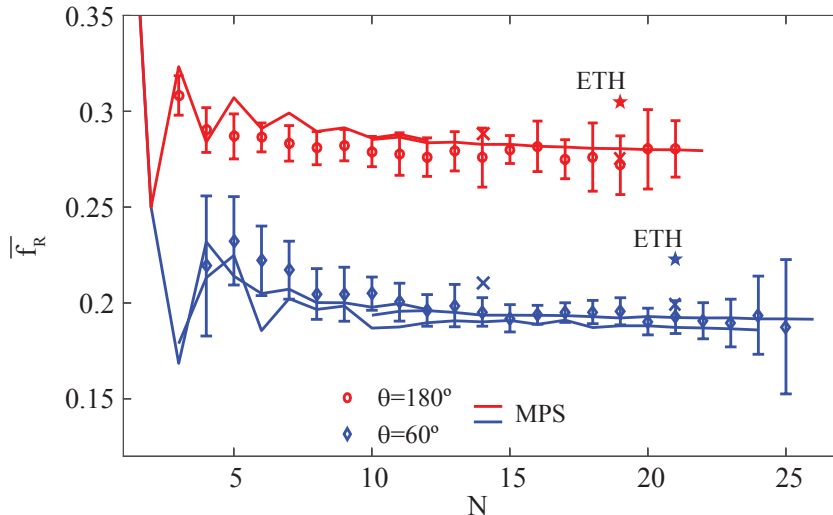


Figure 4.13: **Thermalization value.** Time average  $\bar{f}_R$  of measured Rydberg fraction as a function of system size  $N$  for the linear chain (red circles) and the zigzag chain of  $\theta = 60^\circ$  (blue diamonds). The errorbars of  $\pm\sigma$  are shown. For comparison, the MPS result (solid lines) and the ETH prediction (at  $N = 19$  for the linear chain and at  $N = 21$  for the zigzag chain; color stars) are shown.

## Conclusion

In summary, we performed a quantum simulation experiment with tunable tweezer traps and Rydberg atom interaction. Our quantum simulator provides an ideal test bed for studying quantum coherent evolution of a many-body system after a quench. It allows to simulate a one-dimensional or two-dimensional lattice of Ising-like spin-1/2 particles or the Hamiltonian in Eq. (4.5) with parameters tunable in a wide range. We can monitor the time evolution by measuring occupation probabilities of the eigenstates of a prequench Hamiltonian or a postquench Hamiltonian. The thermalization dynamics studied in our experiment belongs to the cases where the postquench Hamiltonian is slightly modified after quench so that  $H_0 \gg H_I$ . Our results suggest that the detailed balance can be an underlying principle of the thermalization dynamics of the cases. The thermalization dynamics can be efficiently described by the diffusion governed by a master equation of a simple form, similarly to relaxation towards equilibrium in classical statistical mechanics but without its underlying assumptions of coupling to baths and the ergodicity hypothesis based on randomness.

### 4.3.2 Supplements

Professor H.-S Sim and Doctor Yeje Park supported this section with enormous amount of theoretical calculation and fruitful discussion. I would like to appreciate for it.

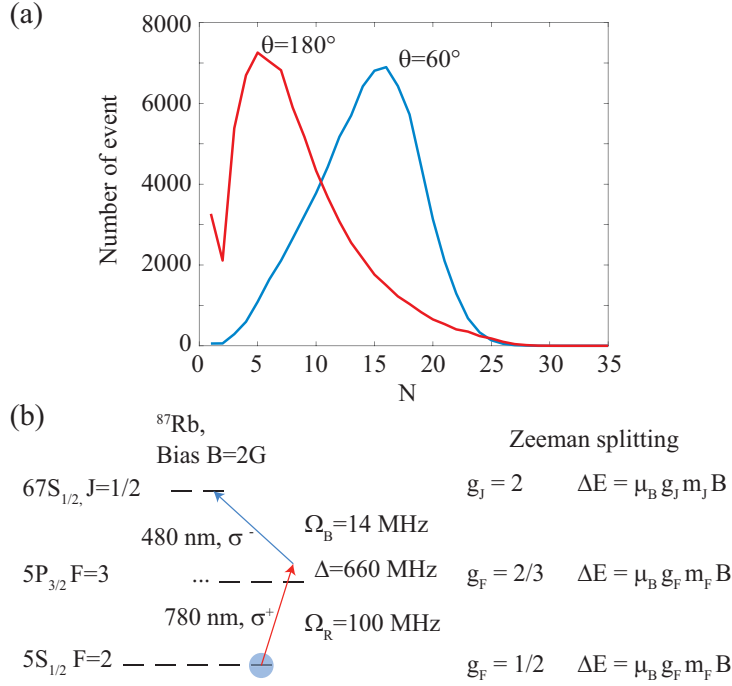


Figure 4.14: (a) Defect-free atom loading spectra, resulting from two-time of feed-back of total 35 sites, for  $\theta = 180^\circ$  (red) and  $60^\circ$  (blue), respectively. (b) Graphical representation of our Rydberg excitation scheme with Rabi frequency and detuning ( $1/2\pi$  scaled). The Rydberg hyper-fine splitting is sub-kHz order thus treated in a reduced form. Zeeman splittings of individual states are shown as well, where the two-level scheme ( $|5S_{1/2}, F = 2, m_F = 2\rangle$  and  $|67S_{1/2}, J = 1/2, m_J = 1/2\rangle$ ) is robust against magnetic field fluctuation.

## Experimental details

Our Rydberg atom system was composed of  $^{87}\text{Rb}$  single-atom tweezer traps synthesized by dynamic phase holograms [43, 110]. As shown in Fig. 3.4, an 820 nm dipole-trap laser of gaussian beam shape was incident on the SLM. Then the laser was phase-modulated by a computer-generated hologram and transferred to the vacuum chamber to form an equally spaced zigzag chain of strongly focused gaussian beams of waist  $w_0 = 1 \mu\text{m}$ , lattice constant  $d = 3.8 - 4.2 \mu\text{m}$ , and bending angle  $\theta$ . Inside the chamber, a 3D magneto-optical trap (MOT) was overlapped with the traps to form a partially filled ( $p \approx 0.5$ ) single-atom array of 80  $\mu\text{K}$  temperature. Then a camera took an image of the initial single-atom loading by collecting scattered photons from the same MOT beams for 40 ms. The result was fed back to the tweezer traps to form a defect-free single-atom array by atom shuttling [43, 110, 105, 104]. The result was then measured and fed back once again for more successful array preparation. The final result showed defect-free array spectrum spanning wide range of atom numbers as shown in the Fig. 4.14(a).

The initialized array was collectively and resonantly driven to Rydberg state  $|67_{1/2}, J = 1/2, m_J = 1/2\rangle \equiv |\uparrow\rangle$  by using the release and recapture (R&R) protocol and the counter-propagating two-pulses ( $\sigma^+$  780 nm and  $\sigma^-$  480 nm) scheme, as shown in Fig. 4.14(b) [126, 135, 44, 106, 107]. First, the bias B-field of 2 G was turned on and waited 50 ms for eddy current decay from nearby metals, and the dipole-trap beam power was adiabatically reduced to 1/3 to mitigate AC stark shift. Then, the entire array was optically pumped to the ground state  $|5S_{1/2}, F = 2, m_F = 2\rangle \equiv |\downarrow\rangle$  by using  $\sigma^+$  transition of  $|5S_{1/2}, F = 2\rangle \rightarrow |5P_{3/2}, F' = 2\rangle$  for 500  $\mu\text{s}$  while the repump was kept low. After driving the system

with R&R protocol, the dipole trap beam power was adiabatically recovered, the bias B-field was turned off, and waited for 50 ms again. Then the final single-atom image was captured for the site-resolved number state measurement, e.g.  $\hat{n} |\downarrow\uparrow\rangle = 01 |\downarrow\uparrow\rangle$ . The overall sequence repeated indefinitely at 0.6 Hz rate.

We used external-cavity diode lasers (780 nm and 480 nm) for Rydberg state excitation. The laser frequencies were locked to an ultra-low-expansion (ULE) cavity (Stable Laser Systems, ATF-6010-4), The long-term temperature drift of the cavity was kept within 10 mK, resulting in absolute frequency drift below 1 kHz on both lasers. The achieved linewidths were estimated to below 10 kHz. The intermediate level detuning from  $5S_{1/2}, F = 2$  to  $5P_{3/2}, F = 3$  was  $\Delta_I = 2\pi \times 660$  MHz. The 780 nm Rabi frequency,  $\Omega_{780} = 2\pi \times 100$  MHz, was calibrated by Stark shift measurement [139]. Then, the 480 nm Rabi frequency,  $\Omega_{480} = 2\pi \times 14$  MHz, was deduced by two-photon Rabi frequency,  $\Omega_{780}\Omega_{480}/2\Delta_I = 2\pi \times 1$  MHz.

The ULE cavity was cylinder shaped and of dual-wavelength, 15,000 finesse, and 1.5 GHz comb spacing. The cavity housing (Stable Laser Systems, VH6010-4) was kept in ultra low vacuum condition ( $< 10^{-7}$  Torr) and locked to precisely measured zero-crossing temperature of the cavity.

The beam diameters ( $1/e^2$ ) at the single-atom array were  $80 \mu\text{m}$ ,  $10 \mu\text{m}$  for 780 nm, and 480 nm lasers, respectively. The available 480 nm power was limited to 10 mW. Two lasers were counter-propagating and the array was elongated along the propagation axis to achieve homogeneous interaction within 5% for the 1D array.

The details are as follows: Finishing the optical pumping, 480 nm Rydberg laser was turned on for  $10 \mu\text{s}$  fixed duration. After  $3 \mu\text{s}$  later, the dipole-trap beam was completely turned off for  $3.8 \mu\text{s}$  fixed duration which was the release process in the protocol so that Rydberg levels were intact from the energy shift that was detrimental for reliable experiments. During the release period, the 780 nm Rydberg laser was switched on for  $0\text{-}3 \mu\text{s}$  variable time with 100 ns step so that the Rydberg pulse length was precisely controlled. After the release period, the dipole-trap beam was turned on again for recapture process. The recapture process was state-selective detection between  $|\downarrow\rangle$  and  $|\uparrow\rangle$  because the dipole trap exerted repulsive force on  $|\uparrow\rangle$  and rapidly kicked out the atom while  $|\downarrow\rangle$  was recaptured again.

Switching of the three lasers (480 nm, 820 nm trap, and 780 nm) were performed with acousto-optic modulators (AOMs). Their rise/fall times were 50 ns, 100 ns, and 20 ns, respectively. All the switching speed satisfied the sudden quench condition we have discussed. The master triggers were generated by a computer controlled data acquisition board (NI, PCIe-6353), and more precise pulse width control was done by using delay generator (SRS, DG-535). The pulse time jitters and shot-to-shot power fluctuations were less than 10 ns and 2% (780 nm), 4% (480 nm), respectively, measured by using fast photo-detectors.

The Rydberg resonance was roughly found by using a wavelength meter (HighFinesse, WS7) and quantum defect theory [136]. Then frequency of the 780 nm was scanned to find the exact resonance. The details were as follows: The cavity part of the 780 nm laser was phase modulated by a fiber electro-optic modulator (EOM) and the first order sideband was locked to a cavity comb. By tuning the sideband frequency, the 780 nm laser spanned the entire range of comb space to find the exact Rydberg resonance line. The RF signals for every EOMs and AOMs were phase locked to a commercial 10 MHz reference clock (SRS, FS725).

The van der Waals coefficient for  $^{87}\text{Rb } 67S_{1/2}$  state was  $C_6 = -470 \text{ GHz } \mu\text{m}^6$  calculated by direct diagonalization [129]. The blockade radius was  $r_B \equiv (|C_6|/\Omega)^{1/6} = 6.6 \mu\text{m}$ , chosen between  $d$  and  $2d$ . Thus the system was well approximated by the nearest neighbor (NN) interacting spin model, and the next nearest neighbor (NNN) interaction was controlled by tuning the angle. As a result, Rydberg crystals for  $N = 11$ , NN and  $N = 16$ , NNN regimes are clearly observed of probabilities 0.005 and

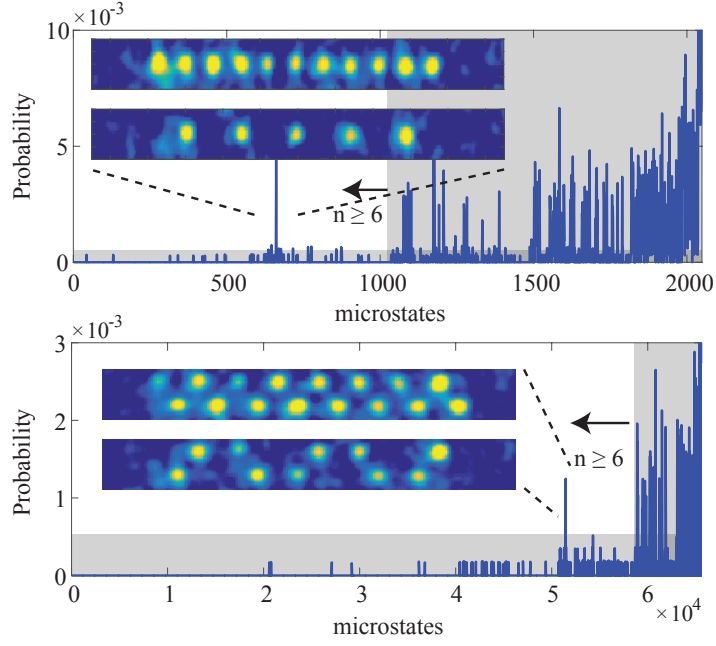


Figure 4.15: Every microstate probability for  $N = 11$ ,  $\theta = \pi$ , and  $N = 16$ ,  $\theta = 78^\circ$ . The  $x$ -axis is decreasing order of  $n$ . The false-positive detection errors (horizontal shaded areas) are sufficiently low. (Inset) Typical images before and after Rydberg excitation for  $N = 11$ , and 16 chains. The bright (empty) sites correspond to the  $|\downarrow\rangle$  ( $|\uparrow\rangle$ ) (see text), clearly show Rydberg crystals. The images are re-scaled and Gaussian filtered for clarity.

0.001, respectively in Fig. 4.15. For robust crystal formation, dynamic crystallization method, utilizing adiabatic sweep of Hamiltonian, has been demonstrated [135, 106].

### Error estimation

Simulated quantum process tomography [159, 160] is a viable option for error estimation in our experiment. The strategy is as follows; We utilized a priori information about the level scheme and fluctuation of the coupling in Fig. 4.14(b) for reconstructing time-trace of single atom Rabi oscillation. Spontaneous decay and laser linewidth were treated by solving Lindblad equation.  $\Omega$  and  $\Delta$  fluctuations were treated by Monte-Carlo method where they are assumed to be decoupled and shot-to-shot of Lorentzian form,  $P(\Omega) \propto 1/(1 + (\Omega - \Omega_0)^2/\delta\Omega^2)$  and  $P(\Delta) \propto 1/(1 + (\Delta - \Delta_0)^2/\delta\Delta^2)$ . The free parameters were estimated by minimizing a maximum-likelihood estimation with the experimental data in Fig. 4.16(a), where  $\Omega_0 = 1.04$  MHz,  $\delta\Omega = 0.08$  MHz,  $\Delta_0 = 0$ , and  $\delta\Delta = 0.1$  MHz, respectively. Furthermore, we extended the procedures from the single atom result to up to 3 atoms collective Rabi oscillation as shown in Fig. 4.16(b, c). The Rabi oscillations effectively fitted with exponential decay. Their decay constants were all equal which confirmed that collective dephasing was the most dominant error. By quantitatively analysing the known error sources in table. 4.2 and 4.3, we could confirm that more than 80 % of the Rabi oscillation decay in our experiment was due to inhomogeneous dephasing from slow environmental fluctuations such as beam power, stray electric field, and beam pointing fluctuation.

From here, further details of the above analysis and the way of application for  $N = 10$  are described.

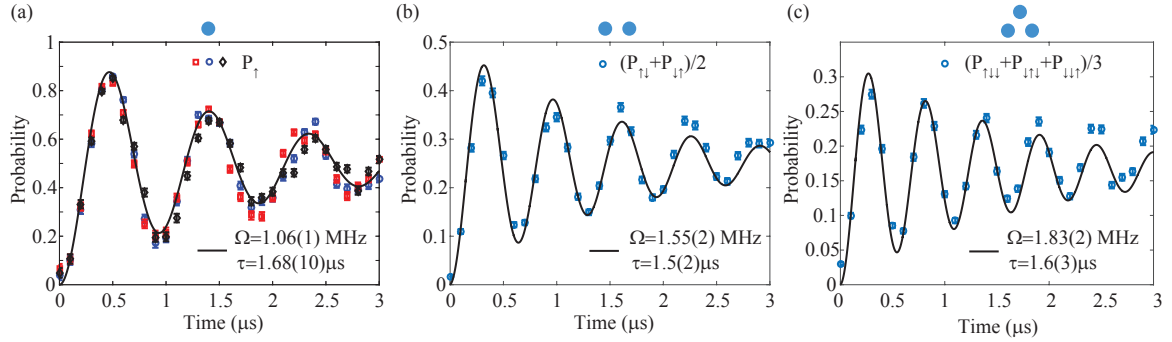


Figure 4.16: **Rydberg fraction dynamics** (a-c) N=1-3 atoms dynamics of collective Rydberg Rabi oscillation. The points are experimental data of W-states and the solid lines are best fits of  $\{1 - \cos(\Omega t) \exp(-t/\tau)\}/2N$ . (a) The color points are data from different positions,  $4.4 \mu\text{m}$  apart.

table 4.2: Individual dephasing sources.

Error sources	Effective Rabi decay $\tau$	Treatment
5P <sub>3/2</sub> decay, 26 ns		Two-level approximation and Lindblad operator, see text
67S <sub>1/2</sub> decay, 100 $\mu\text{s}$ , Ref. [127]	$\simeq 15.5 \mu\text{s}$	$L_i = \sqrt{\gamma/2}\sigma_z^i$ , where $\gamma = 2\pi \times 20 \text{ kHz}$
$\Omega_1, \Omega_2$ imbalance		Neglected for simulation simplicity,
5P <sub>3/2</sub> geometric phase	$> 50 \mu\text{s}$	$ \downarrow\rangle \rightarrow e^{i\delta t}  \downarrow\rangle,  \uparrow\rangle \rightarrow e^{-i\delta t}  \uparrow\rangle$ , where $\delta = 2\pi \times 5 \text{ kHz}$
Atomic thermal motion	$\delta\Omega < 0.01\Omega$ $\delta V \sim 0.5V$	Monte-Carlo method
(80 $\mu\text{K}$ ), Ref. [139]	Doppler shift	$\simeq 100 \mu\text{s}$ Neglected for simulation simplicity

table 4.3: Collective dephasing sources.

Error sources	Effective Rabi decay $\tau$	Treatment
Rydberg Lasers linewidth, $\leq 10$ kHz	$\geq 20 \mu\text{s}$	$L = \sum_i \sqrt{\gamma/2}\sigma_z^i$ , where $\gamma \leq 2\pi \times 16$ kHz
480 nm and dipole trap beam pointing fluctuation	$\delta\Omega \sim 0.05\Omega$ , $\delta\Delta \sim 2\pi \times 10$ kHz	Monte-Carlo method, or effective $L = \sum_i \sqrt{\gamma/2}\sigma_z^i$ , in Fig. 4.16(b, c) where $\gamma = 2\pi \times 160$ kHz
Intensity fluctuation, 4% (480), 2% (780)	$\delta\Omega \sim 0.03\Omega$ , $\delta\Delta \sim 2\pi \times 40$ kHz	
Static electric field fluctuation	$\delta\Delta \sim 2\pi \times 50$ kHz	

First, Lindblad equation [161, 162] is briefly introduced,

$$\frac{d}{dt}\rho = -\frac{i}{\hbar}[\hat{H}, \rho] + \mathcal{L}(\rho), \quad (4.7)$$

where  $\mathcal{L}(\rho)$  is Lindblad super-operator,

$$\mathcal{L}(\rho) = \sum_n L_n \rho L_n^\dagger - (L_n^\dagger L_n \rho + \rho L_n^\dagger L_n)/2, \quad (4.8)$$

where  $L_n$  is called Lindbladian. The equation describes open quantum system factorable to the environment, which is trace preserving and appropriate for dealing with a quantum system in the presence of depopulation or dephasing. The property naturally suits to our experimental condition, post-selective analysis. The representative example is a quantum system in the presence of depopulation or dephasing; two-level system with spontaneous decay from the upper level is described by Lindbladian,  $L = \begin{pmatrix} 0 & 0 \\ \sqrt{\Gamma} & 0 \end{pmatrix}$  and the famous form of super-operator  $\mathcal{L}(\rho) = \begin{pmatrix} -\Gamma\rho_{11} & -\Gamma\rho_{12}/2 \\ -\Gamma\rho_{21}/2 & \Gamma\rho_{11} \end{pmatrix}$  in the optical Bloch equation is acquired. In the case of dephasing,  $L = \sqrt{\gamma/2}\hat{\sigma}_z$  and  $\mathcal{L}(\rho) = \begin{pmatrix} 0 & -\gamma\rho_{12} \\ -\gamma\rho_{21} & 0 \end{pmatrix}$  are given, respectively.

Remind that our level scheme is originally multi-level and reduced to two-level by adiabatic elimination as shown in Fig 4.14(b). We claim that the two-level approximation is still valid for Lindblad formalism in our experiment, so that Lindblad equation up to  $N=10$  can be treated. The leakage to intermediate level during two-photon Rabi oscillation has negligible amount ( $< 0.003$ ) and its geometric phase is sufficiently small as shown in table. 4.2. However, even such small leakage causes decaying Rabi oscillation on the reduced two-level because spontaneous decay rate of  $5P_{3/2}$  is relatively high compared to Rabi frequency. We numerically found that the decaying Rabi oscillation was exactly fitted with exponential curve, and confirmed that the decay can be effectively reduced to two-level dephasing. The result holds for laser linewidth (except it adds up collectively) as well, and the quantities are summarized in table. 4.2 and 4.3.

Then, many-body Lindblad equation could be constructed by direct product of the single atom result, and a priori  $\Omega$  and  $\Delta$  shot-to-shot fluctuation was included by Monte-Carlo realization. The numerical results were shown in Fig. 4.17. Interaction fluctuation,  $\delta V$ , should be accounted as well for investigating the experimental errors of many-body system. Atomic thermal motion induces such fluctuation during the release period; Initially fixed single-atom within 200 nm radius starts to move by having a different velocity on each realization of experiment, where the velocity follows Boltzmann distribution. From the 4  $\mu\text{m}$  period of atom array, the position fluctuation is realized by Monte-Carlo method accounting 3D atomic thermal motion of 80  $\mu\text{K}$  temperature. As a result, the inter-atomic distance has gaussian distribution of  $\sigma = 0.2$  nm at 1.5  $\mu\text{s}$ , and the time-traces of Rydberg fraction

table 4.4: Projection measurement error sources.

Error sources		$\langle \hat{n} \rangle$ error
Detection errors, see text	False-positivie	$0.024(1-\langle \hat{n} \rangle)$
	False-negative	$0.015\langle \hat{n} \rangle$
Optical pumping		0.01
Atom image projection		$\ll 0.001$
Background gas collision		$e^{-0.15/30} = 0.005$
Leakage to the other Rydberg levels [159]		$<0.001$
Leakage to another ground level		$\simeq 0.003$
Leakage to intermediate level		$<0.003$

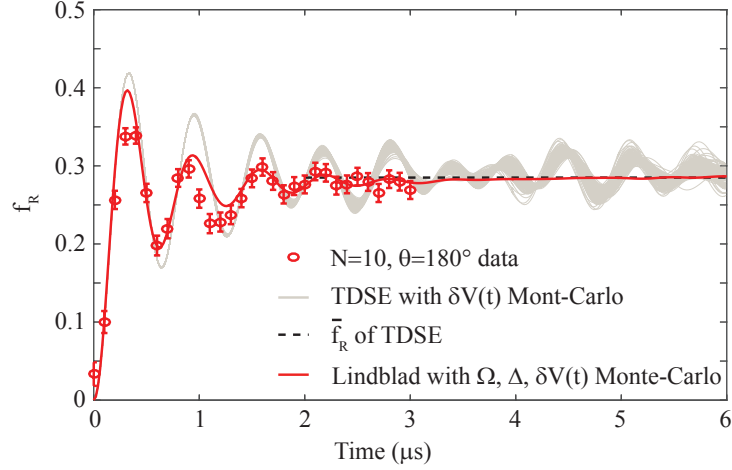


Figure 4.17:  $N=10$ ,  $\theta = 180^\circ$  Rydberg fraction dynamics. Gray lines are Time-domain Schrödinger equation (TDSE) results of 200 Monte-Carlo events.  $\delta V(t)$  was estimated by considering 3D atomic thermal motion. Black dashed line is the result of long-time average of Rydberg fraction in TDSE result. Red line is the result of Lindblad equation of 100 Monte-Carlo events.

of 100 hundred realization are shown in Fig. 4.17. The effect becomes larger as time goes by, yet it is relatively small and neglected within  $3 \mu\text{s}$  of our experimental time. Although the experimental errors are all considered carefully, it does not affect the steady state even in longer period of time. The  $\delta V$  fluctuation manipulates only oscillation phases, and both intrinsic and inhomogeneous dephasing suppress oscillation amplitude. Those arguments and observations support the robustness of our claim for equilibration physics in perturbative regime,  $H_0 \gg H_I$ , even in the existence of experimental errors.

### Supporting experimental data: Thermalization

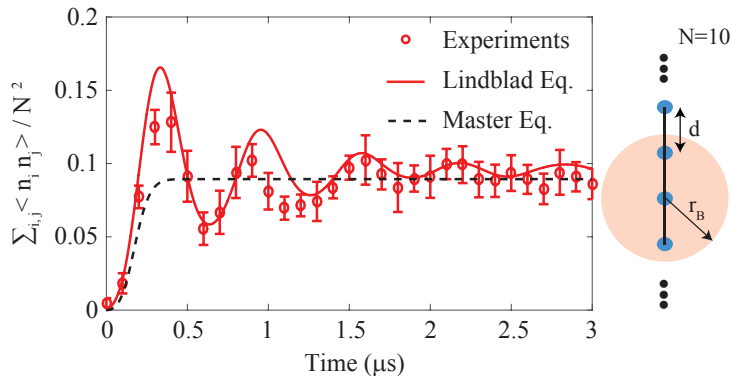


Figure 4.18: Time dependence of  $\sum_{i,j} \langle \hat{n}_i \hat{n}_j \rangle(t) / N^2$  measured for the linear chain of  $N = 10$ . The experimental data (circles) are compared with the computation (solid lines) based on the Lindblad equation and also with the result (dashed) of the master equation constructed based on the experimental data. The errorbars are standard error of the mean.

In the main text, we have shown the experimental data of the Rydberg fraction  $f_R$ . Here we show the data of another observable of  $\sum_{i,j} \langle \hat{n}_i \hat{n}_j \rangle(t) / N^2$ . We plot the quench dynamics of  $\sum_{i,j} \langle \hat{n}_i \hat{n}_j \rangle(t) / N^2$  in Fig. 4.18. Similarly to the dynamics of  $f_R$  in Fig. 3.1, the experimental data agree with the calculation based on the Lindblad equation and also with the master equation constructed from our experimental data. This supports that our system is described by the Hamiltonian  $H$ . We also plot the steady-state value of  $\sum_{i,j} \langle \hat{n}_i \hat{n}_j \rangle(t) / N^2$  in Fig. 4.19. The experimental results agree with the MPS calculation.

### Critical exponent

For 1D case, the ratio between mean interaction energy  $V_m = |C_6| n_{eff}^6$  and Rabi frequency  $\hbar\Omega$  is introduced as a dimensionless quantity,

$$\alpha = \frac{\hbar\Omega}{|C_6| n_{eff}^6} \quad (4.9)$$

where  $n_{eff}$  is effective 1D density for zigzag chain to be defined. The long-time average of Rydberg fraction  $\bar{f}_R$ , then follows the scaling behavior [126, 156]

$$\bar{f}_R \sim \alpha^\nu \quad (4.10)$$

where  $\nu = 2/13 = 0.153$  for 1D case.

The zigzag chain has a constant lattice distance  $d$  and tunable bending angle  $\theta$ . It is effectively described by 1D system since  $d < r_B$  holds. For defining  $n_{eff}(\theta)$ , two density  $n_{\parallel} \equiv (d \sin \theta/2)^{-1}$  and  $n_{\perp} \equiv (d \cos \theta/2)^{-1}$  are defined. For  $\theta \rightarrow 180^\circ$ ,  $n_{eff}(\theta) = n_{\parallel}$  is straightforward. For  $\theta \rightarrow 0$ , we can define  $n_{eff}(\theta) = n_{\parallel}/2$  because the system becomes two independent linear chain of lattice distance  $2d \sin \theta/2$ .

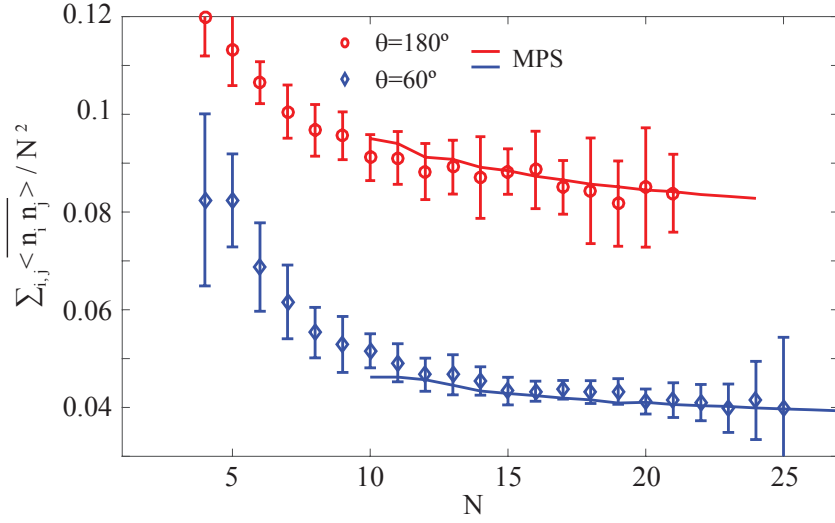


Figure 4.19: Time average of  $\sum_{i,j} \langle \hat{n}_i \hat{n}_j \rangle(t) / N^2$  at  $t \geq t_{\text{relax}}$  as a function of system size  $N$  for the linear chain (red circles) and the zigzag chain of  $\theta = 60^\circ$  (blue diamonds). The errorbars of  $\pm\sigma$  are shown. The theoretical results (solid lines) based on MPS are also shown.

In between those two limits,  $n_\perp$  should contribute on the density but the exact formula is unknown. Here, we used  $n_{\text{eff}}(\theta) \equiv n_\parallel/2 + \min(n_\parallel/2, n_\perp)$  which is one of the simplest approximation satisfying continuity. The  $\alpha$  for extracting 1D critical exponent includes a strong rectifier of sixth-power to  $n_{\text{eff}}$ , so we assume that any density errors caused by the approximation would be reduced. As a result, the critical exponent in Fig. 4.20 shows good agreement with the mean-field theory prediction, supporting our argument that the equilibration behavior in the experiment is generic.

### The master equation from the experimental data

For the case of  $N=10$  and  $\theta = 180^\circ$ , the master equation is written by  $\dot{\mathbf{P}} = M(t)\mathbf{P}$  [153], where  $\mathbf{P}$  is  $P_n$  vector for  $n=0-5$ , and  $M(t)$  is given by Eq. (4.6). The number of total unknown of  $M(t)$  is 10. Among them, five equalities are acquired by the detailed balance of the data, and the other five are acquired by the early time data  $\dot{P}_n(t_i) = M(t_i)P_n(t_i)$ , where  $\dot{P}_n(t_i) = (P_n(t_{i+1}) - P_n(t_{i-1})) / 2dt$  for  $i = 1, 2$ . Note that  $t_i = (i - 1) \times 100$  ns in the experiment. For the details, we explicitly write down the detailed balance and transition matrix,

$$\begin{bmatrix} P_0^{\text{eq}} \\ P_1^{\text{eq}} \\ P_2^{\text{eq}} \\ P_3^{\text{eq}} \\ P_4^{\text{eq}} \\ P_5^{\text{eq}} \end{bmatrix} = \begin{bmatrix} 0.0221 (0.0098) \\ 0.1024 (0.0221) \\ 0.2689 (0.0334) \\ 0.3393 (0.0489) \\ 0.2097 (0.0424) \\ 0.0521 (0.0164) \end{bmatrix} \quad (4.11)$$

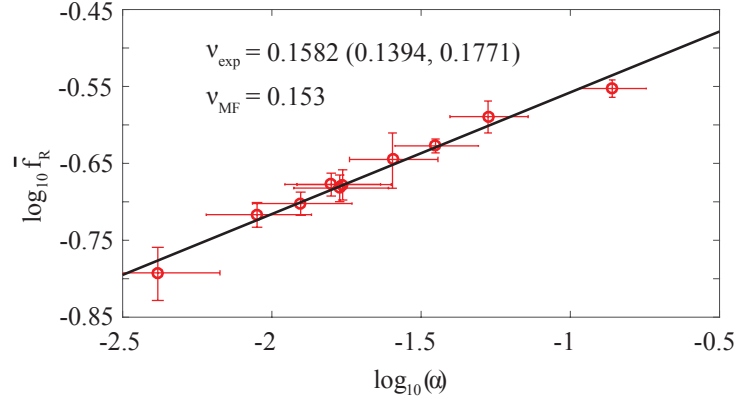


Figure 4.20: Critical behavior of Rydberg fraction,  $\bar{f}_R \sim \alpha^\nu$ , after reaching to the equilibrium as a function of  $\alpha \equiv \hbar\Omega/|C_6|n_{eff}^6$ , where  $n_{eff}$  is effective density of zigzag chain (see text). The experimentally measured critical exponent  $\nu_{exp}$  is estimated with 95 % confidence interval of least-square fit. The y-axis, and x-axis errorbars are standard deviation of  $\bar{f}_R$ , and fixed 200 nm distance error, respectively.  $N=15$  for all data.

$$M(t) = 2\Omega^2 t \begin{bmatrix} -T_{0 \rightarrow 1} & T_{1 \rightarrow 0} & 0 & 0 & 0 & 0 \\ T_{0 \rightarrow 1} & -T_{1 \rightarrow 0} - T_{1 \rightarrow 2} & T_{2 \rightarrow 1} & 0 & 0 & 0 \\ 0 & T_{1 \rightarrow 2} & -T_{2 \rightarrow 1} - T_{2 \rightarrow 3} & T_{3 \rightarrow 2} & 0 & 0 \\ 0 & 0 & T_{2 \rightarrow 3} & -T_{3 \rightarrow 2} - T_{3 \rightarrow 4} & T_{4 \rightarrow 3} & 0 \\ 0 & 0 & 0 & T_{3 \rightarrow 4} & -T_{4 \rightarrow 3} - T_{4 \rightarrow 5} & T_{5 \rightarrow 4} \\ 0 & 0 & 0 & 0 & T_{4 \rightarrow 5} & -T_{5 \rightarrow 4} \end{bmatrix} \quad (4.12)$$

By imposing the detailed balance, where  $T_{n+1 \rightarrow n}/T_{n \rightarrow n+1} = P_n^{eq}/P_{n+1}^{eq}$ , we reduce the unknown from 10 to 5,

$$M(t) = 2\Omega^2 t \begin{bmatrix} -T_{0 \rightarrow 1} & T_{0 \rightarrow 1} \frac{P_0^{eq}}{P_1^{eq}} & 0 & 0 & 0 & 0 \\ T_{0 \rightarrow 1} & -T_{0 \rightarrow 1} \frac{P_0^{eq}}{P_1^{eq}} - T_{1 \rightarrow 2} & T_{1 \rightarrow 2} \frac{P_1^{eq}}{P_2^{eq}} & 0 & 0 & 0 \\ 0 & T_{1 \rightarrow 2} & -T_{1 \rightarrow 2} \frac{P_1^{eq}}{P_2^{eq}} - T_{2 \rightarrow 3} & T_{2 \rightarrow 3} \frac{P_2^{eq}}{P_3^{eq}} & 0 & 0 \\ 0 & 0 & T_{2 \rightarrow 3} & -T_{2 \rightarrow 3} \frac{P_2^{eq}}{P_3^{eq}} - T_{3 \rightarrow 4} & T_{3 \rightarrow 4} \frac{P_3^{eq}}{P_4^{eq}} & 0 \\ 0 & 0 & 0 & T_{3 \rightarrow 4} & -T_{3 \rightarrow 4} \frac{P_3^{eq}}{P_4^{eq}} - T_{4 \rightarrow 5} & T_{4 \rightarrow 5} \frac{P_4^{eq}}{P_5^{eq}} \\ 0 & 0 & 0 & 0 & T_{4 \rightarrow 5} & -T_{4 \rightarrow 5} \frac{P_4^{eq}}{P_5^{eq}} \end{bmatrix} \quad (4.13)$$

From the early-time data,  $P_n(t_{1,2,3})$ , the 6 equations are derived and the remained 5 unknowns are over-determined. Therefore, one of the edge equations,  $\dot{P}_0(t_2) = -T_{0 \rightarrow 1}P_0(t_2) + T_{0 \rightarrow 1}P_0^{eq}/P_1^{eq}P_1(t_2)$  or  $\dot{P}_5(t_2) = T_{4 \rightarrow 5}P_4(t_2) - T_{4 \rightarrow 5}P_4^{eq}/P_5^{eq}P_1(t_2)$ , is discarded and two independent results are acquired as,

$$\begin{bmatrix} T_{0 \rightarrow 1} \\ T_{1 \rightarrow 2} \\ T_{2 \rightarrow 3} \\ T_{3 \rightarrow 4} \\ T_{4 \rightarrow 5} \end{bmatrix} = \begin{bmatrix} 1.644 \\ 1.573 \\ 1.517 \\ 5.123 \\ 1.162 \end{bmatrix}, \begin{bmatrix} 1.612 \\ 1.546 \\ 1.475 \\ 4.732 \\ 0.516 \end{bmatrix} \quad (4.14)$$

which are similar to each other. Then, the time-trace of master equation is calculated by using 4-th order Runge-Kutta method for the initial condition,  $P_0 = 1$ .

## Implementation details of Matrix Product States

We used the matrix product states (MPS) [163] of

$$|\psi\rangle = \sum_{\sigma_z^{(1)}, \dots, \sigma_z^{(L)}} M^{\sigma_z^{(1)}} M^{\sigma_z^{(2)}} \dots M^{\sigma_z^{(L)}} |\sigma_z^{(1)}, \sigma_z^{(2)}, \dots, \sigma_z^{(L)}\rangle. \quad (4.15)$$

Here,  $\sigma_z^{(i)} = 1$  ( $\sigma_z^{(i)} = -1$ ) represents pseudospin  $\uparrow_i$  ( $\downarrow_i$ ).  $\sigma_z^{(i)} = \pm 1$  is related to the occupation number  $n_i$  of the Rydberg state of atom  $i$  through the relation  $\hat{n}_i = (1 + \hat{\sigma}_i^z)/2$ .  $M^{\sigma_z^{(i)}}$  is a  $(\chi_i \times \chi_{i+1})$  matrix for each quantum number  $\sigma_z^{(i)}$ . The integer  $\chi_i$  is called the bond dimension.

The initial state at  $t = 0$  is  $|\psi_0\rangle = |-1, -1, \dots, -1\rangle$ . It is a MPS with bond dimension  $\chi_j = 1$  for all  $j$ . We evolve the initial state using the Hamiltonian

$$H = V_{12} \sum_{i=1}^{N-1} \hat{n}_i \hat{n}_{i+1} + V_{13} \sum_{i=1}^{N-2} \hat{n}_i \hat{n}_{i+2} + \frac{\Omega}{2} \sum_{i=1}^N \hat{\sigma}_x^{(i)},$$

where we choose  $V_{12}/2\pi\hbar = 20$  MHz,  $V_{13} = V_{12}/64$  for  $\theta = 180^\circ$ ,  $V_{13} = V_{12}$  for  $\theta = 60^\circ$ , and  $\Omega/2\pi = 1.0(1)$  MHz. We use the second order Suzuki-Trotter approximation,

$$e^{-iHdt} \approx e^{-ih_x dt/2} e^{-ih_z dt} e^{-ih_x dt/2}, \quad (4.16)$$

where  $h_x$  ( $h_z$ ) is the part of  $H$  containing  $\sigma_x^{(i)}$ 's ( $\sigma_z^{(i)}$ 's). The operator  $h_z$  contains  $\sum_{i=1}^{L-1} \sigma_z^{(i)} \sigma_z^{(i+1)}$  and  $\sum_{i=1}^{L-2} \sigma_z^{(i)} \sigma_z^{(i+2)}$ , and their exponentials can be written as matrix product operators (MPO) using the method described in Ref. [164]. We apply the MPO of  $e^{-iHdt}$  on  $|\psi_0\rangle$ . Because this operation increases bond dimensions, we variationally compress [165, 166] the resulting state. In other words, we approximate the resulting state with another MPS with bond dimensions smaller than some fixed maximum bond dimension  $\chi_{\max}$ . We repeat this process to evolve  $|\psi_0\rangle$  over finite time  $t$ .

There are two sources of error: (1) the time step in Suzuki-Trotter approximation is not infinitesimal and (2) the maximum bond dimension is finite. We verified that the time step smaller than  $\Omega dt = 0.013$  does not change our data much. We increased  $\chi_{\max}$  until our data shows no appreciable dependence on  $\chi_{\max}$ . For example, when  $V_{13} = 0$  and  $N = 23$ , we had  $\chi_{\max} = 240$ . When  $V_{13} = V_{12}$  and  $N = 26$ , we had  $\chi_{\max} = 200$ .

## Invalidity of ETH in our cases

If the eigenstate thermalization hypothesis (ETH) holds for our system, the matrix elements of  $\hat{n}_i$  in the basis of the eigenstates  $|\alpha\rangle$  of  $H$  can be written as [149, 152]

$$n_{\alpha\beta}(E, \omega) \equiv \langle \alpha | \hat{n}_i | \beta \rangle = n(E) \delta_{\alpha\beta} + e^{-S(E)/2} f(E, \omega) R_{\alpha\beta},$$

where  $H|\alpha\rangle = E_\alpha|\alpha\rangle$ ,  $E = (E_\alpha + E_\beta)/2$ , and  $\omega = E_\alpha - E_\beta$ .  $n(E)$  and  $f(E, \omega)$  are smooth functions of  $E$  and  $\omega$ . As our system is time-reversal-symmetric,  $R_{\alpha\beta} = R_{\beta\alpha}$  is real, and  $R_{\alpha\beta}$  is a random variable with zero mean and unit variance.  $S(E)$  is the thermodynamic entropy at  $E$ .

To see whether the above feature is satisfied in our case, we plot the diagonal elements  $n_{\alpha\alpha}(E) = \langle \alpha | \hat{n}_i | \alpha \rangle$  versus  $E = E_\alpha$  for a linear chain in Fig. 4.21 and for a zigzag chain in Fig. 4.22; similar figures have been studied in Ref. [150]. If the ETH is correct,  $n_{\alpha\alpha}(E)$  should be smooth and nearly constant within the energy window  $[-\Delta, \Delta]$  as the initial state  $|\downarrow_1 \downarrow_2 \dots \downarrow_N\rangle$  has the energy expectation value  $\langle H \rangle = 0$  and the energy fluctuation  $\Delta = \sqrt{\langle H^2 \rangle - \langle H \rangle^2} = \Omega\sqrt{N}$ . However,  $n_{\alpha\alpha}(E)$  is not smooth over  $E_\alpha \in [-\Delta, \Delta]$  in our cases shown in Figs. 4.21 and 4.22, demonstrating the violation of the ETH.

Note that we also plot the normalized energy distribution  $\rho(E)$

$$\rho(E) = \sum_{\alpha} |C_{\alpha}|^2 \delta(E - E_{\alpha})$$

in Figs. 4.21 and 4.22, where  $C_{\alpha} = \langle \alpha | \downarrow_1 \downarrow_2 \cdots \downarrow_N \rangle$ . The distribution tells us which energy eigenstates give the most dominant contributions to the eigenstate expansion of  $|\downarrow_1 \downarrow_2 \cdots \downarrow_N\rangle = \sum_{\alpha} C_{\alpha} |\alpha\rangle$ .  $\rho(E)$  is almost a Gaussian with mean 0 and standard deviation  $\Delta$ .

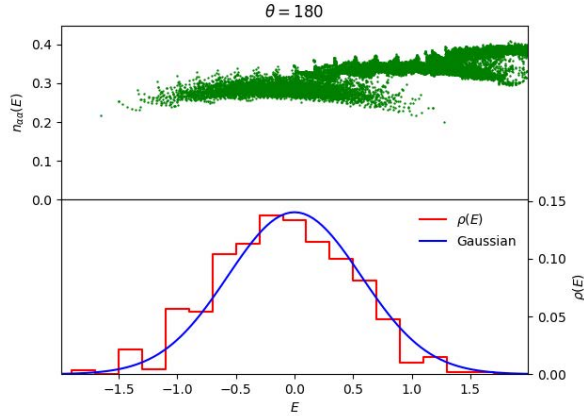


Figure 4.21:  $n_{\alpha\alpha}(E)$  and  $\rho(E)$  for the linear chain with  $N = 19$ . Upper panel: The diagonal element  $n(E)$  is supposed to be a smooth function of  $E$  and constant over energy windows with width  $\Delta$ , according to ETH. However, we see that  $n(E)$  is not smooth.  $\rho(E)$  is plotted after summing delta functions over small energy windows. If the system is quantum chaotic,  $\rho(E)$  is expected to have a Gaussian centered at 0 with standard deviation  $\Delta = 0.57$ .

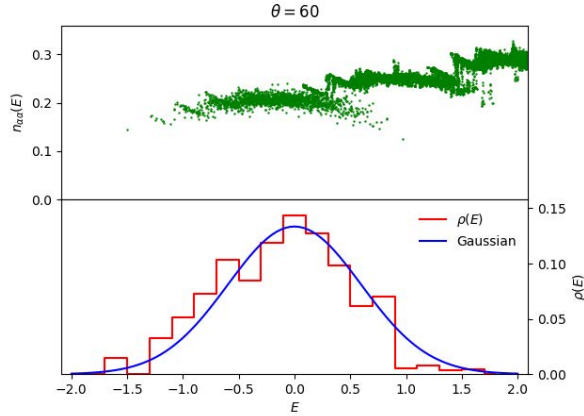


Figure 4.22:  $n_{\alpha\alpha}(E)$  and  $\rho(E)$  for the zigzag chain with  $N = 21$  and  $\theta = 60^\circ$ . The diagonal element  $n(E)$  is supposed to be a smooth function of  $E$  and constant over energy windows with width  $\Delta$ , according to ETH. However, we see that  $n(E)$  is not smooth.  $\rho(E)$  is plotted after summing delta functions over small energy windows. If the system is quantum chaotic,  $\rho(E)$  is expected to have a Gaussian centered at 0 with standard deviation  $\Delta = 0.6$ .

## Chapter 5. Conclusion

In this thesis, real-time transport of single-atom array using holographic tweezers is demonstrated. For this, a liquid-crystal spatial light modulator is used, a computer-generated hologram algorithm (CGHA) is devised based on Gerchberg-Saxton algorithm, and cold rubidium ( $^{87}\text{Rb}$ ) single atoms trapped in the tweezers are simultaneously rearranged without atom losses. In-situ feedback control for defect-free single-atom array formation is also demonstrated.

Establishing such reliable method to form a scalable neutral-atom platform has been an important task to be achieved for quantum information science and quantum simulation of many-body systems. The methodology presented in this thesis resolves the issue and is expected to contribute the progression in the field of neutral atoms quantum simulation and quantum information.

As a preliminary example, a quantum simulation experiment with tunable tweezer traps and Rydberg atom interaction was performed. This quantum simulator provides an ideal test bed for studying quantum coherent evolution of a many-body system after a quench. It allows to simulate a one-dimensional or two-dimensional lattice of Ising-like spin-1/2 particles or the Hamiltonian in Eq. (4.5) with parameters tunable in a wide range. The time evolution by measuring occupation probabilities of the eigenstates of a prequench Hamiltonian or a postquench Hamiltonian is monitored. The thermalization dynamics studied in this experiment belongs to the cases where the postquench Hamiltonian is slightly modified after quench so that  $H_0 \gg H_I$ . These results suggest that the detailed balance can be an underlying principle of the thermalization dynamics of the cases. The thermalization dynamics can be efficiently described by the diffusion governed by a master equation of a simple form, similarly to relaxation towards equilibrium in classical statistical mechanics but without its underlying assumptions of coupling to baths and the ergodicity hypothesis based on randomness.

## Chapter 6. Appendix

### 6.1 Trap depth calculation code in Matlab

Trap depth calculation based on Ref. [52] is implemented in Matlab.

```
c=3e8;
W0=(2*pi*c/780.241e-9+2*pi*c/794.978e-9)/2;%D1 line
g=2*pi*(5.746e6+6.065e6)/2;% decay rate
lambda=820e-9;%dipole laser wavelength
detune1=2*pi*c/794.978e-9-2*pi*c/lambda;%detune
detune2=2*pi*c/780.241e-9-2*pi*c/lambda;
h=6.34e-34;%Planck const.
hbar=h/2/pi;
epsilon=8.854e-12 %F/m, permittivity, vacuum, 1/4pi cgs. 1e-7J=1erg
m=1.67e-27*87;% Rb 87 mass
kb=1.38e-23;%Boltzman const

P=3.3e-3;
P=3.1e-3;%P=1.1;%laser power : 1100*0.55*0.5*0.9/9/9,
    ↪ 1000*0.448*0.99*0.9*0.5*0.96*0.99/8^2,
%1000=total power, 0.5=power at intermediate image, 0.99=dichroic,0.9=tube
%lens, 0.5=objective lens,0.96*0.99=glass cell,8^2=tweezer number.
% Meadowlark, new align: 710mW -> 430mW at the intermediate image.
% 430*0.99*0.9*0.55*0.96=202mW
%1020nm, 20mW=1.5mK.
r=1.14e-6;%r=34e-6;%laser intensity radius(1/e^2)
% r=2.4783e-6/2;
zr=pi*r^2/lambda;%Rayleigh range
I=P/(pi*(r)^2);%mean laser intensity
Ip=2*I;%peak laser intensity
wrmeasure=1.138e6/2;

U=3*pi*c^2*g/2/W0^3/detune1*Ip;%peak potential, temp
U=pi*c^2*g/2/W0^3*(1/detune1+2/detune2)*Ip;
Ug=m*9.8*2*r/kb;%gravity potential across radial direction, temperature
wr=sqrt(4*U/m/r^2);wz=sqrt(2*U/m/zr^2);
Uf=U/kb;
Uf1=U/h;

%%scatering rate
scatter=pi*c^2*g^2/2/hbar/W0^3*(1/detune1^2)*I;
```

```

size=sqrt(kb*80e-6/m)/wr;

%% velocity
T=70e-6;
vatom=sqrt(2*kb*T/m);% 0.1m/s @ 70 uK. 300nm travels during 3 us.
frequencies=c/480e-9-c/780e-9;
dopplerv=2*sqrt(2*kb*T*log(2)/m)/c*frequencies;%780 480 counter propagate doppler FWHM

```

## 6.2 Hungarian algorithm code in Matlab

Hungarian algorithm is used for finding complete and efficient matching solution between the filled sites and target sites. In the Section 3.6.1, the algorithm is of an essential part for operation. The below code is Hungarian algorithm implemented in Matlab.

It is downloaded from <http://csclab.murraystate.edu/bob.pilgrim/445/munkres.html>

```

function [assignment,cost] = munkres(costMat)
% MUNKRES Munkres (Hungarian) Algorithm for Linear Assignment Problem.
%
% [ASSIGN,COST] = munkres(COSTMAT) returns the optimal column indices,
% ASSIGN assigned to each row and the minimum COST based on the assignment
% problem represented by the COSTMAT, where the (i,j)th element represents the cost to
%   ↪ assign the jth
% job to the ith worker.
%
% Partial assignment: This code can identify a partial assignment is a full
% assignment is not feasible. For a partial assignment, there are some
% zero elements in the returning assignment vector, which indicate
% un-assigned tasks. The cost returned only contains the cost of partially
% assigned tasks.
%
% This is vectorized implementation of the algorithm. It is the fastest
% among all Matlab implementations of the algorithm.
%
% Examples
% Example 1: a 5 x 5 example
%{
[assignment,cost] = munkres(magic(5));
disp(assignment); % 3 2 1 5 4
disp(cost); %15
%}
% Example 2: 400 x 400 random data
%{
n=400;
A=rand(n);

```

```

tic
[a,b]=munkres(A);
toc % about 2 seconds
%}

% Example 3: rectangular assignment with inf costs
%{
A=rand(10,7);
A(A>0.7)=Inf;
[a,b]=munkres(A);
%}

% Example 4: an example of partial assignment
%{
A = [1 3 Inf; Inf Inf 5; Inf Inf 0.5];
[a,b]=munkres(A)
%}
% a = [1 0 3]
% b = 1.5
% Reference:
% "Munkres' Assignment Algorithm, Modified for Rectangular Matrices",
% http://csclab.murraystate.edu/bob.pilgrim/445/munkres.html

% version 2.3 by Yi Cao at Cranfield University on 11th September 2011

assignment = zeros(1,size(costMat,1));
cost = 0;

validMat = costMat == costMat & costMat < Inf;
bigM = 10^(ceil(log10(sum(costMat(validMat))))+1);
costMat(~validMat) = bigM;

% costMat(costMat~=costMat)=Inf;
% validMat = costMat<Inf;
validCol = any(validMat,1);
validRow = any(validMat,2);

nRows = sum(validRow);
nCols = sum(validCol);
n = max(nRows,nCols);
if ~n
    return
end

maxv=10*max(costMat(validMat));

```

```

dMat = zeros(n) + maxv;
dMat(1:nRows,1:nCols) = costMat(validRow,validCol);

%*****
% Munkres' Assignment Algorithm starts here
%*****

%%%%%%%%%%
% STEP 1: Subtract the row minimum from each row.
%%%%%%%%%%
minR = min(dMat,[],2);
minC = min(bsxfun(@minus, dMat, minR));

%*****
% STEP 2: Find a zero of dMat. If there are no starred zeros in its
% column or row start the zero. Repeat for each zero
%*****
zP = dMat == bsxfun(@plus, minC, minR);

starZ = zeros(n,1);
while any(zP(:))
    [r,c]=find(zP,1);
    starZ(r)=c;
    zP(r,:)=false;
    zP(:,c)=false;
end

while 1
%*****
% STEP 3: Cover each column with a starred zero. If all the columns are
% covered then the matching is maximum
%*****
    if all(starZ>0)
        break
    end
    coverColumn = false(1,n);
    coverColumn(starZ(starZ>0))=true;
    coverRow = false(n,1);
    primeZ = zeros(n,1);
    [rIdx, cIdx] = find(dMat(~coverRow,~coverColumn)==bsxfun(@plus,minR(~coverRow),
        ↪ minC(~coverColumn)));
    while 1
        %*****
        % STEP 4: Find a noncovered zero and prime it. If there is no starred

```

```

% zero in the row containing this primed zero, Go to Step 5.
% Otherwise, cover this row and uncover the column containing
% the starred zero. Continue in this manner until there are no
% uncovered zeros left. Save the smallest uncovered value and
% Go to Step 6.
%*****
cR = find(~coverRow);
cC = find(~coverColumn);
rIdx = cR(rIdx);
cIdx = cC(cIdx);
Step = 6;
while ~isempty(cIdx)
    uZr = rIdx(1);
    uZc = cIdx(1);
    primeZ(uZr) = uZc;
    stz = starZ(uZr);
    if ~stz
        Step = 5;
        break;
    end
    coverRow(uZr) = true;
    coverColumn(stz) = false;
    z = rIdx==uZr;
    rIdx(z) = [];
    cIdx(z) = [];
    cR = find(~coverRow);
    z = dMat(~coverRow,stz) == minR(~coverRow) + minC(stz);
    rIdx = [rIdx(:);cR(z)];
    cIdx = [cIdx(:);stz(ones(sum(z),1))];
end
if Step == 6
    % *****
    % STEP 6: Add the minimum uncovered value to every element of each covered
    % row, and subtract it from every element of each uncovered column.
    % Return to Step 4 without altering any stars, primes, or covered lines.
    %*****
    [minval,rIdx,cIdx]=outerplus(dMat(~coverRow,~coverColumn),minR(~coverRow),
        ↪ minC(~coverColumn));
    minC(~coverColumn) = minC(~coverColumn) + minval;
    minR(coverRow) = minR(coverRow) - minval;
else
    break
end
end
end

```

```

%*****
% STEP 5:
% Construct a series of alternating primed and starred zeros as
% follows:
% Let Z0 represent the uncovered primed zero found in Step 4.
% Let Z1 denote the starred zero in the column of Z0 (if any).
% Let Z2 denote the primed zero in the row of Z1 (there will always
% be one). Continue until the series terminates at a primed zero
% that has no starred zero in its column. Unstar each starred
% zero of the series, star each primed zero of the series, erase
% all primes and uncover every line in the matrix. Return to Step 3.
%*****
rowZ1 = find(starZ==uZc);
starZ(uZr)=uZc;
while rowZ1>0
    starZ(rowZ1)=0;
    uZc = primeZ(rowZ1);
    uZr = rowZ1;
    rowZ1 = find(starZ==uZc);
    starZ(uZr)=uZc;
end
end

% Cost of assignment
rowIdx = find(validRow);
colIdx = find(validCol);
starZ = starZ(1:nRows);
vIdx = starZ <= nCols;
assignment(rowIdx(vIdx)) = colIdx(starZ(vIdx));
pass = assignment(assignment>0);
pass(~diag(validMat(assignment>0,pass))) = 0;
assignment(assignment>0) = pass;
cost = trace(costMat(assignment>0,assignment(assignment>0)));

function [minval,rIdx,cIdx]=outerplus(M,x,y)
ny=size(M,2);
minval=inf;
for c=1:ny
    M(:,c)=M(:,c)-(x+y(c));
    minval = min(minval,min(M(:,c)));
end
[rIdx,cIdx]=find(M==minval);

```

### 6.3 Miscellaneous experimental apparatus

For driving hardware with analogue voltages, the voltage sources require enough power. In my case, 8-Ch programmable analogue voltage sources from National Instrument PCI card (6733) is used. The card only can supply 2 mA per channel. The current is so small that 50  $\Omega$  resistive load can not be driven by the card. The operational amplifier for the voltage sources is required as shown in Fig. 6.1

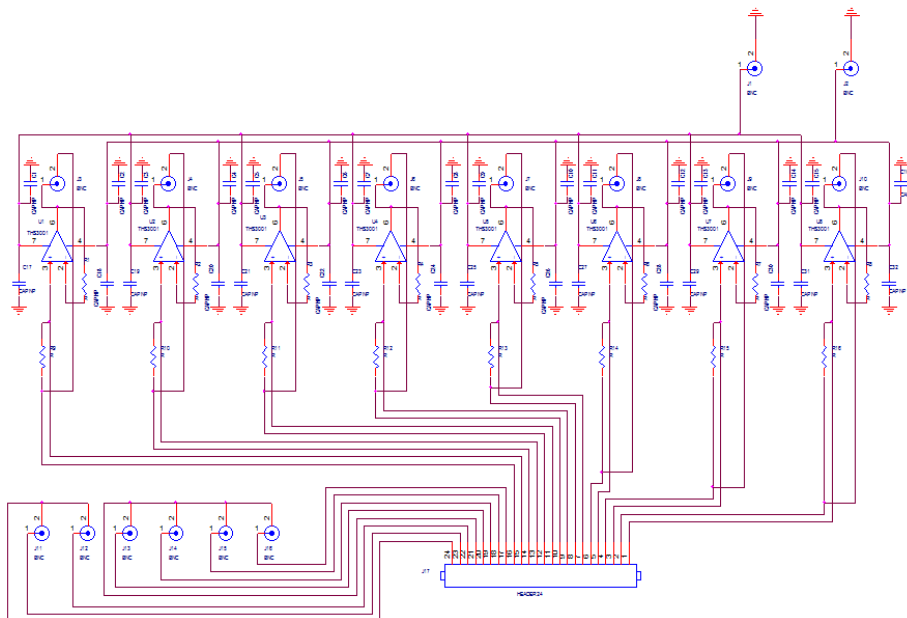


Figure 6.1: Current feed-back operational amplifier (OP-amp) for driving 50 Ohm load by using NI-6733 analogue pulse driver card. OP amp is TH-3001 current feed-back type from Texas Instrument.

For switching the MOT coil, MOSFET switch is designed and its switching performance is shown in Fig. 6.2.

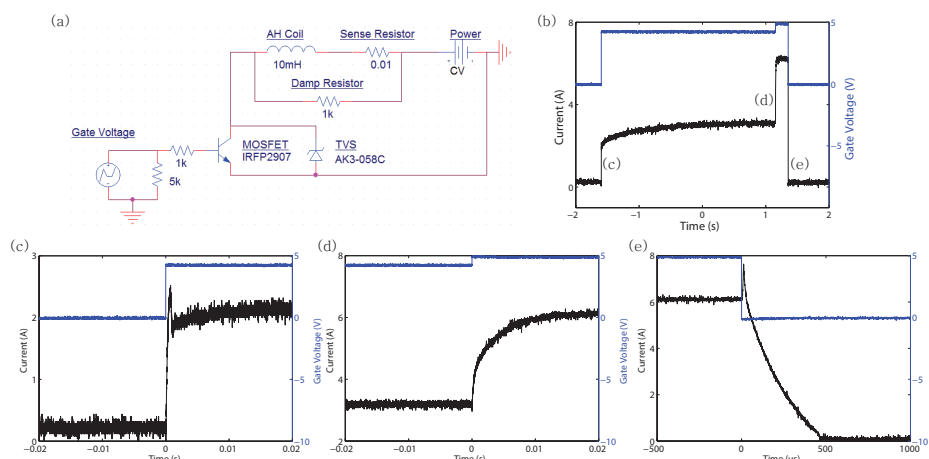


Figure 6.2: Home-built circuit for AH coil switch.

Figure 6.3 shows the on-off transient of bias coil current. Note that the bias coil magnetic field is 0.4 G/A and the current limit is 10 A thus maximum 4 G is achievable in the experiment. For the quantization axis define and optical pumping purpose, few gauss field is enough.

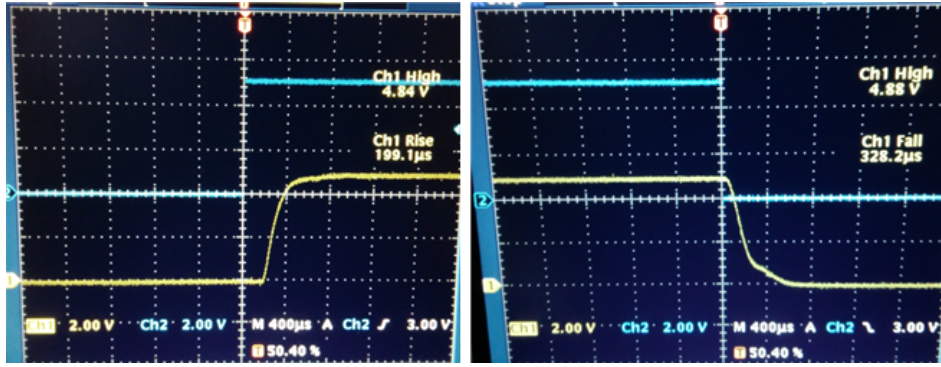


Figure 6.3: Current control transient of bias coil. The blue line corresponds to the current switch given by analog pulse from NI PCIe-6353 device. The current per switching voltage is 2 A/V. The yellow line corresponds to the current of the coil, 2 V/A. The current driver model is Sorenson DLM60-10 with M51A option.

Note that the current driver implements the analog control and monitor channels thus the end-user can easily do the hardware based current control without additional MOSFET-like switch compared to Figure 6.2. Moreover, its transient speed is satisfactory for the experiments.

## Bibliography

- [1] T. W. Hänsch, "Nobel Lecture: Passion for precision\*," *Rev. Mod. Phys.* **78**, 1297-1309 (2006).
- [2] S. Haroche, "Nobel Lecture: Controlling photons in a box and exploring the quantum to classical boundary\*," *Rev. Mod. Phys.* **85**, 1083-1102 (2013).
- [3] A. Aspect, P. Grangier, and G. Roger, "Experimental Tests of Realistic Local Theories via Bell's Theorem," *Phys. Rev. Lett.* **47**, 460-463 (1981).
- [4] A. Aspect, P. Grangier, and G. Roger, "Experimental Realization of Einstein-Podolsky-Rosen-Bohm *Gedankenexperiment* : A New Violation of Bell's Inequalities," *Phys. Rev. Lett.* **49**, 91-94 (1982).
- [5] B. Hensen, *et al.*, "Loophole-free Bell inequality violation using electron spins separated by 1.3 kilometres," *Nature* **526**, 682-686 (2015).
- [6] L. K. Shalm, *et al.*, "Strong Loophole-Free Test of Local Realism\*," *Phys. Rev. Lett.* **115**, 250402 (2015).
- [7] D. J. Wineland, "Nobel Lecture: Superposition, entanglement, and raising Schrödinger's cat\*," *Rev. Mod. Phys.* **85**, 1103-1114 (2013).
- [8] W. S. Warren, H. Rabitz, and M. Dahleh, "Coherent Control of Quantum Dynamics: The Dream Is Alive," *Science* **259**, 1581-1589 (1993).
- [9] A. C. Doherty, *et al.*, "Quantum feedback control and classical control theory," *Physical Review A* **62**, 012105 (2000).
- [10] K. B. Davis, *et al.*, "Bose-Einstein Condensation in a Gas of Sodium Atoms," *Phys. Rev. Lett.* **75**, 3969-3973 (1995).
- [11] C. Monroe, *et al.*, "Resolved-Sideband Raman Cooling of a Bound Atom to the 3D Zero-Point Energy," *Phys. Rev. Lett.* **75**, 4011-4014 (1995).
- [12] M. Greiner, *et al.*, "Quantum phase transition from a superfluid to a Mott insulator in a gas of ultracold atoms," *Nature* **415**, 39-44 (2002).
- [13] C. A. Sackett, *et al.*, "Experimental entanglement of four particles," *Nature* **404**, 256-259 (2000).
- [14] P. A. M. Dirac, "The Quantum Theory of the Emission and Absorption of Radiation," *Proceedings of the Royal Society of London. Series A* **114**, 243-265 (1927).
- [15] M. Brune, *et al.*, "Quantum Rabi Oscillation: A Direct Test of Field Quantization in a Cavity," *Phys. Rev. Lett.* **76**, 1800-1803 (1996).
- [16] A. Ourjoumtsev, R. Tualle-Brouri, J. Laurat, and P. Grangier, "Generating Optical Schrödinger Kittens for Quantum Information Processing," *Science* **312**, 83-86 (2006).
- [17] A. Wallraff, *et al.*, "Strong coupling of a single photon to a superconducting qubit using circuit quantum electrodynamics," *Nature* **431**, 162-167 (2004).

- [18] Veldhorst M, *et al.*, "An addressable quantum dot qubit with fault-tolerant control-fidelity," *Nat Nano* **9**, 981-985 (2014).
- [19] E. Togan, *et al.*, "Quantum entanglement between an optical photon and a solid-state spin qubit," *Nature* **466**, 730 (2010).
- [20] J. J. García-Ripoll, P. Zoller, and J. I. Cirac, "Speed Optimized Two-Qubit Gates with Laser Coherent Control Techniques for Ion Trap Quantum Computing," *Phys. Rev. Lett.* **91**, 157901 (2003).
- [21] F. Motzoi, J. M. Gambetta, P. Rebentrost, and F. K. Wilhelm, "Simple Pulses for Elimination of Leakage in Weakly Nonlinear Qubits," *Phys. Rev. Lett.* **103**, 110501 (2009).
- [22] S. Ritter, *et al.*, "An elementary quantum network of single atoms in optical cavities," *Nature* **484**, 195-200 (2012).
- [23] Z.-L. Xiang, S. Ashhab, J. Q. You, and F. Nori, "Hybrid quantum circuits: Superconducting circuits interacting with other quantum systems," *Rev. Mod. Phys.* **85**, 623-653 (2013).
- [24] C. Wang, *et al.*, "A Schrödinger cat living in two boxes," *Science* **352**, 1087-1091 (2016).
- [25] A. Goban, *et al.*, "Atom–light interactions in photonic crystals," *Nature Communications* **5**, 3808 (2014).
- [26] D. Hucul, *et al.*, "Modular entanglement of atomic qubits using photons and phonons," *Nat Phys* **11**, 37-42 (2015).
- [27] R. P. Feynman, "Simulating Physics with Computers," *Int. J. Theor. Phys.* **21**, 467-488 (1982).
- [28] R. Gerritsma, *et al.*, "Quantum simulation of the Dirac equation," *Nature* **463**, 68-71 (2010).
- [29] K. Kim, *et al.*, "Quantum simulation of frustrated Ising spins with trapped ions," *Nature* **465**, 590-593 (2010).
- [30] J. Simon, *et al.*, "Quantum simulation of antiferromagnetic spin chains in an optical lattice," *Nature* **472**, 307-312 (2011).
- [31] J. Struck, *et al.*, "Quantum Simulation of Frustrated Classical Magnetism in Triangular Optical Lattices," *Science* **333**, 996-999 (2011).
- [32] R. Islam, *et al.*, "Emergence and Frustration of Magnetism with Variable-Range Interactions in a Quantum Simulator," *Science* **340**, 583-587 (2013).
- [33] T. Kinoshita, T. Wenger, and D. S. Weiss, "A quantum Newton's cradle," *Nature* **440**, 900-903 (2006).
- [34] S. Hofferberth, *et al.*, "Non-equilibrium coherence dynamics in one-dimensional Bose gases," *Nature* **449**, 324-327 (2007).
- [35] C. Neill, *et al.*, "Ergodic dynamics and thermalization in an isolated quantum system," *Nat Phys* **advance online publication** (2016).
- [36] A. Kaufman, *et al.*, "Quantum thermalization through entanglement in an isolated many-body system," *arxiv1603.04409* (2016).

- [37] P. W. Shor, "Polynomial-time algorithms for prime factorization and discrete logarithms on a quantum computer," *SIAM J. Comput.* **26**, 1484-1509 (1997).
- [38] L. K. Grover, "Quantum mechanics helps in searching for a needle in a haystack," *Phys. Rev. Lett.* **79**, 325-328 (1997).
- [39] T. Monz, *et al.*, "Realization of a scalable Shor algorithm," *Science* **351**, 1068-1070 (2016).
- [40] N. Ofek, *et al.*, "Extending the lifetime of a quantum bit with error correction in superconducting circuits," *Nature* **536**, 441-445 (2016).
- [41] W. P. Schleich, *et al.*, "Quantum technology: from research to application," *Appl. Phys. B* **122**, 1-31 (2016).
- [42] W. Lee, H. Kim, and J. Ahn, "Three-dimensional rearrangement of single atoms using actively controlled optical microtraps," *Opt. Express* **24**, 9816-9825 (2016).
- [43] H. Kim, *et al.*, "In situ single-atom array synthesis using dynamic holographic optical tweezers," *Nat. Commun*, accepted (2016).
- [44] H. Labuhn, *et al.*, "Tunable two-dimensional arrays of single Rydberg atoms for realizing quantum Ising models," *Nature advance online publication*(2016).
- [45] <http://vacuumtunes.co.uk/vtut1.html>
- [46] G. F. Weston, "Chapter 1 - Fundamentals of vacuum science and technology," in *Ultrahigh Vacuum Practice* (Butterworth-Heinemann, 1985), pp. 1-21.
- [47] W. S. Bakr, *et al.*, "A quantum gas microscope for detecting single atoms in a Hubbard-regime optical lattice," *Nature* **462**, 74-77 (2009).
- [48] M. Mielenz, *et al.*, "Arrays of individually controlled ions suitable for two-dimensional quantum simulations," *Nature Communications* **7**, ncomms11839 (2016).
- [49] J. Dalibard and C. Cohen-Tannoudji, "Laser cooling below the Doppler limit by polarization gradients: simple theoretical models," *J. Opt. Soc. Am. B* **6**, 2023-2045 (1989).
- [50] E. Donley, *et al.*, "Double-pass acousto-optic modulator system," *Rev. Sci. Instrum.* **76**, 063112 (2005).
- [51] [http://www.nobelprize.org/nobel\\_prizes/physics/laureates/1997/illpres/doppler.html](http://www.nobelprize.org/nobel_prizes/physics/laureates/1997/illpres/doppler.html)
- [52] R. Grimm, M. Weidemüller, and Y. B. Ovchinnikov, "Optical Dipole Traps for Neutral Atoms," in *Advances In Atomic, Molecular, and Optical Physics*, B. Benjamin and W. Herbert, eds. (Academic Press, 2000), pp. 95-170.
- [53] J. J. Sakurai and J. Napolitano, *Modern quantum mechanics*, 2nd ed. (Addison-Wesley, Boston, 2011), pp. xviii, 550 p.
- [54] N. Schlosser, G. Reymond, I. Protsenko, and P. Grangier, "Sub-poissonian loading of single atoms in a microscopic dipole trap," *Nature* **411**, 1024-1027 (2001).
- [55] N. Schlosser, G. Reymond, and P. Grangier, "Collisional Blockade in Microscopic Optical Dipole Traps," *Phys. Rev. Lett.* **89**, 023005 (2002).

- [56] T. Grunzweig, A. Hilliard, M. McGovern, and M. F. Andersen, "Near-deterministic preparation of a single atom in an optical microtrap," *Nat Phys* **6**, 951-954 (2010).
- [57] Sortais, Y. R. P. et al. Diffraction-limited optics for single-atom manipulation. *Phys. Rev. A* **75**, 013406 (2007).
- [58] Tuchendler, C., Lance, A. M., Browaeys, A., Sortais, Y. R. P. & Grangier, P. Energy distribution and cooling of a single atom in an optical tweezer. *Phys. Rev. A* **78**, 033425 (2008).
- [59] Schlosser, N., Reymond, G., Protsenko, I. & Grangier, P. Sub-poissonian loading of single atoms in a microscopic dipole trap. *Nature* **411**, 1024-1027 (2001).
- [60] Schlosser, N., Reymond, G. & Grangier, P. Collisional blockade in microscopic optical dipole traps. *Phys. Rev. Lett.* **89**, 023005 (2002).
- [61] Karski, M. et al. Quantum walk in position space with single optically trapped atoms. *Science* **325**, 174-177 (2009).
- [62] Preiss, P. M. et al. Strongly correlated quantum walks in optical lattices. *Science* **347**, 1229-1233 (2015).
- [63] Beugnon, J. et al. Quantum interference between two single photons emitted by independently trapped atoms. *Nature* **440**, 779-782, (2006).
- [64] Bakr, W. S., Gillen, J. I., Peng, A., Folling, S. & Greiner, M. A quantum gas microscope for detecting single atoms in a Hubbard-regime optical lattice. *Nature* **462**, 74-77 (2009).
- [65] Miroshnychenko, Y. et al. An atom-sorting machine. *Nature* **442**, 151-151 (2006).
- [66] Isenhower, L. et al. Demonstration of a neutral atom controlled-NOT quantum gate. *Phys. Rev. Lett.* **104**, 010503 (2006).
- [67] Kaufman, A. M. et al. Two-particle quantum interference in tunnel-coupled optical tweezers. *Science* **345**, 306-309 (2014).
- [68] Nelson, K. D., Li, X. & Weiss, D. S. Imaging single atoms in a three-dimensional array. *Nature Phys.* **3**, 556-560 (2007).
- [69] Wang, Y., Zhang, X., Corcovilos, T. A., Kumar, A. & Weiss, D. S. Coherent addressing of individual neutral atoms in a 3D optical lattice. *Phys. Rev. Lett.* **115**, 043003 (2015).
- [70] Nogrette, F. et al. Single-atom trapping in holographic 2D arrays of microtraps with arbitrary geometries. *Phys. Rev. X* **4**, 021034 (2014).
- [71] Xia, T. et al. Randomized benchmarking of single-qubit gates in a 2D array of neutral-atom qubits. *Phys. Rev. Lett.* **114**, 100503 (2015).
- [72] Fung, Y., Carpentier, A., Sompert, P. & Andersen, M. Two-atom collisions and the loading of atoms in microtraps. *Entropy* **16**, 582-606 (2014).
- [73] Lester, B. J., Luick, N., Kaufman, A. M., Reynolds, C. M. & Regal, C. A. Rapid production of uniformly filled arrays of neutral atoms. *Phys. Rev. Lett.* **115**, 073003 (2015).

- [74] Bakr, W. S. *et al.* Orbital excitation blockade and algorithmic cooling in quantum gases. *Nature* **480**, 500-503 (2011).
- [75] Sherson, J. F. *et al.* Single-atom-resolved fluorescence imaging of an atomic Mott insulator. *Nature* **467**, 68-72 (2010).
- [76] Weiss, D. S. *et al.* Another way to approach zero entropy for a finite system of atoms. *Phys. Rev. A* **70**, 040302(R) (2004).
- [77] Vala, J. *et al.* Perfect pattern formation of neutral atoms in an addressable optical lattice. *Phys. Rev. A* **71**, 032324 (2005).
- [78] Lengwenus, A., Kruse, J., Schlosser, M., Tichelmann, S. & Birkel, G. Coherent transport of atomic quantum states in a scalable shift register. *Phys. Rev. Lett.* **105**, 170502 (2010).
- [79] Kuhr, S. *et al.* Coherence properties and quantum state transportation in an optical conveyor belt. *Phys. Rev. Lett.* **91**, 213002 (2003).
- [80] Kaufman, A. M. *et al.* Entangling two transportable neutral atoms via local spin exchange. *Nature* **527**, 208-211 (2015).
- [81] Xu, P. *et al.* Interaction-induced decay of a heteronuclear two-atom system. *Nature Comm.* **6**, 7803 (2015).
- [82] Dorner, U., Calarco, T., Zoller, P., Browaeys, A. & Grangier, P. Quantum logic via optimal control in holographic dipole traps. *J. Opt. B: Quant. Semiclass. Opt.* **7**, S341-S346 (2005).
- [83] M. Montes-Usategui, E. Pleguezuelos, J. Andilla, and E. Martin-Badosa, Fast generation of holographic optical tweezers by random mask encoding of Fourier components, *Opt. Express* **14**, 2101-2107 (2006).
- [84] Miroshnychenko, Y. *et al.* Continued imaging of the transport of a single neutral atom. *Opt. Express* **11**, 3498-3502 (2003).
- [85] Shimobaba, T., Ito, T., Masuda, N., Ichihashi, Y. & Takada, N. Fast calculation of computer-generated-hologram on AMD HD5000 series GPU and OpenCL. *Opt. Express* **18**, 9955-9960 (2010).
- [86] McGloin, D., Spalding, G. C., Melville, H., Sibbett, W. & Dholakia, K. Applications of spatial light modulators in atom optics. *Opt. Express* **11**, 158-166 (2003).
- [87] He, X., Xu, P., Wang, J. & Zhan, M. Rotating single atoms in a ring lattice generated by a spatial light modulator. *Opt. Express* **17**, 21007-21014 (2009).
- [88] Curtis, J. E., Koss, B. A. & Grier, D. G. Dynamic holographic optical tweezers. *Opt. Comm.* **207**, 169-175 (2002).
- [89] Muldoon, C. *et al.* Control and manipulation of cold atoms in optical tweezers. *New J. Phys.* **14**, 073051 (2012).
- [90] Boyer, V. *et al.* Dynamic manipulation of Bose-Einstein condensates with a spatial light modulator. *Phys. Rev. A* **73**, 031402 (2006).

- [91] Jauregui, R. Nonperturbative and perturbative treatments of parametric heating in atom traps. *Phys. Rev. A* **64**, 053408 (2001).
- [92] Gehm, M. E., O'Hara, K. M., Savard, T. A. & Thomas, J. E. Dynamics of noise-induced heating in atom traps. *Phys. Rev. A* **58**, 3914-3921 (1998).
- [93] McGovern, M., Grunzweig, T., Hilliard, A. J. & Andersen, M. F. Single beam atom sorting machine. *Laser Phys. Lett.* **9**, 78-84 (2012).
- [94] Lee, W., Kim, H., & Ahn, J. Three-dimensional rearrangement of single atoms using actively controlled optical microtraps. *Opt. Express* **24**, 9816-9825 (2016).
- [95] D. Engström, J. Bengtsson, E. Eriksson, and M. Goksör, "Improved beam steering accuracy of a single beam with a 1D phase-only spatial light modulator," *Opt. Express* **16**, 18275-18287 (2008).
- [96] D. G. Grier, "A revolution in optical manipulation," *Nature* **424**, 810-816 (2003).
- [97] K. Dholakia and T. Cizmar, "Shaping the future of manipulation," *Nat. Photon* **5**, 335-342 (2011).
- [98] Y. Roichman and D. G. Grier, "Holographic assembly of quasicrystalline photonic heterostructures," *Opt. Express* **13**, 5434-5439 (2005).
- [99] K. Kim, J. Yoon, and Y. Park, "Simultaneous 3D visualization and position tracking of optically trapped particles using optical diffraction tomography," *Optica* **2**, 343-346 (2015).
- [100] R. Diekmann *et al.*, "Nanoscopy of bacterial cells immobilized by holographic optical tweezers," *Nat. Comm.* **7**, 13711 (2016).
- [101] F. Nogrette *et al.*, "Single-Atom Trapping in Holographic 2D Arrays of Microtraps with Arbitrary Geometries," *Physical Review X* **4**, 021034 (2014).
- [102] H. Tamura *et al.*, "Highly uniform holographic microtrap arrays for single atom trapping using a feedback optimization of in-trap fluorescence measurements," *Opt. Express* **24**, 8132-8141 (2016).
- [103] T. Xia *et al.*, "Randomized Benchmarking of Single-Qubit Gates in a 2D Array of Neutral-Atom Qubits," *Phys. Rev. Lett.* **114**, 100503 (2015).
- [104] M. Endres *et al.*, "Atom-by-atom assembly of defect-free one-dimensional cold atom arrays," *Science* **354**, 1024-1027 (2016).
- [105] D. Barredo *et al.*, "An atom-by-atom assembler of defect-free arbitrary two-dimensional atomic arrays," *Science* **354**, 1021-1023 (2016).
- [106] H. Bernien, *et al.*, "Probing many-body dynamics on a 51-atom quantum simulator," *Nature* **551**, 579 (2017).
- [107] V. Lienhard, *et al.*, "Observing the space- and time-dependent growth of correlations in dynamically tuned synthetic Ising antiferromagnets," arXiv:1711.01185 (2017).
- [108] H. Kim, *et al.*, "Detailed Balance of Thermalization dynamics in Rydberg atom quantum simulators," arXiv:1712.02065 (2017).
- [109] J. E. Curtis, B. A. Koss, and D. G. Grier, "Dynamic holographic optical tweezers," *Optics Communications* **207**, 169-175 (2002).

- [110] W. Lee, H. Kim, and J. Ahn, “Defect-free atomic array formation using the Hungarian matching algorithm,” *Physical Review A* **95**, 053424 (2017).
- [111] T. Cizmar, M. Mazilu, and K. Dholakia, “In situ wavefront correction and its application to micromanipulation,” *Nat. Photonics* **4**, 388-394 (2010).
- [112] M. Persson, D. Engstrom, and M. Goksor, “Reducing the effect of pixel crosstalk in phase only spatial light modulators,” *Opt. Express* **20**, 22334-22343 (2012).
- [113] D. McGloin *et al.*, “Applications of spatial light modulators in atom optics,” *Opt. Express* **11**, 158-166 (2003).
- [114] V. Boyer *et al.*, “Dynamic manipulation of Bose-Einstein condensates with a spatial light modulator,” *Physical Review A* **73**(2006).
- [115] G. Thalhammer *et al.*, “Speeding up liquid crystal SLMs using overdrive with phase change reduction,” *Opt. Express* **21**, 1779-1797 (2013).
- [116] S. P. Poland *et al.*, “Development of a doubly weighted Gerchberg-Saxton algorithm for use in multibeam imaging applications,” *Opt. Lett.* **39**, 2431-2434 (2014).
- [117] T. W. Clark *et al.*, “Comparison of beam generation techniques using a phase only spatial light modulator,” *Opt. Express* **24**, 6249-6264 (2016).
- [118] P. Zupancic *et al.*, “Ultra-precise holographic beam shaping for microscopic quantum control,” *Opt. Express* **24**, 13881-13893 (2016).
- [119] A. M. Kaufman, B. J. Lester, and C. A. Regal, “Cooling a Single Atom in an Optical Tweezer to Its Quantum Ground State,” *Physical Review X* **2**, 041014 (2012).
- [120] G. Shabtay, “Three-dimensional beam forming and Ewald’s surfaces,” *Opt. Comm.* **226** 33-37 (2003).
- [121] W. Graeme and C. Johannes, “Experimental demonstration of holographic three-dimensional light shaping using a Gerchberg-Saxton algorithm,” *New J. Phys.* **7**, 117 (2005).
- [122] C. Hao *et al.*, “Holographic optical tweezers obtained by using the three-dimensional Gerchberg-Saxton algorithm,” *J. Opt.* **15**, 035401 (2013).
- [123] G. Sinclair *et al.*, “Interactive application in holographic optical tweezers of a multi-plane Gerchberg-Saxton algorithm for three-dimensional light shaping,” *Opt. Express* **12**, 1665-1670 (2004).
- [124] F. O. Fahrbach *et al.*, “Rapid 3D light-sheet microscopy with a tunable lens,” *Opt. Express* **21**, 21010-21026 (2013).
- [125] T. F. Gallagher, *Rydberg Atoms* (Cambridge University Press, 2005).
- [126] R. Low, *et al.*, “An experimental and theoretical guide to strongly interacting Rydberg gases,” *J Phys B-at Mol Opt* **45**(2012).

- [127] I. I. Beterov, I. I. Ryabtsev, D. B. Tretyakov, and V. M. Entin, "Quasiclassical calculations of blackbody-radiation-induced depopulation rates and effective lifetimes of Rydberg  $nS$ ,  $nP$ , and  $nD$  alkali-metal atoms with  $n \leq 80$ ," *Physical Review A* **80**(2009).
- [128] L. Beguin, "Measurement of the van der Waals interaction between two Rydberg atoms," HAL Id: pastel-00936072 <https://pastel.archives-ouvertes.fr/pastel-00936072> (2014).
- [129] W. Sebastian, *et al.*, "Calculation of Rydberg interaction potentials," *J. Phys. B: At. Mol. Phys.* **50**, 133001 (2017).
- [130] M. Saffman, T. G. Walker, and K. Mølmer, "Quantum information with Rydberg atoms," *Rev. Mod. Phys.* **82**, 2313-2363 (2010).
- [131] H. Weimer, *et al.*, "A Rydberg quantum simulator," *Nat Phys* **6**, 382-388 (2010).
- [132] A. M. Hankin, *et al.*, "Two-atom Rydberg blockade using direct  $6S$  to  $nP$  excitation," *Physical Review A* **89**(2014).
- [133] J. Zeiher, *et al.*, "Many-body interferometry of a Rydberg-dressed spin lattice," *Nat Phys* **12**, 1095-1099 (2016).
- [134] E. Guardado-Sanchez, *et al.*, "Probing quench dynamics across a quantum phase transition into a 2D Ising antiferromagnet," arXiv:1711:00887 (2017).
- [135] P. Schauß, *et al.*, "Crystallization in Ising quantum magnets," *Science* **347**, 1455-1458 (2015).
- [136] M. Mack, *et al.*, "Measurement of absolute transition frequencies of  $^{87}\text{Rb}$  to  $nS$  and  $nD$  Rydberg states by means of electromagnetically induced transparency," *Physical Review A* **83**, 052515 (2011).
- [137] J. M. Obrecht, R. J. Wild, and E. A. Cornell, "Measuring electric fields from surface contaminants with neutral atoms," *Physical Review A* **75**, 062903 (2007).
- [138] S. A. Miller, D. A. Anderson, and G. Raithel, "Radio-frequency-modulated Rydberg states in a vapor cell," *New J. Phys.* **18**, 053017 (2016).
- [139] K. M. Maller, *et al.*, "Rydberg-blockade controlled-not gate and entanglement in a two-dimensional array of neutral-atom qubits," *Physical Review A* **92**, 022336 (2015).
- [140] R. K. Pathria and P. D. Beale, *Statistical Mechanics* (Elsevier Science, 1996).
- [141] A. Polkovnikov, K. Sengupta, A. Silva, and M. Vengalattore, "Colloquium: Nonequilibrium dynamics of closed interacting quantum systems," *Rev. Mod. Phys.* **83**, 863-883 (2011).
- [142] J. Eisert, M. Friesdorf, and C. Gogolin, "Quantum many-body systems out of equilibrium," *Nat Phys* **11**, 124-130 (2015).
- [143] G. Christian and E. Jens, "Equilibration, thermalisation, and the emergence of statistical mechanics in closed quantum systems," *Rep. Prog. Phys.* **79**, 056001 (2016).
- [144] T. Langen, *et al.*, "Local emergence of thermal correlations in an isolated quantum many-body system," *Nat Phys* **9**, 640-643 (2013).
- [145] G. Clos, D. Porras, U. Warring, and T. Schaetz, "Time-Resolved Observation of Thermalization in an Isolated Quantum System," *Phys. Rev. Lett.* **117**, 170401 (2016).

- [146] K. Georg, *et al.*, "Critical thermalization of a disordered dipolar spin system in diamond," arXiv:1609.08216 (2016).
- [147] J. M. Deutsch, "Quantum statistical mechanics in a closed system," *Physical Review A* **43**, 2046-2049 (1991).
- [148] M. Srednicki, "Chaos and quantum thermalization," *Phys Rev E* **50**, 888-901 (1994).
- [149] S. Mark, "The approach to thermal equilibrium in quantized chaotic systems," *J. Phys. A: Math. Gen.* **32**, 1163 (1999).
- [150] M. Rigol, V. Dunjko, and M. Olshanii, "Thermalization and its mechanism for generic isolated quantum systems," *Nature* **452**, 854-858 (2008).
- [151] M. Rigol and M. Srednicki, "Alternatives to Eigenstate Thermalization," *Phys. Rev. Lett.* **108**, 110601 (2012).
- [152] L. D'Alessio, Y. Kafri, A. Polkovnikov, and M. Rigol, "From quantum chaos and eigenstate thermalization to statistical mechanics and thermodynamics," *Adv. Phys.* **65**, 239-362 (2016).
- [153] C. Ates, J. P. Garrahan, and I. Lesanovsky, "Thermalization of a Strongly Interacting Closed Spin System: From Coherent Many-Body Dynamics to a Fokker-Planck Equation," *Phys. Rev. Lett.* **108**, 110603 (2012).
- [154] I. Lesanovsky, B. Olmos, and J. P. Garrahan, "Thermalization in a Coherently Driven Ensemble of Two-Level Systems," *Phys. Rev. Lett.* **105**, 100603 (2010).
- [155] T. Kiendl and F. Marquardt, "Many-Particle Dephasing after a Quench," *Phys. Rev. Lett.* **118**, 130601 (2017).
- [156] H. Weimer, R. Löw, T. Pfau, and H. P. Büchler, "Quantum Critical Behavior in Strongly Interacting Rydberg Gases," *Phys. Rev. Lett.* **101**, 250601 (2008).
- [157] M. Marcuzzi, *et al.*, "Facilitation Dynamics and Localization Phenomena in Rydberg Lattice Gases with Position Disorder," *Phys. Rev. Lett.* **118**, 063606 (2017).
- [158] B. Olmos, M. Müller, and I. Lesanovsky, "Thermalization of a strongly interacting 1D Rydberg lattice gas," *New J. Phys.* **12**, 013024 (2010).
- [159] X. L. Zhang, *et al.*, "Fidelity of a Rydberg-blockade quantum gate from simulated quantum process tomography," *Physical Review A* **85**, 042310 (2012).
- [160] Y. Miroshnychenko, *et al.*, "Coherent excitation of a single atom to a Rydberg state," *Physical Review A* **82**, 013405 (2010).
- [161] G. Lindblad, "On the generators of quantum dynamical semigroups," *Comm. Math. Phys.* **48**, 119-130 (1976).
- [162] V. Gorini, A. Kossakowski, and E. C. G. Sudarshan, "Completely positive dynamical semigroups of Nlevel systems," *J Math Phys* **17**, 821-825 (1976).
- [163] U. Schollwöck, "The density-matrix renormalization group," *Rev. Mod. Phys.* **77**, 259-315 (2005).

- [164] B. Pirvu, V. Murg, J. I. Cirac, and F. Verstraete, "Matrix product operator representations," *New J. Phys.* **12**, 025012 (2010).
- [165] F. Verstraete, J. J. García-Ripoll, and J. I. Cirac, "Matrix Product Density Operators: Simulation of Finite-Temperature and Dissipative Systems," *Phys. Rev. Lett.* **93**, 207204 (2004).
- [166] F. Verstraete, V. Murg, and J. I. Cirac, "Matrix product states, projected entangled pair states, and variational renormalization group methods for quantum spin systems," *Adv. Phys.* **57**, 143-224 (2008).

## Acknowledgments in Korean

학업과 연구를 수행해 나갈 수 있게 많은 가르침과 도움을 주신 지도교수 안재욱 선생님과 연구실의 동료들인 임종석, 이상경, 이민우, 한대훈, 이한결 박사님과 이우준, 조한래, 송윤홍, 김민혁 학생들에게 감사 인사를 전합니다. 특히 선생님께서 가르쳐 주신 엄격한 연구윤리와 끈기는 어떠한 일을 수행하든지 간에 그 기저에 품어야 할 근본 가치임을 기억하겠습니다. 이 학위논문을 심사해주시기 위해 귀한 시간 내어주신 심사위원 이순철, 강명수, 이성빈, 이재훈 선생님들께 또한 감사드립니다. 그리고 이 논문의 마지막 부분인 리드버그 양자모사에 대해 수많은 이론계산을 수행해주시고 도움을 주신 박예제 박사님, 심홍선 선생님께도 감사드립니다.

학위 기간동안 가족들의 신뢰와 지원은 연구를 지속하는 데 큰 힘이 되었습니다. 친애하는 친구들과의 교류 또한 무미건조할 수 있었던 지난 시간들을 즐겁운 순간으로 떠올리게 해주는 값진 기억들입니다. 특히 공진택, 김민중, 김진, 이승훈과 나눈 흥미로운 대화들은 긴 시간 추억으로 남을 것입니다. 이 분들께도 이 편을 빌려 감사인사 드립니다.

# Curriculum Vitae

Name : Hyosub Kim

## Educations

- KAIST, South Korea
2011. 3. – 2018. 2. Ph.D., Physics
2007. 3. – 2011. 2. BS, Physics

## Teaching Experience

2013. 3. – 2014. 2. TA, PH351 "Experimental Physics," KAIST
2012. 9. – 2013. 2. TA, PH142 "General Physics2," KAIST
2012. 3. – 2013. 2. TA, RnE "Measuring Birefringence of 5CB LC in THz-TDS ," KSA of KAIST
2010. 3. – 2010. 9. TA, PH141 "General Physics1," KAIST
2008. 3. – 2008. 9. Co-editor, MattLetter,  $M^2$  of KAIST

## Research Experience

2011. 6. – current **Korea Advanced Institute of Science and Technology**  
Graduate Researcher; Advisor: Jaewook Ahn  
Single-atom trapping, and Rydberg atom quantum simulation  
Ultrafast coherent control of atoms  
Low temperature THz time-domain spectroscopy of materials
2010. 6. – 2011. 2. **Korea Atomic Energy Research Institute**  
Internship; Advisor: Kyu-Ha Jang  
FDTD simulation of metal-grid THz mirror for THz-FEL

## Grants and Awards

2017. 10 **Conference, Student Presentation award**  
The Korea Physical Society
2017. 9. **Department of Physics, Pre-doctoral Fellow award**  
KAIST
2017. 2. **Conference, Student Presentation award**  
Optical Society of Korea
2014. 10. **Conference, Student Poster award**

## Publications

1. **Hyosub Kim**, Yeje Park, Kyungtae Kim, H.-S Sim, and Jaewook Ahn, "Detailed Balance of Thermalization dynamics in Rydberg atom quantum simulators," arXiv:1712.02065 (2017).
2. Yunheung Song, Han-gyeol Lee, **Hyosub Kim**, Hanlae Jo, and Jaewook Ahn, "Ultrafast X rotations of atomic clock states," <http://arxiv.org/abs/1706.10021>
3. Woojun Lee, **Hyosub Kim**, and Jaewook Ahn, "Defect-free atomic array formation using the Hungarian matching algorithm," *Physical Review A* **95**, 053424 (2017)
4. **H. Kim**, W.Lee, H.-g. Lee, H. Jo, Y. Song, and J. Ahn, "In situ single-atom array synthesis by dynamic holographic optical tweezers," *Nature Communication* **7**, 13317 (2016).
5. W. Lee, **H. Kim**, and J. Ahn, "Three-dimensional rearrangement of single atoms using actively controlled optical microtraps," *Opt. Express* **24**, 9816-9825 (2016).
6. H.-g. Lee, Y. Song, **H. Kim**, H. Jo, and J. Ahn, "Quantum dynamics of a two-state system induced by a chirped zero-area pulse," *Physical Review A* **93**, 023423 (2016).
7. W. Lee, **H. Kim**, K. Kim, and J. Ahn, "Coherent control of resonant two-photon transitions by counterpropagating ultrashort pulse pairs," *Physical Review A* **92**, 033415 (2015).
8. H.-g. Lee, **H. Kim**, and J. Ahn, "Ultrafast laser-driven Rabi oscillations of a trapped atomic vapor," *Opt. Lett.* **40**, 510-513 (2015).
9. **H. Kim**, Y. Song, H.-g. Lee, and J. Ahn, "Rabi oscillations of Morris-Shore transformed  $N$ -state systems by elliptically polarized ultrafast laser pulses," *Physical Review A* **91**, 053421 (2015).
10. **H. Kim**, W. Lee, H. Lee, and J. Ahn, "Nonparaxial aberrations in the optical Talbot effect probed by quantum-dot fluorescence tomography," *Physical Review A* **91**, 033817 (2015).
11. **H. Kim**, H. Lee, J. Lim, and J. Ahn, "Optimal Pulse Shaping for Ultrafast Laser Interaction with Quantum Systems," in *Progress in Ultrafast Intense Laser Science XI*, K. Yamanouchi, H. C. Nam, and P. Martin, eds. (Springer International Publishing, Cham, 2015), pp. 73-94.
12. H.-g. Lee, **H. Kim**, J. Lim, and J. Ahn, "Quantum interference control of a four-level diamond-configuration quantum system," *Physical Review A* **88**, 053427 (2013).
13. M. Yi, **H. Kim**, K. H. Jin, J. C. Ye, and J. Ahn, "Terahertz substance imaging by waveform shaping," *Opt. Express* **20**, 20783-20789 (2012).
14. **H. Kim**, M. Yi, X. Wang, S.-W. Cheong, and J. Ahn, "Ultrafast terahertz transmission ellipsometry of YMn<sub>2</sub>O<sub>5</sub> electromagnons," *Appl. Phys. Lett.* **101**, 242911 (2012).

## Patents

1. Jaewook Ahn, Hyosub Kim, Woojun Lee, "DYNAMIC HOLOGRAPHIC SINGLE ATOM TWEEZERS AND TWEEZING METHOD USING THEREOF," Korea Patent, Registration No. : 10-1783404-0000.

## Academic Activities

1. **Hyosub Kim**, Yeje Park, Heungsun Sim, Kyungtae Kim, Woojun Lee, Yunheung Song, and Jaewook Ahn, "Thermalization dynamics of an Ising quantum magnet," D5.05, 2017 KPS Fall Meeting, 2017.10.25-2017.10.27 (**Presentation award**)
2. **Hyosub Kim**, Kyungtae Kim, Woojun Lee and Jaewook Ahn, "Quantum simulation with up to N=30 Rydberg atoms for quantum Ising dynamics," Contributed talks Session B Wednesday, ICSSUR 2017, Jeju, South Korea.
3. **Hyosub Kim**, Kyungtae Kim, Woojun Lee, and Jaewook Ahn, "Quantum simulation with N=19 Rydberg atoms for quantum Ising dynamics," JTh5C.1, 14-19 May, CLEO 2017, San Jose, California, USA. (**Post-deadline**)
4. **Hyosub Kim**, Woojun Lee, and Jaewook Ahn, "Deterministic single-atom array preparation using dynamic holographic optical tweezers," FTu3E.8, 14-19 May, CLEO 2017, San Jose, California, USA.
5. **Hyosub Kim**, Woojun Lee, Jaewook Ahn, "Gerchberg-Saxton Algorithm for Single-Atom Dynamic Holographic Optical Tweezer," 제 28회 한국광학회 정기총회 및 2017 동계학술발표회, 하이원리조트 컨벤션호텔, W2C-VII-4, 2017 02/15-17. (**Presentation award**)
6. **Hyosub Kim**, Woojun Lee, Han-gyeol Lee, Hanlae Jo, Yunheung Song, and Jaewook Ahn, "Dynamic holographic single-atom arrays for deterministic single-atom loading," ICAP 2016, Mon-096, Seoul, South Korea, July 24-29, 2016.
7. **Hyosub Kim**, Woojun Lee, and Jaewook Ahn, "Experimental realization of real-time feedback-control of single-atom arrays," DAMOP 2016, T5.00006, Providence, RI, USA, 5/23-27, 2016.
8. **Hyosub Kim**, Yunheung Song, Han-Gyeol Lee, and Jaewook Ahn, "Ultrafast Laser-Driven Rabi Oscillation of Morris-Shore Transformed Multi-Level Atoms", CLEO-PR 2015, BEXCO, Korea, 26G1-5, 8/24-28, 2015.
9. 김효섭, 이한결, 이우준, 조한래, 송운홍, 안재욱, "탈보트 간섭 효과를 이용한 루비듐 원자 광포획 실험 연구", 제14회 첨단 레이저 및 레이저 응용 워크숍 (ALTA 2015), 제주도, 서귀포 KAL호텔, Fri-P-81, 5/6-9 (5/8), 2015
10. 김효섭, 송운홍, 이한결, 안재욱, "루비듐 원자의 초고속 라비 진동: 모리스 쇼어 변환", 한국광학회 제 26회 정기총회 및 2015년도 동계학술발표회, 대전컨벤션센터, T2E-VIII2, 1/28-30 (1/29), 2015.
11. **Hyosub Kim**, Hangyeol Lee, Jaewook Ahn, "Ultrafast manipulation of atomic ground hyperfine sublevel", 한국물리학회 2014년 가을학술논문발표회 및 임시총회, 광주 김대중 컨벤션 센터, P1-J010\*, 10/22-24, 2014. (**poster award**)
12. **Hyosub Kim**, Woojun Lee, Hangyeol Lee, Jaewook Ahn, "Design of optical Talbot focal point array for neutral atom quantum computing", ICAP 2014, Washington D. C., USA, Th-149, August 3-8, 2014.
13. 김효섭, 이우준, 이한결, 안재욱 "CdSe 양자점 박막을 이용한 3차원 탈보 카펫의 공초점 이미지 (Confocal imaging of 3D talbot carpet by using CdSe QD film)", 제13회 첨단레이저 및 레이저응용 워크숍 (ALTA2014), 제주도, 서귀포 KAL호텔, Fri-P-62, 5/7-10, 2014.
14. 김효섭, 이한결, 임종석, 안재욱 "Ultrafast Ramsey Interference Observed in REMPI Process", 한국물리학회 가을학술논문발표회 및 임시총회, 창원 컨벤션 센터, P3-J010, 10/30-11/1, 2013.
15. 김효섭, 이한결, 임종석, 안재욱, "루비듐 원자의 이광자 전이 경로간의 간섭현상 관측", 제12회 첨단 레이저 및 레이저 응용 워크숍 (ALTA2013), 제주도, 서귀포 KAL호텔, 5/2-4, 2013.

16. **Hyosub Kim**, Minwoo Yi, Xueyun Wang, Sang-Wook Cheong, and Jaewook Ahn, "Ultrafast Terahertz Transmission Ellipsometry of YMn<sub>2</sub>O<sub>5</sub> Electromagnons", 한국물리학회 봄 학술논문발표회 및 임시총회, 대전 컨벤션 센터, P2-D084, 4/24-26, 2013.
17. 김효섭, 이민우, 안재욱, "사방정계 다강체의 전기적 매그논 모드에 관한 초고속 테라헤르쯔 분광 연구," 2012년도 한국광학회 하계학술발표회, MP-I1, 제주도, 금호리조트, 2012년 8월 27일 29일.

